



Christian Puchwein, BSc

Development of a projection unit for fast 3D-measurement with structured light projection

Master's thesis

to achieve the university degree of
Diplom-IngenieurIn

Master's degree programme: Production Science and Management

submitted to

Graz University of Technology

Supervisor

DI Bernhard Gütl
KNAPP AG

Ao.Univ.-Prof.i.R. Laurentius Windholz
Institute for Experimental Physics

Graz, May 2015

EIDESSTÄTTLICHE ERKLÄRUNG AFFIDAVIT

Ich erkläre an Eides statt, dass ich die vorliegende Arbeit selbstständig verfasst, andere als die angegebenen Quellen / Hilfsmittel nicht benutzt, und die den benutzten Quellen wörtlich und inhaltlich entnommenen Stellen als solche kenntlich gemacht habe. Das in TUGRAZonline hochgeladene Textdokument ist mit der vorliegenden Masterarbeit identisch.

I declare that I have authored this thesis independently, that I have not used other than the declared sources / resources, and that I have explicitly indicated all material which has been quoted either literally or by content from the sources used. The text document uploaded to TUGRAZonline is identical to the present master's thesis.

.....
Datum / Date

.....
Unterschrift / Signature

Danksagung

An dieser Stelle möchte ich mich bei all jenen Personen bedanken die mich während meines Studiums unterstützt und begleitet haben und somit zur Entstehung dieser Masterarbeit beitrugen.

Besonders bei meinen Eltern Edith und Gerd möchte ich mich für die emotionale und finanzielle Unterstützung bedanken, die mir mein Studium erst ermöglicht hat. Auch bei meinen beiden Brüdern Ewald und Martin, die mir immer Vorbild und Inspiration sein werden und mir mit Rat und Tat zur Seite standen, möchte ich mich herzlichst bedanken.

Großer Dank gebührt meiner Freundin Eva, die mir ein großer Rückhalt in meinem Leben ist und mir während meiner Studienzeit immer zur Seite stand. Ich liebe dich.

Auch meinen Freunden und Studienkollegen danke ich für die unvergessliche Studienzeit.

Nicht zuletzt möchte ich mich bei meinem Betreuer Prof. Laurentius Windholz, für die geduldige und konstruktive Betreuung meiner Masterarbeit bedanken sowie meinem Betreuer Bernhard und meinen Kollegen bei KNAPP, durch die ich Teil dieses spannenden Projekts sein durfte.

Besonderer Dank an meine Schwägerin Janna und meinen Bruder Ewald für die Durchsicht und Korrektur dieser Masterarbeit.

Abstract

In this master thesis an industrial high speed projection unit for a vision system for 3D-measurements of objects is developed for the company KNAPP AG, a material handling and logistics solution provider situated in Hart bei Graz in Austria. At first, a brief overview of the applications for 3D-measurement systems as well as the different methods to measure objects is provided. The scope of this study is then focused on the method of structured light projection. The algorithm for the generation of the 3D-point cloud is not part of this master thesis due to contractual agreements with an external provider. Furthermore, a market research of existing products is presented and the different concepts of projecting structured light are discussed. Ultimately, a prototype is designed, built and tested regarding brightness, optics, adaptability and feasibility. At the end, an outlook on future areas of application is given and further developments of the vision system are discussed.

In dieser Masterarbeit wird eine Projektionseinheit für ein Vision System zur schnellen 3D-Vermessung von Objekten für die Firma KNAPP AG, einem Unternehmen für Lagerlogistik und Lagerautomation mit dem Sitz in Hart bei Graz in Österreich, ausgearbeitet. Zuerst wird ein kurzer Überblick der Anwendungen von 3D-Messsystemen gegeben, mit dem Fokus auf der 3D-Vermessung mittels Streifenprojektion. Der Algorithmus zur Erstellung der 3D-Punktvolke selbst wird von einem externen Unternehmen zur Verfügung gestellt und ist aufgrund vertraglicher Vereinbarung nicht Teil dieser Arbeit. Der Fokus liegt auf der schnellen Projektion der Sequenz von Streifenmustern. Eine Marktrecherche der zu Verfügung stehenden Projektionseinheiten wird durchgeführt und die unterschiedlichen Konzepte der Projektion von Streifenmustern werden vorgestellt. Schlussendlich wird ein Prototyp bereitgestellt, der in Bezug auf Helligkeit, Optik, Anpassbarkeit und Machbarkeit getestet wird. Auch ein Ausblick auf zukünftige Anwendungsgebiete und weitere Entwicklungsschritte des Prototyps wird gegeben.

Contents

| | | |
|-------|--|----|
| 1 | Introduction..... | 1 |
| 2 | Applications of 3D-measurement..... | 3 |
| 2.1 | Overview..... | 3 |
| 2.2 | 3D-Digitalization..... | 3 |
| 2.3 | 3D-Surface analysis..... | 3 |
| 2.4 | Reverse engineering..... | 4 |
| 2.5 | Quality inspection..... | 4 |
| 2.6 | Bin-picking..... | 5 |
| 2.7 | Vehicle safety..... | 5 |
| 2.8 | Biometry, cosmetics and medicine..... | 5 |
| 2.9 | Forensics and measurements of large areas..... | 6 |
| 3 | Theoretical basics of optics..... | 7 |
| 3.1 | Light as an electromagnetic wave..... | 7 |
| 3.2 | Color spectrum..... | 8 |
| 3.3 | Reflection and refraction of light..... | 9 |
| 3.4 | Dispersion of light..... | 10 |
| 3.5 | Polarization of light..... | 11 |
| 3.6 | Interference and diffraction of light..... | 12 |
| 3.7 | Optical aberrations..... | 14 |
| 3.7.1 | Chromatic aberration..... | 14 |
| 3.7.2 | Spherical aberration..... | 15 |
| 3.7.3 | Coma..... | 15 |
| 3.7.4 | Astigmatism..... | 15 |
| 3.7.5 | Curvature and distortion..... | 16 |
| 4 | Methods to acquire 3D-data..... | 17 |
| 4.1 | Tactile methods to acquire 3D-data..... | 17 |
| 4.2 | Non-contact methods to acquire 3D data..... | 18 |
| 4.2.1 | Optical methods..... | 18 |
| 4.2.2 | Acoustic methods..... | 39 |
| 4.2.3 | Magnetic methods..... | 39 |
| 4.3 | Practical problems of 3D-data acquisition..... | 40 |
| 4.3.1 | Calibration..... | 40 |
| 4.3.2 | Accuracy..... | 40 |
| 4.3.3 | Accessibility..... | 40 |
| 4.3.4 | Occlusion..... | 40 |
| 4.3.5 | Noise and incomplete data..... | 40 |
| 4.3.6 | Surface finish..... | 40 |
| 4.4 | Performance evaluation of 3D-data acquisition systems..... | 41 |
| 4.4.1 | Accuracy..... | 41 |
| 4.4.2 | Resolution..... | 41 |
| 4.4.3 | Speed..... | 41 |

| | | |
|-------|---|----|
| 4.4.4 | Primary performance space | 41 |
| 4.4.5 | Other requirements..... | 42 |
| 5 | Projection techniques | 43 |
| 5.1 | Basic principle..... | 43 |
| 5.2 | Light modulation | 43 |
| 5.2.1 | Slide projector..... | 43 |
| 5.2.2 | Movie projector | 44 |
| 5.2.3 | Rotational light modulator | 45 |
| 5.2.4 | Array Projector..... | 46 |
| 5.2.5 | CRT – Cathode Ray Tube | 48 |
| 5.2.6 | LCD – Liquid Crystal Display..... | 50 |
| 5.2.7 | LCoS – Liquid Crystal on Silicon | 61 |
| 5.2.8 | DLP – Digital Light Processing..... | 63 |
| 5.2.9 | Laser projector..... | 69 |
| 6 | Choosing the projection unit..... | 70 |
| 7 | Prototype of the projection unit | 74 |
| 7.1 | Sequence programming | 74 |
| 7.2 | Triggering of cameras..... | 77 |
| 7.3 | Luminous flux..... | 78 |
| 7.4 | Optics..... | 83 |
| 7.5 | Cooling..... | 87 |
| 8 | Summary and future work | 88 |
| 8.1 | Summary | 88 |
| 8.2 | Lightcrafter 6500..... | 88 |
| 8.3 | 3D-measurement system from ENSHAPE..... | 89 |

Figures

| | |
|---|----|
| Figure 1: Rendering of the Pick-it Easy Robot by KNAPP | 2 |
| Figure 2: Picking process of Pick-it-easy Robot by KNAPP..... | 2 |
| Figure 3: Main steps of the reverse engineering process (Zhou, 2011) | 4 |
| Figure 4: Light as an electromagnetic wave. The orientations of the electric and magnetic fields are indicated, as well as the direction of propagation. (Hebbeker, 2002) | 7 |
| Figure 5: Color spectrum which can be perceived by the human eye. It starts after the ultraviolet and ends before the infrared area. White light contains all colors represented in the spectrum. (Clive, 2013) | 8 |
| Figure 6: Chromaticity diagram which is used as the standard for color reproduction for electronic products. All colors have the same brightness. (Sakurambo, 2007)..... | 8 |
| Figure 7: Law of reflection: A light beam is emitted at point A and reflected at point R towards point B. The reflection law can be obtained from Fermat's principle by considering the mirror point B' of B. (Chen R. H., 2011, p. 67) | 9 |
| Figure 8: Snell's law of refraction: The light beam travels from point A with a velocity v_1 to point R where the refraction occurs. From point R on, the light travels in medium 2 with a different velocity v_2 until it reaches point B. (Chen R. H., 2011, p. 68) | 9 |
| Figure 9: Dispersion of light by a glass prism: visible light enters the prism and the wavelengths are refracted depending on the refractive index of the material. When the light leaves the prism, the light rays are refracted again and the full spectrum is visible on a screen. | 10 |
| Figure 10: Linear polarizer with a transmitting z-axis (Mellish, 2006) | 11 |
| Figure 11: The three types of polarization of electromagnetic waves. (Chen R. H., 2011, p. 60) | 11 |
| Figure 12: Propagation of a wave according to Huygens' principle (Schröder & Treiber, 2007, p. 21) | 12 |
| Figure 13: Diffraction of a perpendicular plane wave by a grating (left) (Schröder & Treiber, 2007, p. 24) and the wave propagation at a slit with a width greater than the wavelength of the incident wave (Nordmann, 2007) | 13 |
| Figure 14: Diffraction by a circular aperture (Schröder & Treiber, 2007, p. 25) | 14 |
| Figure 15: Chromatic aberration: The different colors are refracted differently due to the dependency of the refractive index of the lens on the wavelength. This causes a deviation of the focal points. (Demtröder, 2006, p. 277) | 14 |
| Figure 16: Spherical aberration: A deviation of the focal points for rays with different distances from the optical axis of the lens. (Demtröder, 2006, p. 279) | 15 |
| Figure 17: Coma: Deviation of the focal points caused by a tilted lens (a) or by an object point outside of the symmetrical axis (b). (Demtröder, 2006, p. 282) | 15 |
| Figure 18: Astigmatism: Can be observed when the image is far away from the optical axis. a) perspective view, b) cross section of the beam of light. (Demtröder, 2006, p. 283) | 16 |
| Figure 19: Curvature of the image plane. Depending on the distance of the object points from the symmetrical axis of the lens, the image is focused on curved surfaces which causes distortions. (Demtröder, 2006, p. 284) | 16 |
| Figure 20: 3D-data acquisition methods..... | 17 |
| Figure 21: Classification of optical 3D-measurement principles (Beyerer, León, & Frese, 2012, p. 431) | 18 |
| Figure 22: Triangulation principle: With the fixed angles α and β and the base b , the distance to the object point P can be calculated..... | 19 |
| Figure 23: Triangulation setup: The object point P is imaged by the lens onto point B of the detector. The Scheimpflug principle is employed as the planes of the object, the lens and the detector intersect each other in one straight line. (Beyerer, León, & Frese, 2012, p. 306) | 20 |
| Figure 24: Principle of stereo photogrammetry using two parallel cameras (Beyerer, León, & Frese, 2012, p. 342) | 21 |
| Figure 25: Epipolar geometry: Illustrated are the two image planes which display the object point x_w . Due to the epipolar geometry, the search area for x_2 is reduced to one epipolar line l_2 . By finding the corresponding point x_2 in image 2 to the point x_1 in image 1, the correspondence problem is solved. (Beyerer, León, & Frese, 2012, p. 343) | 22 |
| Figure 26: Point-by-point laser triangulation: the Scheimpflug principle is employed. (Beyerer, León, & Frese, 2012, p. 304) | 23 |
| Figure 27: Light section measurement: Height information h is obtained by the lateral displacement d of the detected light section and the angle θ . (Beyerer, León, & Frese, 2012, p. 309) | 23 |
| Figure 28: Flow chart of a typical fringe projection process (Gorthi & Rastogi, 2010)..... | 25 |
| Figure 29: De Bruijn circle (a) and De Bruijn pattern (b) (Geng, 2011)..... | 26 |

| | |
|---|----|
| Figure 30: Different M-arrays: (a) Pseudo-random binary array (Geng, 2011), (b) Multivalued pseudo-random array, (c) Color-coded pseudo-random array (Salvi, Pagès, & Batlle, 2004)..... | 26 |
| Figure 31: Pattern classification for sparse reconstruction methods (Navarro Fernández, 2012)..... | 27 |
| Figure 32: Pattern classification for dense reconstruction methods (Navarro Fernández, 2012)..... | 28 |
| Figure 33: Gray-code sequence projected onto an object (Beyerer, León, & Frese, 2012, p. 315) | 29 |
| Figure 34: 5-bit Gray-code sequence for 32 lines (Gühning, 2002)..... | 29 |
| Figure 35: Phase shifting reference plane principle. (Geng, 2011)..... | 30 |
| Figure 36: Deflectometry principle: A pattern is displayed on a screen and the reflection on the surface is observed by a camera. A computer then analyzes the distortions caused by surface defects. (Beyerer, León, & Frese, 2012, p. 320)..... | 31 |
| Figure 37: Comparison of the light path of structured light and deflectometry (Beyerer, León, & Frese, 2012, p. 322) | 31 |
| Figure 38: Generation of Moiré patterns by overlaying two patterns with: (a) varying gap width, (b) rotated orientation, (c) different magnification. (Beyerer, León, & Frese, 2012, p. 331) | 32 |
| Figure 39: Shadowing of the light source by a grating (Beyerer, León, & Frese, 2012, p. 339)..... | 32 |
| Figure 40: Light field: includes all possible images of the measured object. (Beyerer, León, & Frese, 2012, p. 350) | 33 |
| Figure 41: Light field camera principle: A micro lens array focuses different areas of the objective, for example area C, onto the imaging sensor which creates several images from different perspectives. (Beyerer, León, & Frese, 2012, p. 352)..... | 33 |
| Figure 42: Silhouette capturing method with bright field configuration. (Beyerer, León, & Frese, 2012, p. 356)..... | 34 |
| Figure 43: Confocal microscopy principle: Light (blue path) passes through an aperture and a dichroic mirror and is focused onto the object by a lens. The focused reflection by the object (red path) is deflected by the dichroic mirror onto a detector. An aperture blocks reflections by the object which are not focused (green path). (Beyerer, León, & Frese, 2012, p. 367) | 35 |
| Figure 44: Interferometer principle: Monochromatic light, usually from a laser, is split up into a reference wave (mirror) and measurement wave (object). The two waves are then superimposed and the interference is observed with a detector. (Beyerer, León, & Frese, 2012, p. 372)..... | 37 |
| Figure 45: Interferometer using white light. (Beyerer, León, & Frese, 2012, p. 378)..... | 38 |
| Figure 46: Measurement uncertainty of optical methods in relation to the measurement distance. (Schwarte, Häusler, & Malz, 2000, p. 180)..... | 39 |
| Figure 47: Primary performance space for 3D-measurement systems consisting of accuracy, speed and resolution. (Geng, 2011)..... | 41 |
| Figure 48: Basic principle of a projecting device | 43 |
| Figure 49: Slide projector principle: Light passes a lens system and illuminates a slide which contains the image. Projection lenses then focus the projection onto a screen..... | 43 |
| Figure 50: Movie projector principle: A film is fed from the upper spool and stopped at the gate. Light illuminates the image and a lens projects the image onto a screen. During the change of one image to the next, a rotating shutter blocks the light path. (Munday, 2006) | 44 |
| Figure 51: Concept of rotational pattern projection. (Wissmann, Forster, & Schmitt, 2011)..... | 45 |
| Figure 52: First (left) and second (right) generation of analogue pattern projection unit. (Wissmann, 2013)..... | 45 |
| Figure 53: Array projector principle: a projection group contains the same image and consists of a LED, a condenser lens array and a projection lens array. By powering the LED, the image is projected and the frame rate only depends on the switching speed of the LED. A macro lens focuses the images of the different projection groups. (Heist, Sieler, Breitbarth, Kühmstedt, & Notni, 2013)..... | 46 |
| Figure 54: Array projector and crystal wafer (top left) (Notni & Kühmstedt, 2013) | 47 |
| Figure 55: Cathode ray tube principle: the cathode, consisting of three electron guns, emits an electron beam which is deflected by two coils. A shadow mask assures that the correct phosphor on the faceplate is illuminated. (Wandell, 2012) | 48 |
| Figure 56: Luminance of a pulse-type display such as a cathode ray tube: For the black to white transition, the maximum luminance is reached shortly after the start of a new frame and decays over time. For the white to black transition, an inevitable activation of the phosphor occurs when the electron beam passes the phosphor. (Elze & Tanner, 2012)..... | 48 |
| Figure 57: Sony G70 CRT projector..... | 49 |
| Figure 58: Luminance of a hold-type display such as a liquid crystal display: For a black to white transition, the maximum luminance is reached after a certain amount of time. For a white to black transition, the LCD also requires time to reduce the luminance. (Elze & Tanner, 2012) | 50 |
| Figure 59: Structure of a liquid crystal cell: The backlight provides the illumination which is then linear polarized. The linear polarized light enters the liquid crystal layer and depending on the state of the | |

| | |
|---|----|
| crystal and the voltage at the electrodes, the light is modulated or not. The light then passes subpixel color filter (RGB) and a second linear polarizer either blocks or lets the light pass..... | 50 |
| Figure 60: Classification of liquid crystals into thermotropic and lyotropic liquid crystals. The thermotropic can be distinguished by their shape into calamatic and discotic liquid crystals and several others. The calamatic liquid crystals can have different phases such as nematic or smectic. (MERCK, 2015)..... | 51 |
| Figure 61: Mesophases of thermotropic liquid crystals: With increasing temperature, the solid crystal becomes liquid, which however does not occur instantly. The crystal transforms into several different mesophases with different alignment of the molecules. (Chen R. H., 2011, pp. 80, 92)..... | 51 |
| Figure 62: Helical superstructure caused by the introduction of chirality to the liquid crystal (Dierking, 2014)..... | 52 |
| Figure 63: Structure of Blue Phase I: The liquid crystal molecules are aligned in a double twist cylinder. The double-twist cylinders have cubic symmetry in the structure. (Kikuchi, 2010)..... | 52 |
| Figure 64: Temperature - Chirality diagram of the three different Blue Phases. Introducing chirality generates Blue Phase I, whose stability increases for increasing chirality. Blue Phase II is obtained for intermediate chirality. Blue Phase III is observed at maximum chirality and its stability also increases until it is dissolved at the critical point. (Dierking, 2014)..... | 52 |
| Figure 65: Rotation of the twisted nematic (TN) with positive anisotropy and of the vertical alignment (VA) with negative anisotropy. As a reaction to the applied electric field E the liquid crystal molecules will rotate in the effort to align the intrinsic electric dipole moment p to the electric field. (Chen R. H., 2011, p. 350)..... | 54 |
| Figure 66: Twisted nematic in normally white mode (Elze & Tanner, 2012)..... | 54 |
| Figure 67: Vertical alignment (VA) liquid crystals (Chen R. H., 2011, p. 370)..... | 55 |
| Figure 68: Multi-domain vertical alignment (MVA) liquid crystal. (Chen R. H., 2011, p. 373)..... | 55 |
| Figure 69: Patterned vertical alignment liquid crystal. (Chen R. H., 2011, p. 375)..... | 56 |
| Figure 70: In-plane switching (IPS) liquid crystal. (Chen R. H., 2011, p. 377)..... | 56 |
| Figure 71: Elastic deformation categories of liquid crystals: Splay, twist and bend. (Chen R. H., 2011, p. 102)..... | 57 |
| Figure 72: Innovation and differentiation in existing as well as in new liquid crystal technologies (MERCK, 2013)..... | 58 |
| Figure 73: Structure of a 3LCD projector: The white light is split up by a system of dichroic mirrors and each color illuminates one LCD panel. A prism then recombines the colors and guides the light into a projection lens. (DELIGHT 2000, 2013)..... | 59 |
| Figure 74: Dichroic prism: The blue and the red light are reflected, while the green light is transmitted. The three colors are combined to one projection..... | 59 |
| Figure 75: Structure of an LCoS cell. (Lenz & R ther, 2009)..... | 61 |
| Figure 76: Structure of an LCoS projector: The white light is split up into the primary colors by a system of dichroic mirrors. The three light beams then enter polarizing beam splitters (PBS) which let p-polarized beams pass and reflect s-polarized beams. When the polarization of the light is modulated by the LCoS chip from s-polarization to p-polarization, it passes the PBS and reaches a dichroic prism, where the RGB images are overlaid and guided to the projection optics. Otherwise the light is reflected and stays in the optical system. (Reichl, 2006)..... | 61 |
| Figure 77: Wire Grid: The unpolarized light is incident on the wire grid with an angle of 45° and the light transmitted by the wire grid and incident on the LCoS is p-polarized (JVC, 2007)..... | 62 |
| Figure 78: Digital light processing principle (left) (TI, 2013) and structure of a digital micro mirror device (right) (Kuhlmann & Paul, 2002)..... | 63 |
| Figure 79: DMD electrical schematic: The regions of electrostatic attraction are highlighted (Hornbeck, 2002)..... | 63 |
| Figure 80: Monostable, bistable and tristable mode of a DMD in relation to the bias voltage V_b (top) and effect of the applied address voltage ϕ_a for the bistable mode (bottom). (Motamedi, 2004, p. 406) ... | 64 |
| Figure 81: Address and reset sequence of the DMD (Hornbeck, 2002)..... | 65 |
| Figure 82: Different color wheels for DLP projectors (left) (Tsolis, 2009) and the structure of a 1DLP projector (right) (SITER, 2014)..... | 66 |
| Figure 83: Structure of a 3DLP projector: The light of a xenon lamp is incident on a TIR prism and split up by a system of dichroic prisms. Each of the three DLP chips reflects one of the primary colors which are then recombined by the prism systems and guided to the projection lens. Very precise optical elements and positioning is required..... | 66 |
| Figure 84: DMD micro mirror alignment. Diamond (left) (TI, 2013) and orthogonal (right) (TI, 2013) .. | 67 |
| Figure 85: Color wheels..... | 67 |
| Figure 86: Configuration for LED-based (top right) (TI, 2015), Laser-based (bottom right) (Chinnock, 2013) and Hybrid projectors (left) (Morrison, 2013)..... | 68 |
| Figure 87: Principle of a laser projector and a MEMS scanner (Freeman, Champion, & Madhavan, 2009)..... | 69 |

| | |
|--|----|
| Figure 88: Bidirectional raster scan (Freeman, Champion, & Madhavan, 2009) | 69 |
| Figure 89: Value benefit analysis of projectors: Consumer projectors with LCD, LCoS and DLP technology cannot process input signals with a frame rate that exceeds 120 Hz and are consequently not an option. The Lightcrafter modules score the highest overall score and are therefore selected. . | 72 |
| Figure 90: Lightcrafter 4500 (WINTECH, 2015) | 73 |
| Figure 91: GUI - Creating an image of the pattern sequence | 74 |
| Figure 92: GUI - Adding images and configurations to the firmware | 75 |
| Figure 93: GUI - Pattern sequence settings | 76 |
| Figure 94: Trigger of Lightcrafter 4500 (TI, 2014) | 77 |
| Figure 95: Lightcrafter 4500 Input and Output Connectors | 77 |
| Figure 96: IEC test pattern for projector calibration (a) and measurement points for illuminance measurement (b) according to IEC 61947-1:2002 (IEC, 2002)..... | 79 |
| Figure 97: Measurement M1, white light from standard LEDs, standard configuration. Measured values are in Lux. | 80 |
| Figure 98: Measurement M2, green standard LED, maximum current. Measured values are in Lux. . | 80 |
| Figure 99: Disassembly process of the Lightcrafter 4500 to change the LEDs | 81 |
| Figure 100: Wiring of LT3763 LED driver with LE CG P1W..... | 82 |
| Figure 101: Measurement M3, green high-power LED. Measured values are in Lux..... | 82 |
| Figure 102: Optical system of the Lightcrafter 4500 | 83 |
| Figure 103: Shrinking the source image and projecting it diagonally..... | 84 |
| Figure 104: Construction of the image generated by a thin lens (Demtröder, 2006, p. 273) | 84 |
| Figure 105: Self-made objective using an achromatic lens with a focal length of 35 mm from QIOPTIQ | 85 |
| Figure 106: Projection with self-made objective and observed distortions | 85 |
| Figure 107: Available space to mount the optics | 86 |
| Figure 108: Construction of the image generated by two lenses which are close to each other: The additional lens L_2 reduces the size of the image I' to the size of image I and moves it closer towards the lens. (Demtröder, 2006, p. 276) | 86 |
| Figure 109: Test of converging lens in front of projector to reduce the size of the image | 87 |
| Figure 110: Lightcrafter 6500 (top) (TI, 2014) and STAR-065 (bottom) (VIALUX, 2015) | 88 |
| Figure 111: Test container for the measurement by ENSHAPE (top), 3D point cloud (bottom left) and segmentation (bottom right)..... | 89 |

Tables

| | |
|--|----|
| Table 1: Technical specifications of the analogue pattern projection unit (Wissmann, 2013) | 46 |
| Table 2: Technical specifications array projector (Heist, Sieler, Breitbarth, Kühmstedt, & Notni, 2013) | 47 |
| Table 3: Technical specifications of CRT projectors (Palme, 2015) | 49 |
| Table 4: Technical specifications of the L3C07W-9x from EPSON (EPSON, 2014) | 60 |
| Table 5: DMD Chipsets by TI | 71 |
| Table 6: List of projectors which can process a 120Hz input and are inside the provided budget | 72 |
| Table 7: Overview of the available DLP Lightcrafter moduls | 73 |
| Table 8: Input trigger connector J11 pin assignment of the Lightcrafter 4500 | 77 |
| Table 9: Output trigger connector J14 pin assignment of the Lightcrafter 4500 | 78 |
| Table 10: Configurations of the Lightcrafter 4500 and the VisiLine VLG-02M..... | 78 |
| Table 11: Specifications of the LEDs of the Lightcrafter 4500 by OSRAM | 78 |
| Table 12: Parameters for luminous flux measurement | 79 |
| Table 13: Specifications of the LE CG P1W by OSRAM | 82 |
| Table 14: Specifications of the optics of the Lightcrafter 4500 (IVIEW DISPLAYS, 2014) | 83 |
| Table 15: Specifications of the Lightcrafter 6500 by VIALUX | 89 |

Abbreviations

| | |
|-------|---|
| ANSI | American National Standard Institute |
| BP | Blue Phase |
| CAD | Computer-Aided Design |
| CCD | Charge-Coupled Device |
| CMM | Coordinate Measuring Machine |
| CMOS | Complementary Metal-Oxide-Semiconductor |
| CRT | Cathode Ray Tube |
| D-ILA | Direct-drive Image Light Amplification |
| DC | Dark Chip |
| DIC | DIANIPPON INK AND CHEMICALS |
| DLI | DIGITAL LIGHT INNOVATIONS |
| DMD | Digital Micro-mirror Display |
| DLP | Digital Light Processing |
| FFS | Fringing Field Switching |
| FLC | Ferroelectric Liquid Crystals |
| FPD | Flat Panel Display |
| FSC | Field Sequential Color |
| GPIO | General-Purpose Input and Output |
| GUI | Graphical User Interface |
| Hz | Hertz |
| IEC | International Electromechanical Commission |
| IOF | Institut für angewandte Optik und Feinmechanik (FRAUNHOFER) |
| IPS | In-Plane Switching |
| IR | InfraRed |
| ITO | Indium Tin Oxide |
| JVC | VICTOR COMPANY OF JAPAN |
| LCD | Liquid Crystal Display |
| LCoS | Liquid Crystal on Silicon |
| LED | Light-Emitting Diode |
| LIDAR | Laser Illuminated Detection And Ranging |
| Lm | Lumen |
| MCP | Micro Clock Pulse |
| MEMS | MicroElectroMechanical Systems |
| MVA | Multi-domain Vertical Alignment |

| | |
|-------|--|
| PBS | Polarizing Beam Splitter |
| PRBA | Pseudo-Random Binary Array |
| PSI | Phase Shifting Interferometry |
| PVA | Patterned Vertical Alignment |
| PWM | Pulse Width Modulation |
| RGB | Red, Green and Blue (primary colors) |
| Rpm | Revolutions per minute |
| SHG | Second Harmonic Generation |
| SLM | Spatial Light Modulator |
| SONAR | Sound Navigation And Ranging |
| SXRD | Silicon X-tal Crystal Reflective Display |
| TFT | Thin Film Transistors |
| TI | TEXAS INSTRUMENTS |
| TIR | Total Internal Reflection |
| TN | Twisted Nematic |
| TV | TeleVision |
| USB | Universal Serial Bus |
| UV | UltraViolet |
| VA | Vertical Alignment |
| VIS | Visible Light |
| VSI | Vertical Scanning Interferometry |

1 Introduction

Digital image processing is a key technology with a high potential and plays an important part in a lot of existing applications in the whole value chain. Further applications are constantly developed in the field of manufacturing and automation, quality inspection and non-destructive examination. The advantage is that machine vision is independent of human fatigue, which leads to objective and replicable results. Additionally, sensors which work in the spectrum of non-visible light can make things visible to the human eye, which would otherwise be invisible. The application field and performance of image processing systems is constantly growing, mainly due to the increasing computing power, which enables real time processing. Thus, industrial image processing plays an important role as a connective link of several areas in the whole value chain, which provides the opportunity to establish automated and self-organized networks. The integration of 3D-measurement systems in the manufacturing process enables the discovering of deviations of quality as they emerge. This provides the possibility to take appropriate countermeasures during the production process. In addition, non-contact 3D-measurement systems are hardly limited to the dimensions and properties of the parts which need to be investigated. Important areas of future application include real time processing and moving parts, especially for guided robots. Ranging from bin-picking applications, which perform an automatic separation of loosely arranged parts in a container, to service robots which also have several application fields beyond the industrial area. (Notni, 2014)

In the field of structured light and triangulation, an object to be measured is sequentially illuminated by one or more measurement patterns to spatially encode its surface with respect to the origin of the illumination. In regards to the hardware, the bottleneck of the measurement is very often the projection frequency of the patterns to create the 3D-point cloud of an object. Cameras as well as computers are able to operate much faster and are available for kHz or even MHz frame rates, depending on size and budget limitations. Digital projection systems, which are commonly used for the structured light illumination of objects, are digital micro mirror devices (DMD), liquid crystal on silicon (LCoS) or liquid crystal display (LCD) devices. Other concepts include the use of a slide projector or lasers as an illumination source. Normally, a sequence of different or spatial modulated fringes is necessary for a robust and accurate determination of the coordinates of the measured object. (Patent No. DE102012206472A1)

When a sequence of patterns is used, the algorithms require stationary objects for the entire time of the projection and acquisition of the images. For dynamic applications where the measured object or the sensor system, or both, move relative to each other this condition is not satisfied. To fulfill the requirement of a quasi-static measurement situation, there are two possible approaches. On the one hand, adjustments to the software or the algorithm can be done by reducing the projection sequence, using alternative patterns or compensating the relative motion. On the other hand, modifications to the hardware such as increasing the projection and acquisition speed can be performed. (Breitbarth, 2014) Consumer products are very often not suitable for industrial applications and usually have the following disadvantages: (Patent No. DE102012206472A1)

- A luminous flux higher than 1000 Lumen (IEC)¹ typically requires a bigger construction size (min. 300 mm by 100 mm) and especially a bigger construction depth (bigger than 200 mm).
- To keep the projector ready, it has to run continuously, which requires sufficient cooling and also reduces its life-time.
- The frame rate is very often limited to 60 Hz or 120 Hz.

¹ Originally the measurement procedure was defined by the American National Standards Institute (ANSI), but the standards ANSI/NAPM IT7.228-1997 and ANSI/PIMA IT7.227-1998 became invalid in 2003. The International Electrotechnical Commission (IEC) defined the new standards IEC 61947-1:2001 and IEC 61947-2:2001, which equal the former ANSI standards and require the same testing procedures. Thus manufacturers still use the established terms Lumen (ANSI) or ANSI lumen.

Pick-it-Easy Robot by KNAPP:

The Pick-it-Easy Robot is a fully automatic commissioning unit which is designed for picking products out of a storage container and distribute them to commission containers. The products in the storage containers are arbitrarily packed. The Pick-it-Easy Robot is designed for the use in the pharmaceutical wholesale and the typical products in that branch. The robot cell, as shown in Figure 1, is built up of a robotic arm with an interchangeable pick unit, the image acquisition and processing software as well as the robot system controller.



Figure 1: Rendering of the Pick-it Easy Robot by KNAPP

The image acquisition and processing software detects the objects in the storage container and calculates the pick points of the objects for the robotic arm. The robot system controller then moves the robotic arm at the exact position so that the pick unit can pick the object. The chosen product is then picked with a vacuum suction cup and moved to the commission container. The process for one commission by the Pick-it-Easy Robot is illustrated in Figure 2.



Figure 2: Picking process of Pick-it-easy Robot by KNAPP

The Pick-it-Easy Robot cell is supplied with containers by a fully automatic storage system and can handle one or more commissions simultaneously. The robotic arm picks the necessary amount of products and the storage container is then returned to the storage system. The commission containers are transported to the next process step of the commission.

2 Applications of 3D-measurement

2.1 Overview

Photogrammetric procedures and systems for 3D-industrial measurements have increased in the last several years and gained increasing interest and importance, which is partly due to the developments in the area of digital image acquisition and processing. These developments led to a higher accuracy, faster data processing as well as a higher degree of automation. Systems can be categorized on the one hand into mobile, flexible online- and offline-systems, and on the other hand into stationary, process integrated systems, which both serve to acquire 3D-point coordinates or the profile of a surface. (Luhmann, 2014)

Industries which use 3D-measurement systems range from the medical industries to the aerospace and automotive industry over the manufacturing and consumer products industry to power generation industries. Typically, these industries use 3D-measurement systems for one or more of the following applications:

- 3D-Digitalization
- 3D-Surface reconstruction and analysis
- Reverse engineering
- Quality inspection
- Object recognition
- Robotic vision
- 3D-Image metrology
- Motion tracking
- 3D-Full-body-scanning for humans and other objects

In the remainder of this section some important applications of 3D-measurement systems are discussed.

2.2 3D-Digitalization

Computer-based surface models are used in several fields of science and engineering. On the one hand, the design and manufacturing of complex parts for cars and aircrafts would not be possible without highly advanced CAD and simulation tools which predict the behavior of the parts. On the other hand, designers in the automobile industry create very complex free form surfaces to generate an elegant design. Such surfaces are rather difficult to create on a CAD-system. Hence, designers usually start with freehand sketches and then continue with a clay or wooden model because these materials are rather cheap, widely available and easy to form into the desired shape. First studies regarding the aerodynamic properties of a new design are based on this handcrafted models. 3D-measurement systems are then used to generate a digital model of the first prototype, which is required in the subsequent steps of the development process. To describe complex shapes accurately a high object point density is necessary. These points combined are referred to as a point cloud, which can be created with different methods. Since a clay model is rather soft, contact measuring techniques such as coordinate measuring machines (CMM), are not suitable to obtain the necessary data as explained in chapter 4.1. Therefore, a non-contact measurement system is required. (AICON 3D SYSTEMS, 2014)

2.3 3D-Surface analysis

To measure reference parts, which are used to calibrate measurement equipment, highly precise 3D-measurement systems using digital holography can be used. They can also measure metallic objects, which are, for example, formed with a deep drawing process, and check the surface for defects and measure the thickness of the material and the roughness of the surface. Another field of application is the measurement of soldered joints of microelectromechanical systems (MEMS), which are mounted onto circuit boards. (Fratz, Beckmann, & Carl, 2014)

Usually, tactile measurement systems are used for the measurement of the roughness of a surface. This however, has the drawback of requiring contact between the surface and the touch probe, which might cause deformations. Alternatively, optical 3D-measurement systems can be used to perform such

a measurement, as, for example, confocal microscopes, white light interferometers or chromatic-confocal sensors.

2.4 Reverse engineering

Reverse engineering is the process of analyzing and reconstructing an already existing product and is used to extract knowledge, ideas and design philosophy from it, when such information is not available. By disassembling a product and measuring every component, the function or the design as well as the structure can be analyzed. To get a precise model of the different components of the disassembled product, 3D-measurement system can be used. If not only a CAD-model is desired, such measurement systems can be combined with a 3D-printer or any other rapid prototyping machine. (Eilam, 2005, pp. 3-4)

The traditional reverse engineering process, as summarized in Figure 3, consists of data acquisition, noise filtering, data reduction, curve filtering, surface fitting and CAD modeling. (Zhou, 2011)



Figure 3: Main steps of the reverse engineering process (Zhou, 2011)

As a result of a 3D-measurement for reverse engineering a set of data points is generated, ranging from point clouds to complete boundary representation models. Reverse engineering is used to perform benchmarking and develop competing products and supports the design of a new part or the copy of an already existing part. Very often the replacement for a damaged or broken part is either no longer available or simply too expensive. Then reverse engineering can be used to obtain the necessary information and reconstruct a CAD-model, which can then be used to manufacture the broken parts. Another application is to improve the precision of a CAD-model or inspect a numerical model. (Bagci, 2009)

2.5 Quality inspection

Inspection of manufactured components and their tolerances is at the heart of industrial quality inspection. High-speed 3D-measurement systems can be directly implemented into the manufacturing process, where they constantly control the quality in-between critical process steps. If deviations are detected, appropriate measures can be taken automatically without extensive stoppage. (Wernemünde, 2014)

Computer aided quality inspection can be used to compare the actual data of the physical object with the target data of the CAD-model. This can be used to check if parts are at the right position and have the correct orientation. If the assembly is then complete, the next process step can start. AIRBUS, for example, is using such a system in the assembly process of their planes. (Berndt & Trostmann, 2014)

Changes to the surface caused by warpage can be measured, as well as the deviations of size and position of holes and cutting edges of metal sheets. The measured 3D-data is transferred to the inspection software which contains the specifications of the inspection criteria of the CAD-model. The tolerances can be quantified, localized and the results can be visualized in various forms. Furthermore, the geometric accuracy of components, as well as their shape and the position of drilled holes can be verified. The 3D-data also allows the inspection of shape deviations caused by material properties, attrition, corrosion and ageing. The gathered data can then be used for the documentation and further testing. Quality inspection is used in a lot of different industries, especially in the automotive, aircraft, plant construction and power plant industry and is integrated in the production process. For example, AUDI is measuring their components to check if the hole pattern and trimming line are within the tolerances after the manufacturing process. (AICON 3D SYSTEMS, 2014)

WIRTHWEIN uses 3D-quality inspection for their plastic components, which are used in the railway, automotive, home appliances and electronics industries (AICON 3D SYSTEMS, 2014). GENERAL ELECTRICS measures turbine blades for aircrafts, which have highly complex free-form surfaces (AICON 3D SYSTEMS, 2014).

2.6 Bin-picking

Automated bin-picking applications are a very active research field. 2D-smart cameras are rather cheap and very compact and do not only capture images, but also analyze and evaluate them. This technology reaches its limits when the measurement task gets more complex and a precise measurement of the position and orientation of an object is required. 3D-measurement systems can be used to deal with more complex measurement tasks. 3D-smart cameras are, as of 2015, only used for rather simple tasks such as controlling the fill level of a tank or checking if certain parts are present in the captured scene. Flexible automation technologies in the manufacturing or distribution process are not widely-used. Incoming goods are often randomly arranged in a bin and are then separated with rather complex methods, using several mechanical components and conveyors, which are specially adapted to the product. For applications which have to deal with a wide variety of different and frequently changing products these solutions are not practical. One possible solution is to use a robotic arm which picks the unsorted parts directly from the bin or the belt conveyor. This however, requires a precise measurement of the position and the orientation of the objects. Several 3D-measurement systems are able to satisfy the requirements of such a task, ranging from light section scanners, to time-of-flight cameras and structured light projection systems (see chapter 4.2.1). For bin-picking applications which only have to deal with a few different objects, so-called best-fit algorithms are applied, which use cylinders, planes, cones, spheres or tori to detect the objects in the 3D-point cloud. Several different factors, which can significantly affect the result of the segmentation, have to be taken into account. The configuration of the system, concerning the preprocessing and the segmentation of the point cloud and the combination with the best-fit algorithms, is a very time-intensive task and is usually carried out by an expert for image processing following the trial-and-error principle. Consequently, the development of an algorithm which is able to learn and choose the correct configuration automatically is highly desirable and currently a very active field of research. Also, the implementation of a database which stores information about the dimensions and the properties of the different objects is a useful tool to support the segmentation. (Effenberger, 2014)

2.7 Vehicle safety

Some 3D-measurement systems can be used for highly dynamic scenes, which enables the analysis of the inflation of an airbag. The results are then the basis for the optimization of the airbag design thereby increasing driver and passenger safety. Also the analysis of crash tests and the intrusions during the impact is possible. This is important because very often the injury consequences do not only relate to the severity of the intrusions, which can be seen after the crash. They also relate to the location and velocity of the intrusion and the relative position of the people inside the car during the crash. High-speed measurement systems are able to capture and display the deformations of various parts of the vehicle while the crash test is performed. (Geng, 2011)

2.8 Biometry, cosmetics and medicine

Each part of a human body is almost unique and its surface can be reconstructed very well using 3D-measurement systems. The applications range from biometric face scanner, used for face recognition systems and for animations in the multimedia industry, to the planning of plastic surgery. Also in the field of dentistry applications are present, such as measuring the denture of a patient and creating a dental arch which fits into the tooth space. The same principle can also be applied to build a custom-fit hearing aid. (Geng, 2011)

Due to laws in the European Union, manufacturers in the cosmetic industry need to verify the advertised properties of their products by accurately measuring them in a scientific way. Some 3D-measurement systems are so accurate that they can be used to measure changes of the skin structure and therefore fulfill that task. The measurement happens fast, is safe for the skin and delivers an undisturbed measuring result of the human skin. (Frankowski & Hainich, 2009)

Another very interesting approach is to use 3D-measurement to capture fingerprints without requiring contact to the sensor as presented by Koller et al. (Koller, et al., 2011)

2.9 Forensics and measurements of large areas

Images of a traffic accident are seldom captured and the only possible way of reconstructing the actual accident is to interpret the things that are found at the scene. Thus 3D-measurement systems can be used to document the scene precisely and support the work of the authorities. The information gathered by the measurement can be used to simulate and re-enact the accident scene. (Geng, 2011)

Another application is the measurement of roads and landscapes, which can either be mounted on a plane or a vehicle on the ground.

3 Theoretical basics of optics

3.1 Light as an electromagnetic wave

Light can be described as an electromagnetic wave with an electric field vector \vec{E} and a magnetic induction vector \vec{B} , which are perpendicular to each other and perpendicular to the direction of propagation of the wave as shown in Figure 4.

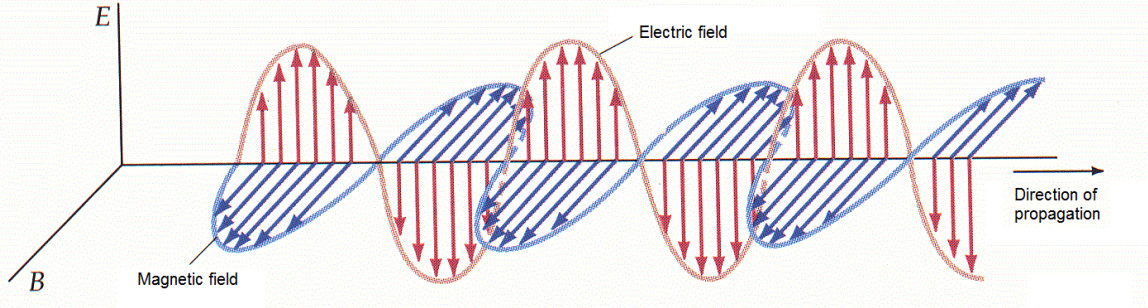


Figure 4: Light as an electromagnetic wave. The orientations of the electric and magnetic fields are indicated, as well as the direction of propagation. (Hebbeker, 2002)

Maxwell's four differential equations describe the interactions between the electric field \vec{E} and the magnetic field \vec{B} . Here \vec{D} denotes the electric flux density, ρ the free charge density, \vec{H} the magnetic field strength and \vec{j} the current density of free charge.

$$\text{Gauss's law for electric fields:} \quad \vec{\nabla} \cdot \vec{D} = \rho \quad (3.1)$$

$$\text{Gauss's law for magnetic fields:} \quad \vec{\nabla} \cdot \vec{B} = 0 \quad (3.2)$$

$$\text{Faraday's law:} \quad \vec{\nabla} \times \vec{E} = -\frac{\partial \vec{B}}{\partial t} \quad (3.3)$$

$$\text{Extension of Ampere's circuital law:} \quad \vec{\nabla} \times \vec{H} = \vec{j} + \frac{\partial \vec{D}}{\partial t} \quad (3.4)$$

In combination with the 3 material equations

$$\vec{B} = \mu \cdot \vec{H} \quad (3.5)$$

$$\vec{D} = \epsilon \cdot \vec{E} \quad (3.6)$$

$$\vec{j} = \kappa \cdot \vec{E} \quad (3.7)$$

where μ denotes the permeability, ϵ the permittivity and κ the electrical conductivity. For electromagnetic waves in vacuum $\vec{j} = 0$ and $\rho = 0$ the equations can be written as

$$\vec{\nabla} \cdot \vec{E} = 0 \quad (3.8)$$

$$\vec{\nabla} \cdot \vec{H} = 0 \quad (3.9)$$

$$\vec{\nabla} \times \vec{E} = -\mu \frac{\partial \vec{H}}{\partial t} \quad (3.10)$$

$$\vec{\nabla} \times \vec{H} = \epsilon \frac{\partial \vec{E}}{\partial t} \quad (3.11)$$

Taking the curl of (3.11) and substituting (3.10) yields

$$\vec{\nabla} \times (\vec{\nabla} \times \vec{H}) = \vec{\nabla} \times \left(\epsilon \frac{\partial \vec{E}}{\partial t} \right) = \epsilon \frac{\partial}{\partial t} (\vec{\nabla} \times \vec{E}) = -\mu \cdot \epsilon \frac{\partial^2 \vec{H}}{\partial t^2}. \quad (3.12)$$

Rewriting the cross product

$$\vec{\nabla} \times (\vec{\nabla} \times \vec{H}) = \vec{\nabla} \cdot (\vec{\nabla} \cdot \vec{H}) - \vec{\nabla}^2 \cdot \vec{H} \quad (3.13)$$

in (3.12) leads in combination with (3.9) to

$$\vec{\nabla} \times (\vec{\nabla} \times \vec{H}) = -\vec{\nabla}^2 \cdot \vec{H}. \quad (3.14)$$

Substituting (3.14) into (3.12) leads to

$$\vec{\nabla}^2 \cdot \vec{H} - \mu \cdot \epsilon \frac{\partial^2 \vec{H}}{\partial t^2} = 0. \quad (3.15)$$

The same can be done with (3.11) in (3.10) which yields

$$\nabla^2 \cdot \vec{E} - \mu \cdot \varepsilon \frac{\partial^2 \vec{E}}{\partial t^2} = 0. \quad (3.16)$$

The two equations (3.15) and (3.16) have the same form as a sound wave in air or in water. The equation for a sound wave propagation through a medium with velocity v can be described with

$$\nabla^2 \cdot p - \frac{1}{v^2} \frac{d^2 p}{dt^2} = 0 \quad (3.17)$$

where p is the acoustic pressure. From the similarity of (3.15), (3.16) and (3.17) it can be deduced that

$$\varepsilon \cdot \mu = \frac{1}{v^2}. \quad (3.18)$$

Which leads to the following expression for the speed v of an electromagnetic wave

$$v = \frac{1}{\sqrt{\varepsilon \cdot \mu}}. \quad (3.19)$$

In vacuum where $\varepsilon = \varepsilon_0 = 8,8541878 \frac{As}{Vm}$ and $\mu = \mu_0 = 4\pi \cdot 10^{-7} \frac{Vs}{Am}$, the speed of an electromagnetic wave is

$$v = \frac{1}{\sqrt{8,8541878 \cdot 4\pi \cdot 10^{-7}}} = 299,792.458 \frac{m}{s} \quad (3.20)$$

which is exactly the speed of light in vacuum. (Chen, 2011, pp. 25-28)

Since light is an electromagnetic wave, electrical charges and currents can be used to modulate light.

3.2 Color spectrum

The color spectrum of light as a function of the wavelength is shown in Figure 5.

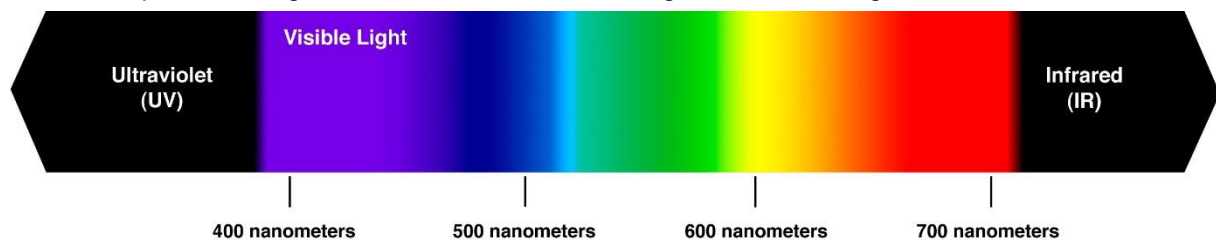


Figure 5: Color spectrum which can be perceived by the human eye. It starts after the ultraviolet and ends before the infrared area. White light contains all colors represented in the spectrum. (Clive, 2013)

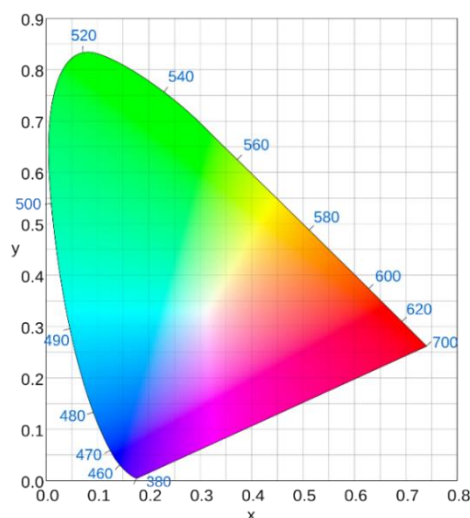


Figure 6: Chromaticity diagram which is used as the standard for color reproduction for electronic products. All colors have the same brightness. (Sakurambo, 2007)

The range of optical radiation (100 nm to 1 mm) covers the regions ultraviolet (UV), visible light (VIS) and infrared (IR). The wavelengths of visible light lie between 380 and 780 nm. Any color can be generated by mixing the three primary colors red, green and blue (primary means that neither of these three colors can be generated by combining the other two). So, color can be represented by a vector in a three-dimensional coordinate system, with the components encoding the contribution of the three primary colors

$$Color = rR + gG + bB \quad (3.21)$$

A certain color can then be defined by the red, green and blue color coordinates as a point in space. In the chromaticity diagram shown in Figure 6 all the colors have the same brightness, which reduces the three-dimensional space to a two-dimensional plane which is used as a standard for color reproduction for electronic products. (Chen R. H., 2011, pp. 328-333)

3.3 Reflection and refraction of light

The incident light is reflected from a mirror according to the law of reflection, which states that the angle of reflection of a beam of incident light on a plane mirror will be equal to the angle of incidence. If the incident beam would pass through the mirror as illustrated in Figure 7 then, as per Euclid's geometry, the straight line ARB' is the shortest distance between point A and B' .² The path ARB is only the shortest distance, if the angle of reflection θ_r is equal to θ'_r , which from simple geometry is equal to the angle of incidence θ_i . The propagation of the light beam in different mediums can be described by Fermat's principle, which states that a ray of light follows the path which takes a minimum time. (Chen R. H., 2011, pp. 66-67)

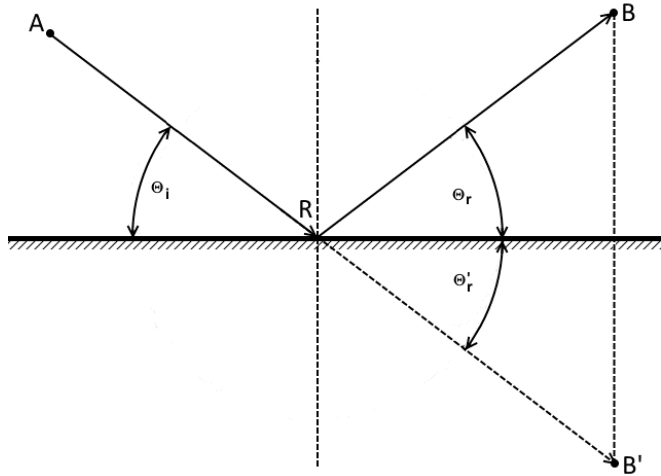


Figure 7: Law of reflection: A light beam is emitted at point A and reflected at point R towards point B . The reflection law can be obtained from Fermat's principle by considering the mirror point B' of B . (Chen R. H., 2011, p. 67)

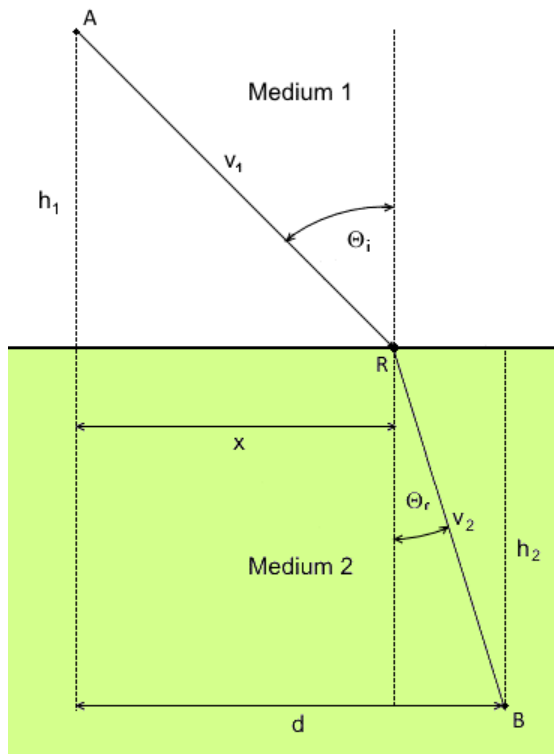


Figure 8: Snell's law of refraction: The light beam travels from point A with a velocity v_1 to point R where the refraction occurs. From point R on, the light travels in medium 2 with a different velocity v_2 until it reaches point B . (Chen R. H., 2011, p. 68)

The refractive index is defined as the ratio of the speed of light in vacuum and the phase velocity of the light in the medium.

$$n_i = \frac{c}{v_i} \quad (3.22)$$

A derivation of Fermat's principle is Snell's law, which describes the change in direction of the ray of light when it passes through a different medium as illustrated in Figure 8.

The distances \overline{AR} and \overline{RB} can be calculated by using the Pythagorean Theorem, which leads to

$$\overline{AR} = \sqrt{h_1^2 + x^2} \quad (3.23)$$

$$\overline{RB} = \sqrt{h_2^2 + (d-x)^2} \quad (3.24)$$

Thus the time T , which is required to travel from A to B , is

$$T = \frac{\sqrt{h_1^2 + x^2}}{v_1} + \frac{\sqrt{h_2^2 + (d-x)^2}}{v_2}. \quad (3.25)$$

Further the sinus of the incident and the refraction angle are

$$\sin \theta_i = \frac{x}{\sqrt{h_1^2 + x^2}} \quad (3.26)$$

$$\sin \theta_r = \frac{d-x}{\sqrt{h_2^2 + (d-x)^2}}. \quad (3.27)$$

² Note that in Einstein's general theory of relativity, the shortest distance between two points must not be a straight line because of the curvature of space and time.

The calculation of the minimum of (3.25) can be done with

$$\frac{dT}{dx} = \frac{1}{2} \cdot \frac{1}{v_1} \cdot \frac{2x}{\sqrt{h_1^2+x^2}} + \frac{1}{2} \cdot \frac{1}{v_2} \cdot \frac{-2(d-x)}{\sqrt{h_2^2+(d-x)^2}} = 0 \quad (3.28)$$

And thus

$$\frac{x}{v_1 \sqrt{h_1^2+x^2}} - \frac{d-x}{v_2 \sqrt{h_2^2+(d-x)^2}} = 0. \quad (3.29)$$

With (3.22), (3.26) and (3.27), this leads to Snell's law (Chen R. H., 2011, pp. 67-69)

$$\frac{\sin \theta_i}{\sin \theta_r} = \frac{v_1}{v_2} = \frac{n_2}{n_1}. \quad (3.30)$$

3.4 Dispersion of light

If light enters a non-absorbing homogenous material, such as glass or plastic, reflection and refraction occurs at the boundary surface and the incident visible light is separated into the color spectrum as displayed in Figure 5. This effect is called dispersion. The refractive index n of the material is a function of the light's wavelength and as a result each color is refracted by a different angle. Because shorter wavelengths have a lower velocity in the material, red light is usually refracted the least amount and blue light is refracted the most. The light rays are refracted twice, once when entering the prism and once when leaving the prism as displayed in Figure 9. (ZEISS, 2013)

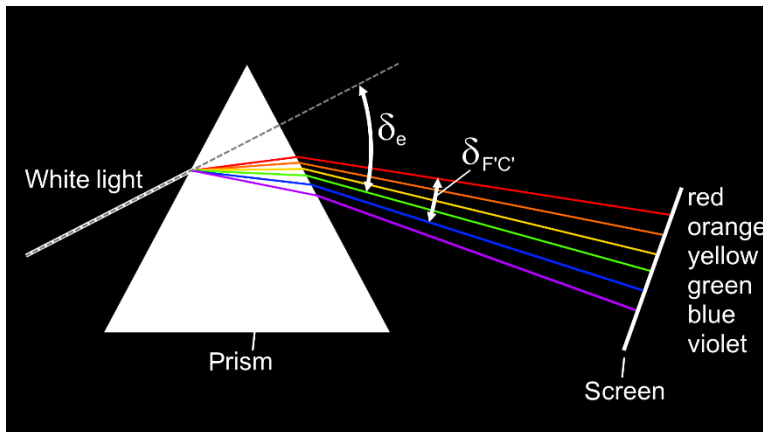


Figure 9: Dispersion of light by a glass prism: visible light enters the prism and the wavelengths are refracted depending on the refractive index of the material. When the light leaves the prism, the light rays are refracted again and the full spectrum is visible and a screen.

Transparent materials having a high refractive index usually have a high dispersion, which means a low Abbe number. A more detailed characterization of the relation between the refractive index and the wavelength is given by Cauchy's equation, which was further developed by Sellmeier to also describe the ultraviolet and infrared regions. Both equations use empirically determined coefficients. (SCHOTT, 2014, pp. 2-5)

Dispersion can be a desirable effect, for example, when used to construct spectrometers, or an undesirable effect of lenses used in cameras, telescopes, projectors or microscopes. This chromatic aberration can be prevented by using achromatic lenses as discussed in more detail in section 3.7.1.

The dispersion of a transparent material can be characterized by the Abbe number which is defined as

$$v_e = \frac{n_e - 1}{n_{F'} - n_{C'}} = \frac{\delta_e}{\delta_{F'C'}}, \quad (3.31)$$

where δ_e denotes the refraction angle of green and $\delta_{F'C'}$ the angle between the red and the blue area. $n_e, n_{F'}$ and $n_{C'}$ denote the refractive indices at 546.07 nm (green Mercury line), 479.99 nm (blue Cadmium line) and 643.85 nm (red Cadmium line) respectively. (ZEISS, 2013)

Transparent materials having a low refractive index usually also have a low dispersion, which means a high Abbe number. Transparent

3.5 Polarization of light

Naturally occurring light is unpolarized, which means that the direction and magnitude of the resultant electric and magnetic field vector vary rapidly and randomly in time. By convention the polarization of light refers to the polarization of the electric field. To analyze how a certain material influences the polarization of light, linear polarized light is used which is gained from unpolarized light when passing through a linear polarizer as shown in Figure 10. A linear polarizer transmits only the vector component which is aligned with the polarizer's transmitting axis and blocks all the other components. (Chen R. H., 2011, pp. 49-50)

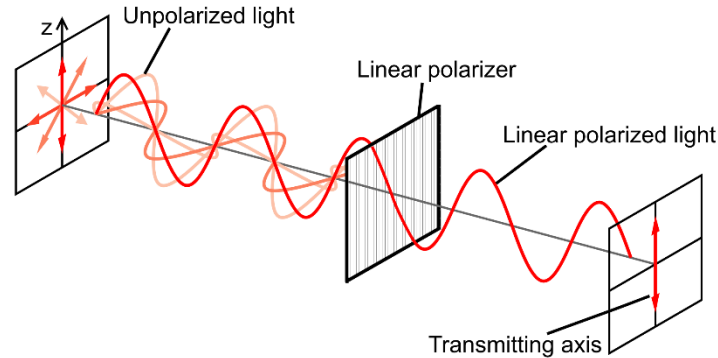


Figure 10: Linear polarizer with a transmitting z-axis (Mellish, 2006)

The probe, which needs to be investigated, is put in between two linear polarizers, the second one also being called the analyzer. By looking through the analyzer, the influence of the structure of the probe on the linear polarization state of the incident light can be seen. If the analyzer is aligned in the same way as the polarizer and the intensity of the light does not change, then the investigated probe does not change the polarization of the light. However, if there is a modulation in the intensity of the light, then the investigated probe does change the polarization of the incident light beam. A change does only occur if the material is anisotropic, which means that the indices of refraction of the material are different in different directions. If the material is isotropic, as for example transparent glass, then no modulation occurs. The different types of polarization which can occur, are shown in Figure 11. (Chen R. H., 2011, pp. 61-63)

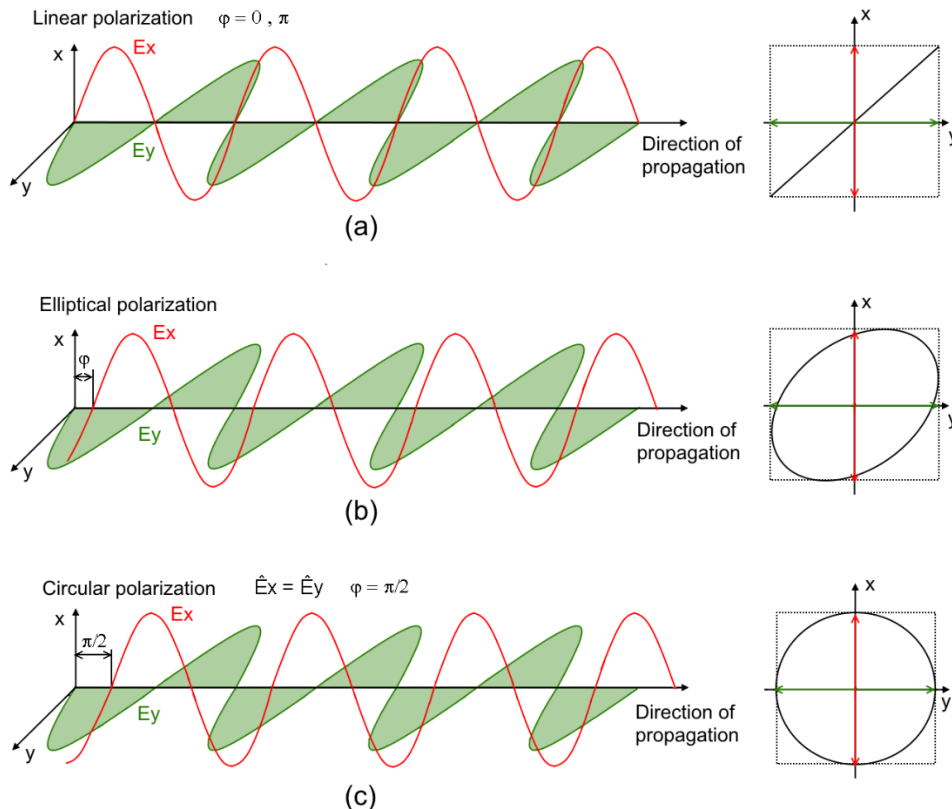


Figure 11: The three types of polarization of electromagnetic waves. (Chen R. H., 2011, p. 60)

Anisotropic crystals are usually birefringent, which means that an incident unpolarized light beam is split into two separate light beams taking slightly different paths depending on the refractive indices. One light beam passes through the crystal along the axis of the effective higher refractive index n_e (extraordinary beam) and a second one follows the axis of the effective lower refractive index n_o (ordinary beam). (Chen R. H., 2011, pp. 64-65)

If a linearly polarized light beam hits an anisotropic crystal with its \vec{E} vector at an arbitrary angle, then the electric field vector can be described by its components \vec{E}_x and \vec{E}_y as illustrated in Figure 11. Due to the anisotropy of the crystal, the speed of the two components through the crystal is different. This causes a phase difference φ between the electric field vector components. The magnitude of the phase difference depends on the refractive indices of the crystal and causes a change of the polarization of the light. The incident angle determines the magnitude of the amplitudes of E_x and E_y and as a consequence the type of polarization. (Chen R. H., 2011, pp. 53-54)

The most general state of polarization is the elliptical polarization for which the phase difference and the magnitudes of the amplitudes of E_x and E_y are arbitrary as illustrated in Figure 11 (b). The polarization of the incident linearly polarized light does not change due to the crystal if the caused phase difference is a multiple of π ($\varphi = n\pi$ with $n = 0; 1; 2; \dots$) as displayed in Figure 11 (a). If the amplitudes of E_x and E_y are equal and additionally the phase difference between E_x and E_y is an odd multiple of $\frac{\pi}{2}$ ($\varphi = (2n + 1)\frac{\pi}{2}$ with $n = 0; 1; 2; \dots$), then the rotation of the resulting electric field vector describes a circle as displayed in Figure 11 (c). The amplitudes of E_x and E_y are equal if the linearly polarized beam of light is incident on the crystal at an angle of 45° with respect to the effective refractive indices. (Chen R. H., 2011, pp. 59-61)

3.6 Interference and diffraction of light

Huygens' construction states that every point of a wave front can be considered as a center of a secondary disturbance which propagates in the form of spherical wavelets. The wavelets create disturbances in other regions and the superposition of all waves results in the observed propagation in Figure 12. (Schröder & Treiber, 2007, pp. 21-22)

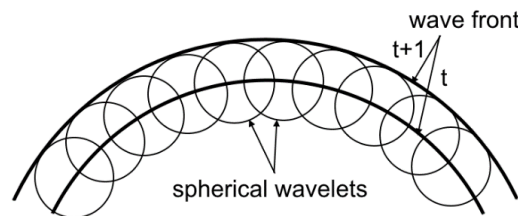


Figure 12: Propagation of a wave according to Huygens' principle (Schröder & Treiber, 2007, p. 21)

If two or more light waves with the same polarization plane and similar frequencies meet at a point in space, the contribution and position of the field components E_i can be superimposed on each other. This superimposition does not take place if the field amplitudes are oriented perpendicular to each other. The result of the superimposition depends on the phase difference $\Delta\varphi$ of the waves, which can be written as

$$\Delta\varphi = \frac{2\pi}{\lambda} \cdot n \cdot \Delta z, \quad (3.32)$$

in which λ is the wavelength in vacuum, n is the refractive index and Δz is the offset in the path lengths. If two waves with the same wavelength and polarization plane meet each other, two types of interference can occur:

1. They are in phase (the phase difference is a multiple of $2\pi \rightarrow \varphi = k \cdot 2\pi$) then the amplitude of the resulting wave increases. This is a constructive interference, which leads to an increase in light intensity.
2. If the waves have exactly the opposite phase (the phase difference is an odd multiple of $\pi \rightarrow \varphi = (2k + 1) \cdot \pi$), then the amplitude of the resulting wave decreases. This is a destructive interference which leads to a decrease in light intensity. In the special case that the waves have equal amplitudes, they cancel each other out, which results in zero intensity. (Schröder & Treiber, 2007, pp. 21-22)

The optical path difference is defined as

$$\delta = \frac{\lambda}{2\pi} \Delta\varphi. \quad (3.33)$$

And the conditions for interference can then be written as

$$\delta = k\lambda \quad \text{for constructive interference} \quad (3.34)$$

$$\delta = \frac{\lambda}{2} + k\lambda \quad \text{for destructive interference} \quad (3.35)$$

Huygens' principle however is only valid in spaces with an odd number of dimensions and does not properly describe diffraction. Diffraction is the interference of waves by physical objects. The diffraction is especially strong by objects which have dimensions in the area of the wavelength of the light. The Huygens-Fresnel principle combines Huygens' principle with Fresnel's principle of interference to describe diffraction near and far away from the object. The Fraunhofer diffraction on the other hand describes the behavior of waves at infinite distance from the object, but it can also be used to describe diffraction far away from the object. Both principles include undetermined factors and expressions. A sound mathematical description was carried out by Kirchhoff with the Fresnel-Kirchhoff diffraction formula, which by approximations leads back to the Huygens-Fresnel and the Fraunhofer diffraction. (Born & Wolf, 1970, pp. 370-381)

For technical applications two cases are relevant. The diffraction by a grating and the diffraction by a circular aperture. Optical gratings are periodical structures, mostly parallel lines at constant gap width and separation, which influence the amplitudes or the phase of the transmitted light wave or both. The wave is diffracted at the grating and spherical waves are generated at the slits. These spherical waves interfere with each other and form intensity maxima and minima. Figure 13 shows the diffraction of a flat wave front that hits a grating which is parallel to it. If the wave is incident at a certain angle ε , the grating formula can be written as

$$\sin \beta_{max} = \frac{m\lambda}{g} + \sin \varepsilon, \quad (3.36)$$

where β_{max} are the diffraction angles of the intensity maxima, λ is the wavelength, g is the grating constant and ε is the incident angle. (Schröder & Treiber, 2007, pp. 24-26)

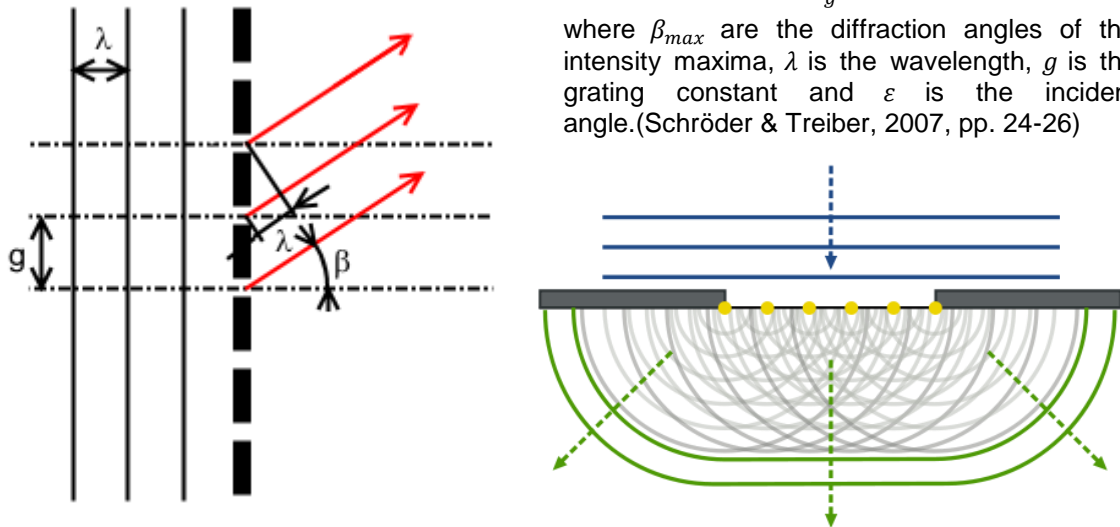


Figure 13: Diffraction of a perpendicular plane wave by a grating (left) (Schröder & Treiber, 2007, p. 24) and the wave propagation at a slit with a width greater than the wavelength of the incident wave (Nordmann, 2007)

Figure 14 shows a plane wave front which is incident on a circular aperture. If no diffraction would occur, the intensity on the screen would be described by the red rectangular graph. When the diameter d of the aperture becomes comparable to the wavelength, diffraction occurs and spherical wavelets (red and blue) are generated. These waves interfere with each other and the intensity on the screen changes. The pattern on the screen consists of a bright disc in the center, surrounded by concentric dark and bright rings, whose diameters increase if a smaller d is chosen. The intensity of the bright rings decreases rapidly with their radius. (Schröder & Treiber, 2007, pp. 24-26)

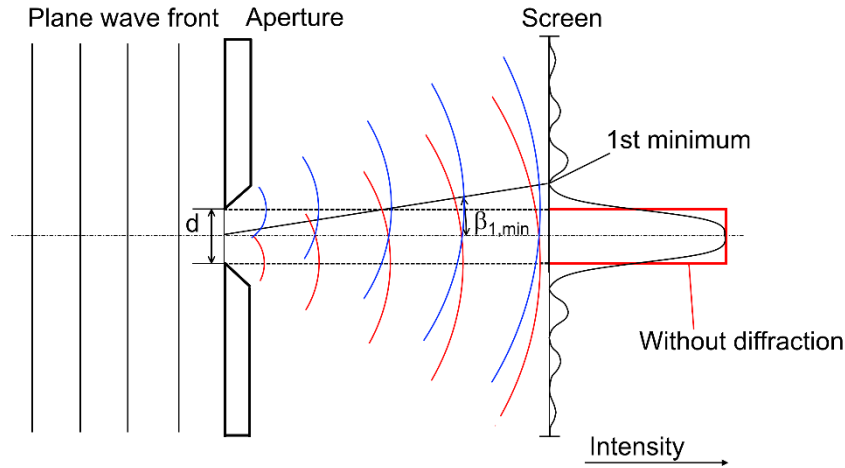


Figure 14: Diffraction by a circular aperture (Schröder & Treiber, 2007, p. 25)

The radius of the first dark circle is defined as the radius of the Airy disc, which increases with the distance between aperture and screen and the angle $\beta_{1,min}$ which can be written as

$$\sin \beta_{1,min} = 1.22 \frac{\lambda}{d} \tag{3.37}$$

3.7 Optical aberrations

In the field of optics, aberrations are deviations from the ideal image caused by an optical system. For an ideal optical system, a beam of light passes co-axial and all rays of that beam intersect each other in one point after the optical system. For a real optical system, where the rays are further away from the optical axis and are not co-axial, this is not the case and a certain degree of distortions always exists. As a result, certain areas of the image are defocused and distorted, which is especially a problem for applications which have to image very small structures. (Aldiek, Naumann, Gottfried, & Löffler-Mang, 2014, p. 107)

3.7.1 Chromatic aberration

Since the refractive index of the material of the lens is dependent on the wavelength of the light, the focal length of the lens is different for different colors. Hence, the red component of the white light is less refracted than the green and blue components as illustrated in Figure 15.

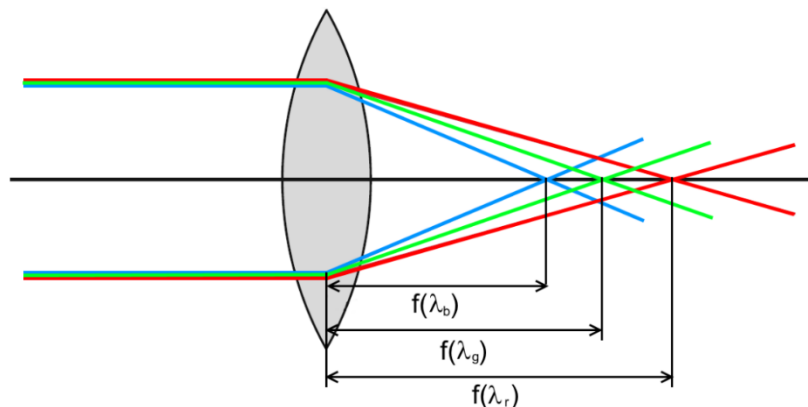


Figure 15: Chromatic aberration: The different colors are refracted differently due to the dependency of the refractive index of the lens on the wavelength. This causes a deviation of the focal points. (Demtröder, 2006, p. 277)

The chromatic aberration can be partly reduced by using a system of two lenses with different refractive indices. This so called achromatic lens consists of a biconvex converging lens and diverging lens which are glued together. (Demtröder, 2006, pp. 277-278)

Another possibility is to only use mirrors as, for example, in a reflecting telescope.

3.7.2 Spherical aberration

Deviations of the image can also occur when using monochromatic light as illumination as displayed in Figure 16. The focal length of the lens depends on the distance of the individual light rays from the optical axis. The spherical aberration furthermore depends on the shape of the lens and the object distance.

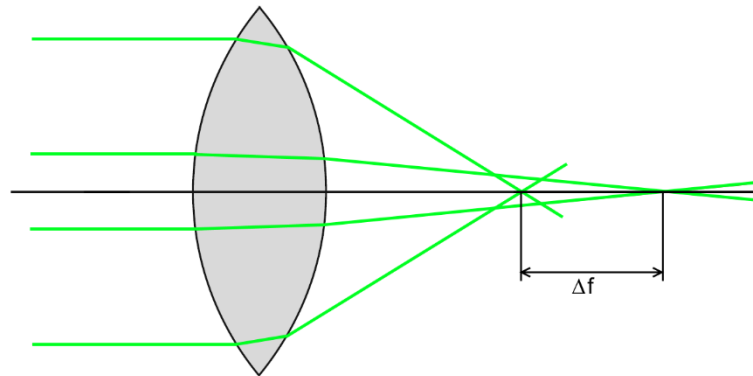


Figure 16: Spherical aberration: A deviation of the focal points for rays with different distances from the optical axis of the lens. (Demtröder, 2006, p. 279)

The spherical aberration can be partly reduced with an aperture, a plan-convex-lens, a combination of different diverging and converging lenses or with optimized aspheric lenses. (Demtröder, 2006, pp. 279-281)

3.7.3 Coma

If the beam of light is not co-axial with the axis of the optical system, the refraction angles do not only depend on the distance to the axis, but also if they are above or below the axis. The focal points of the individual rays are not positioned on the central beam anymore. This effect can either occur when the lens is tilted (a), or when the imaged object point is outside of the symmetrical axis (b) as shown in Figure 17. (Demtröder, 2006, pp. 281-282)

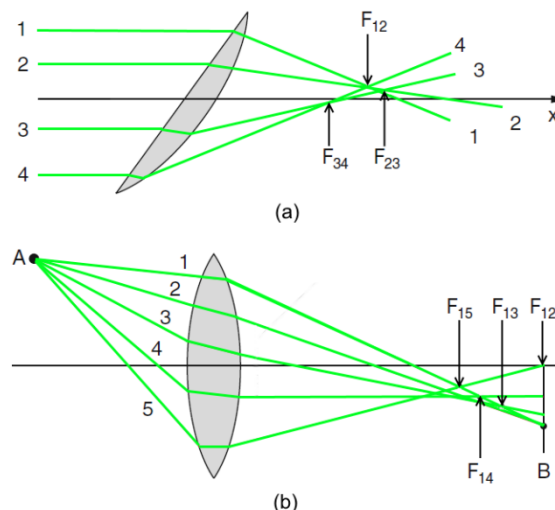


Figure 17: Coma: Deviation of the focal points caused by a tilted lens (a) or by an object point outside of the symmetrical axis (b). (Demtröder, 2006, p. 282)

3.7.4 Astigmatism

Astigmatism occurs if the image is far away from the axis. A beam of light which is coming from an object point A outside of the symmetry axis is incident on a lens at a certain angle. All rays of the beam in the tangential plane are focused in point B_T at an image distance of b_T . All rays of the radial plane however are imaged in a different point B_R at an image distance b_R which is smaller than b_T . This is due to the

fact that rays travelling along $\overline{AR_1}$ are more strongly refracted than the rays travelling along $\overline{AT_1}$. This results in a horizontal image line B_R at $x = b_R$ and a vertical image line B_T at $x = b_T$, instead of an image point B as displayed in Figure 18 a). Figure 18 b) shows the cross section of the beam of light at the different image distances.

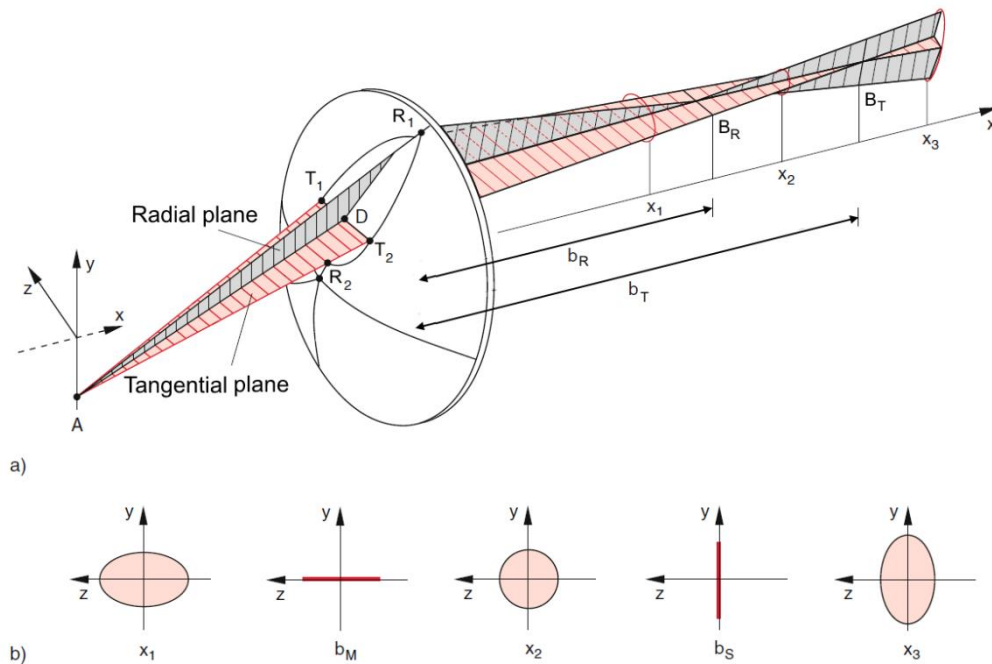


Figure 18: Astigmatism: Can be observed when the image is far away from the optical axis. a) perspective view, b) cross section of the beam of light. (Demtröder, 2006, p. 283)

The distance $dx = b_T - b_R$ increases when the beam of light has a steeper incident angle. Astigmatism can also occur when a beam of light shines through a plane parallel glass plate. Astigmatism can be corrected with an aspheric lens which also has a cylindrical curvature. (Demtröder, 2006, pp. 282-283)

3.7.5 Curvature and distortion

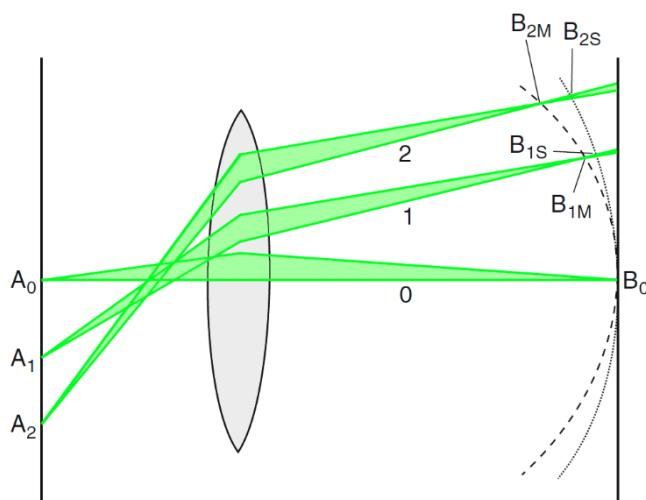


Figure 19: Curvature of the image plane. Depending on the distance of the object points from the symmetrical axis of the lens, the image is focused on curved surfaces which causes distortions. (Demtröder, 2006, p. 284)

The image distances i_i of different object points A_i depend on the distance of these object points to the symmetrical axis which is due to the different refraction angles of the light rays which pass the optical system. The resulting image is then in focus on two curved surfaces B_M (for the rays in the perpendicular or median plane) and B_S (for the rays in the horizontal or sagittal plane) as illustrated in Figure 19. The distortion can either have the shape of a barrel or a pincushion. Tele optics tend to have a pincushion distortion, whereas fisheye optics cause a strong barrel distortion. (Demtröder, 2006, pp. 283-285)

4 Methods to acquire 3D-data

Methods to acquire 3D-data are widely used in all kinds of different fields of applications ranging from quality inspection in the manufacturing process to digitalization of objects for 3D-printing or medicine (dental imprint), criminalistics (forensics), archeology and many more. Depending on the field of application a variety of measurement principles and sensors are used. After reviewing the most important measuring techniques, the advantages and limitations associated with these methods are pointed out. Figure 20 shows the classification of data acquisition methods for surfaces which can either be tactile or non-contact methods.

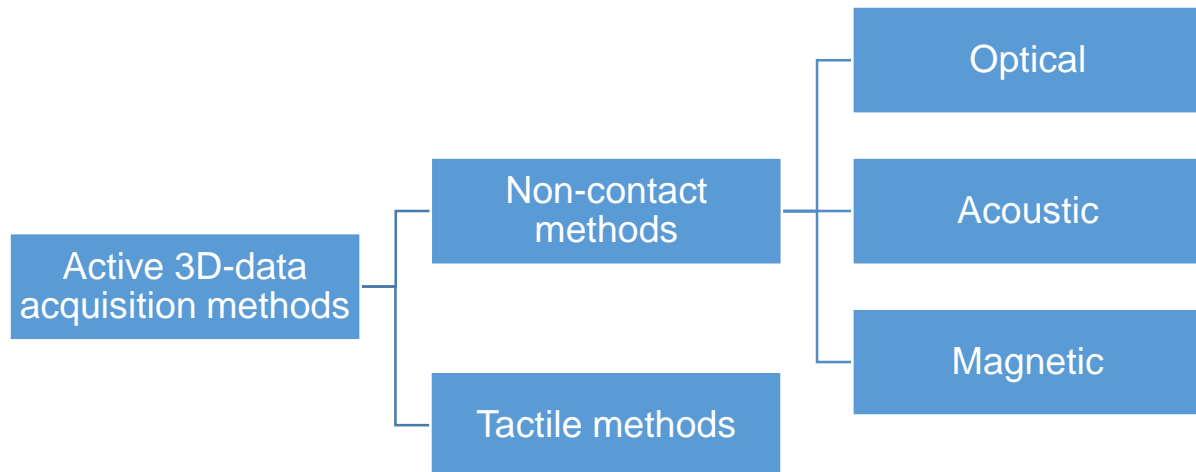


Figure 20: 3D-data acquisition methods

4.1 Tactile methods to acquire 3D-data

Tactile methods are popular and highly advanced ways of measuring and testing objects and their tolerances in the field of industrial quality inspection and manufacturing processes. The two main types are coordinate measuring machines (CMM) and robotic arms with a touch probe sensing device. CMMs are very robust and precise and they can be programmed to follow paths along a surface and collect very accurate, nearly noise-free data. The sensing probe registers the object point-by-point. It is also possible to automate the measuring process of gathering the information, analyzing the data and transmitting the data to a computer aided quality system. The second type of contact methods are robotic arms fitted with a touch probe which are used as a tactile measuring system. The probe head is the most important part of tactile methods, since it is the interface between the measuring device and the objects' surface. Tactile methods are a relatively slow way of data acquisition, since they can only measure point-by-point or linear. There are also several disadvantages of using a tactile method to measure the surface of a part. Due to the working principle, contact to the surface of the measured object is required. This however, can influence the object itself, especially if it is soft. Difficulties also occur when measuring complex free-form surfaces. If the part has very small indentations, the touch probe sensing device is not able to measure the surface completely. Furthermore, if the part is very flexible, the contact may create elastic or plastic deformations which lead to an inaccurate model of the object. For CMM, geometric complexity increases the number of points required for an accurate model. The time needed to capture points can range from hours to sometimes even days for very complex parts. Also external factors like temperature, vibrations and humidity can affect the measurement significantly. Tactile methods are still extensively used to measure the roughness of the surface of an object. (Gühring, 2002)

4.2 Non-contact methods to acquire 3D data

Non-contact methods acquire the shape of an object by using light waves, sound waves or magnetic fields. The non-contact 3D-measuring methods have the same underlying principles as the tactile methods. All of the measuring schemes need object points which are defined in a three dimensional coordinate system. The main differences are the number of object points and the way how these object points are obtained, as well as the analysis and visualization options. (de Felice, Petrillo, & Carlomusto, 2014)

4.2.1 Optical methods

Optical measurement systems for 3D-measurements typically consist of a light source, which is also called “sender”, the measured object which is illuminated by the light source, and a “receiver” which records the reflected light signals. The object causes distortions and changes the amplitude, phase, polarization or direction of the light signal which is then measured. By analyzing the change caused by the object, the 3D-information and the surface of the object can be reconstructed. Optical methods have the fastest acquisition rates of the non-contact methods and for that reason are the most popular ones. Figure 21 shows the classification of optical 3D-measurement principles. (Beyerer, León, & Frese, 2012)

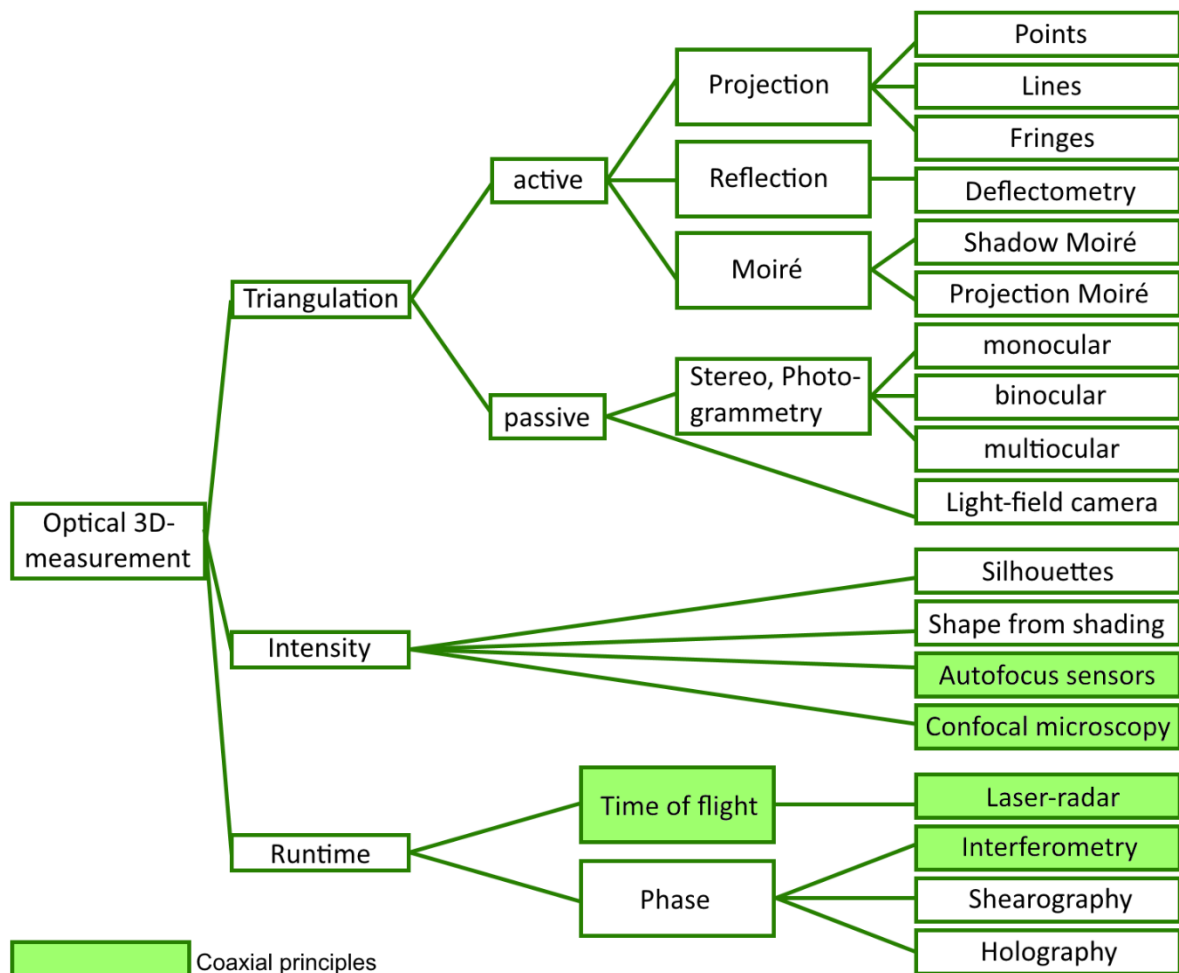


Figure 21: Classification of optical 3D-measurement principles (Beyerer, León, & Frese, 2012, p. 431)

Besides the classification by the measured variable, the inherent angle between the sender, object and the receiver is important. If the angle is zero, then the principle is coaxial. If the angle is different from zero, then the method uses triangulation to calculate the distance. A coaxial method has the advantage that there are no shadows or occlusions and as a consequence the measurement of deep object structures is possible. (Beyerer, León, & Frese, 2012, p. 430)

4.2.1.1 Optical methods based on triangulation

Triangulation is used to measure distances and is based on the geometry of flat triangles. By fixing two angles and one length of a triangle, it is unambiguously defined and the triangulation can either be performed actively or passively. Passive triangulation was first found by Tales von Milet in the 6th century and mostly used to perform measurement tasks of landscapes and to navigate. (Berndt & Christian, 2014)

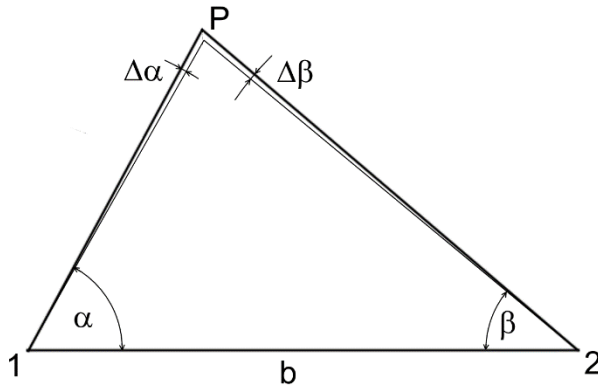


Figure 22: Triangulation principle: With the fixed angles α and β and the base b , the distance to the object point P can be calculated.

In case of the simplified two-dimensional case, the distance to a certain object point P is measured by aiming at it from at least two different positions 1 and 2 which provide two different angles α and β with an accuracy of $\Delta\alpha$ and $\Delta\beta$ respectively as displayed in Figure 22. By knowing the distance b , also called base, between these two positions, the other two sides and the third angle can be calculated. In practice and 3D, the two lines between P and 1 and P and 2 do not always intersect at the same point which leads to inaccuracies in the calculation. The problem then is to find a P' which optimally fits the measured point P . Textures, corners, edges or artificial markers can be used as targeted object points. Active triangulation is

performed by projecting patterns, points or lines onto the object with some sort of pattern projection unit, whose position can also be used as one element of the triangulation. At the intersection of the lines of sight of two or more cameras, or at the intersection of a camera's line of sight and a projector's line of projection, the object point can be calculated. The components which are used as the base of the triangulation need to be calibrated so that the position in the global coordinate systems and the position relative to each other is known. (Gühring, 2002)

The distance between the points 1 and P can then be calculated from the law of sines as

$$\overline{1P} = b \frac{\sin \beta}{\sin(\alpha + \beta)} \quad (4.1)$$

4.2.1.1.1 Measurement uncertainty of triangulation

The uncertainty of the measurement is usually specified as the standard deviation of the measured value. In regard to the triangulation principle, there are two types of uncertainty. The lateral measurement uncertainty parallel to the surface of the object and the vertical measurement uncertainty perpendicular to the surface of the object. For methods which make use of the triangulation principle, the uncertainty is determined by several factors which are listed below:

- a. Quality of the pattern projection
- b. Quality of the camera optics
- c. Sensor resolution
- d. Speckle³ caused by the coherent light

The uncertainty factors (a.) and (b.) can be reduced to a manageable level by using optics which correct most of the optical aberrations. The sensor resolution (c.) can be increased to a suitable level. The speckle (d.) is a stochastic source of error which is caused by coherent light which is incident on a rough surface. Since basically all active triangulation principles are based on measuring the position of a projected pattern, the uncertainty of the measurement increases with the speckle effect. Using white incoherent light instead of a laser decreases the speckle effect. (Beyerer, León, & Frese, 2012, pp. 310-313)

³ Speckle are caused by the interference of light waves which are reflected by a surface with a roughness bigger or equal to the wavelength. They can be observed as a random variation of the intensity.

For a certain triangulation setup the relation between the measured image coordinate x and the searched distance to the object point z can be derived from Figure 23.

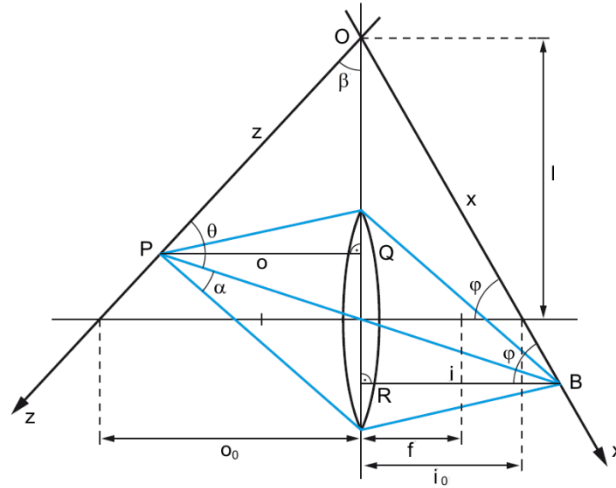


Figure 23: Triangulation setup: The object point P is imaged by the lens onto point B of the detector. The Scheimpflug principle is employed as the planes of the object, the lens and the detector intersect each other in one straight line. (Beyerer, León, & Frese, 2012, p. 306)

In the triangle ORB the image distance i is calculated with

$$i = x \cdot \cos \varphi \quad (4.2)$$

and the respective object distance o is calculated with

$$o = \frac{if}{i-f} = \frac{fxcos \varphi}{xcos \varphi - f} \quad (4.3)$$

From the triangle OPQ the distance z to the measured object point P can be calculated with

$$z = \frac{o}{\sin \beta} = \frac{fxcos \varphi}{(xcos \varphi - f) \sin \beta} \quad (4.4)$$

Since the setup in Figure 23 employs the Scheimpflug principle, the angle φ is fixed. This principle states that the planes of the detector, the object and the lens intersect in a straight line. With the object distance o_0 and image distance i_0 on the optical axis of the lens yields

$$\tan \beta = \frac{o_0}{l} \quad (4.5)$$

$$\tan \varphi = \frac{l}{i_0} \quad (4.6)$$

The formula for thin lenses is

$$\frac{1}{i_0} + \frac{1}{o_0} = \frac{1}{f} \quad (4.7)$$

which yields with (4.5) and (4.6) to

$$\tan \varphi = l \left(\frac{1}{f} - \frac{1}{o_0} \right) = \frac{l}{f} - \frac{1}{\tan \beta} \quad (4.8)$$

$$\cos \varphi = \frac{1}{\sqrt{1 + \left(\frac{l}{f} - \frac{1}{\tan \beta} \right)^2}} \quad (4.9)$$

and consequently with (4.4) to

$$z = \frac{fx}{\left(x-f \sqrt{1 + \left(\frac{l}{f} - \frac{1}{\tan \beta} \right)^2} \right) \sin \beta} \quad (4.10)$$

The relation between x and z is non-linear which is due to the tilted lens. The sensitivity of the measurement is therefore not constant for the whole measurement area and increases with the triangulation angle θ . (Beyerer, León, & Frese, 2012, pp. 310-313)

The minimal vertical measurement uncertainty δ_z can be calculated as

$$\delta_z = \frac{\lambda}{2\pi \sin \alpha \sin \theta} \quad (4.11)$$

and the measuring range Δz is given by

$$\Delta z = \frac{2\lambda}{\sin^2 \alpha} \quad (4.12)$$

with λ being the wavelength of the incident light, α the half aperture angle and θ the triangulation angle in Figure 23.

4.2.1.1.2 Stereo photogrammetry

Photogrammetry uses triangulation to measure the distance to an object point. It is an easy-to-apply and widespread method because only two cameras with known relative distance b are required. The cameras need to be calibrated with a reference object of known dimensions first which leads to the relative position and orientation of the cameras to the measured object. (Berndt & Christian, 2014, p. 14)

For each object point a mathematical relation in a triangle is found in both cameras. Figure 24 shows the principle of a stereo photogrammetry measurement, where b is the distance between the two cameras, d_i is the image distance of both cameras, h_{i1} and h_{i2} are the image sizes, h_o is the object size and d_o is the object distance.

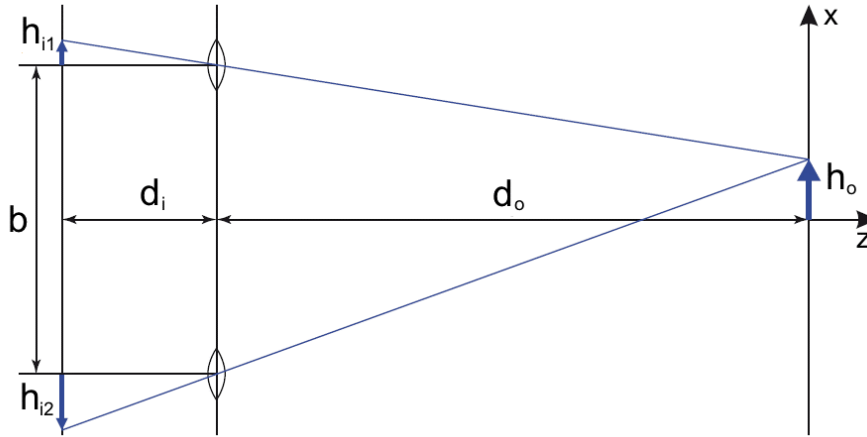


Figure 24: Principle of stereo photogrammetry using two parallel cameras (Beyerer, León, & Frese, 2012, p. 342)

From the similarity of the triangles, it follows that

$$\frac{h_{i1}}{d_i} = \frac{\frac{b}{2} - h_o}{d_o}, \quad (4.13)$$

$$\frac{-h_{i2}}{d_i} = \frac{\frac{b}{2} + h_o}{d_o}. \quad (4.14)$$

Summing (4.13) and (4.14) leads to

$$d_o = \frac{b \cdot d_i}{h_{i1} - h_{i2}}. \quad (4.15)$$

The object distance is inversely proportional to the difference of the image sizes. If the cameras are not aligned parallel to each other as in Figure 24, the information of the relative location of the cameras needs to be obtained with a calibration process. This is the so-called reconstruction problem which is the determination of the three-dimensional position of an object point with known image coordinates. This leads to a linear system of equations in which the camera parameters are inserted. The second aspect of stereo photogrammetry is the correspondence problem which refers to the challenge of identifying identical object features in several images and correlating them to each other. If the correspondence is found and the cameras are calibrated, triangulation is possible. Most of the measurement systems differ only in the way on how they solve the correspondence problem. An object point x_w and its two image points x_1 and x_2 are in one plane E which is defined by x_w and the two optical projection centers P_1 and P_2 as illustrated in Figure 25. (Beyerer, León, & Frese, 2012, pp. 341-346)

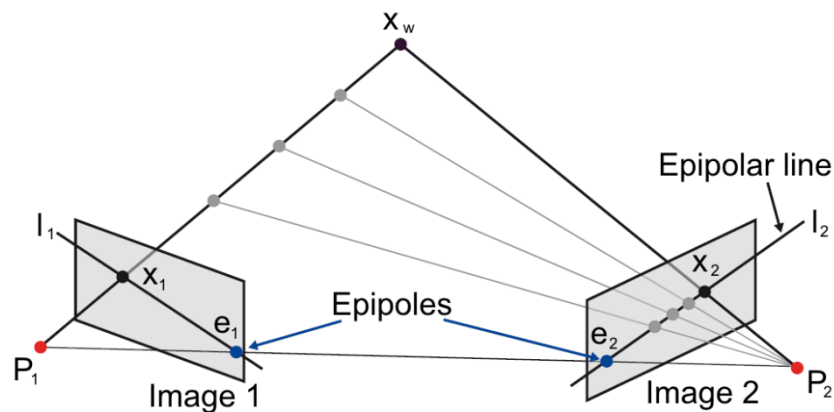


Figure 25: Epipolar geometry: Illustrated are the two image planes which display the object point x_w . Due to the epipolar geometry, the search area for x_2 is reduced to one epipolar line l_2 . By finding the corresponding point x_2 in image 2 to the point x_1 in image 1, the correspondence problem is solved. (Beyerer, León, & Frese, 2012, p. 343)

The epipolar plane intersects the two image planes in the epipolar lines l_1 and l_2 . The corresponding image point x_2 has to be somewhere on l_2 which reduces the search area to one line. The epipolar geometry can also exist between a camera and a projection unit. Depending on the position and the orientation of the cameras relative to each other, the epipolar lines run across the image which makes the calculation difficult. Consequently, the known position and orientation of the cameras are used to transform the two images onto one virtual plane where image lines and epipolar lines coincide. This simplifies the comparison even further because only the pixels of two image lines need to be compared. (Berndt & Christian, 2014)

Due to disturbances and limited resolution, the corresponding sight paths do not always exactly intersect each other. In such a case, the real object point x_w needs to be estimated as the point which has the shortest distance to both sight paths. Although the correspondence problem is reduced to a one-dimensional search by the epipolar geometry, the solution is not that easy to find. Correspondence is made difficult by the fact that the same object looks different to both cameras. On the one hand, this is caused by the different perspectives because shapes and dimensions of the object change with the camera position. Furthermore, certain areas can be occluded for one of the cameras. On the other hand, the measured intensities only match if the object has a diffusely reflecting surface. If however the surface is almost a perfect mirror, the stereo cameras may capture such different images that a correspondence is not possible at all. In addition, differences in the imaging optics and the camera sensors need to be avoided or, if that is not possible, considered via calibration. (Beyerer, León, & Frese, 2012, pp. 346-347)

Ambiguity is another challenge for stereo photogrammetry. The quality of the solution very much depends on the observed scene. If the scene has periodic, little or no structures along the epipolar lines, a defect-free correspondence is not possible. To manage the ambiguity, image smoothing algorithms are used, which however reduce the lateral resolution significantly. (Berndt & Christian, 2014)

Many algorithms which are very different in the quality of the results, the complexity of the measurement and the required computing power, have been developed for the stereo correspondence problem. Examples are correlation methods, dynamic programming, minimization of energy functions or diffusion principles based on differential equations, to only name a few. A detailed overview is given by Scharstein and Szeliski. (Scharstein & Szeliski, 2001)

An alternative to a full reconstruction of surfaces are the feature based stereo correspondence methods which only identify and localize characteristic image details, such as edges, corners, etc. Also a combination of a feature based and full correspondence algorithm is possible. By using more than two cameras, the analysis of the correspondence and the reconstruction can be improved. This reduces the ambiguity for the correspondence problem and occluded areas are reduced. In principle, it does not matter if one static scene is captured by multiple cameras or if one variable camera captures the scene from multiple positions. The extrinsic camera parameters have to be estimated, since a certain motion cannot be reproduced exactly. (Beyerer, León, & Frese, 2012, pp. 347-349)

4.2.1.1.3 Laser triangulation (point-by-point scanner)

Laser triangulation is a point-by-point scanning method which uses the location and angles between the light source and the photo sensing device to calculate the position of an object point. The base b and angle α are known from the setup shown in Figure 22 and the angle β is measured. By using geometric triangulation, the position of a surface point relative to a reference plane can be calculated. Various different high-energy light sources can be used, but lasers are the most common ones. A laser is focused onto the measured object and a photosensitive device, usually a video camera, senses the diffuse reflection of the laser light by the object. Since the diffuse reflections are of interest, the object must not be a perfect mirror, nor a perfect absorber. Otherwise laser triangulation is not possible. Transparent and semi-transparent objects increase the uncertainty of the measurement and the steepness of the surface needs to be within certain limits to avoid occlusions. However, with an increasing angle between the laser beam and surface, the triangulation becomes more sensitive to height differences. This is due to the fact that with an increase triangulation angle a larger distance on the detector is covered for the same height difference. (Beyerer, León, & Frese, 2012, pp. 303-308)

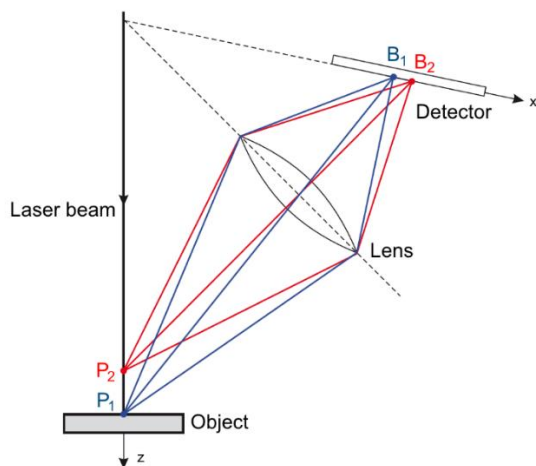


Figure 26: Point-by-point laser triangulation: the Scheimpflug principle is employed. (Beyerer, León, & Frese, 2012, p. 304)

The basic setup of a laser triangulation measurement is shown in Figure 26. Different to a normal camera, where the planes of the camera chip, the objective and the focus are parallel to each other, the laser triangulation method makes use of the Scheimpflug principle. If one object point P_1 is focused on the detector, all the other object points along the laser beam are also in focus, independent of the distance. The accuracy of a measurement is determined by the resolution of the detector and the distance between the surface and the setup. Laser triangulation can acquire data at very fast rates, but since it is a point-by-point scanning method, it takes some time to measure and reconstruct the whole surface of an object. (Beyerer, León, & Frese, 2012, p. 159)

4.2.1.1.4 Light section measurement (line scanner)

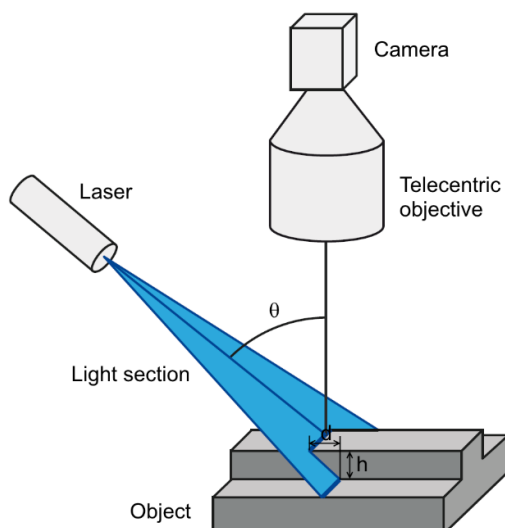


Figure 27: Light section measurement: Height information h is obtained by the lateral displacement d of the detected light section and the angle θ . (Beyerer, León, & Frese, 2012, p. 309)

Light section systems are also based on the principle of triangulation and are a widely used method to acquire the shape of an object. A laser source and optics are used to generate and project a line onto the surface of an object. The projection of the laser line is deformed by the object depending on its height and a camera captures the scattered light. The length of the laser line depends on the fan angle of the lens. The measurement of fine structures depends on the orientation of the light section sensor. Laser light ideally has a Gaussian beam which means that its width increases from the middle to the outside. The smaller the beam is in the middle, the wider the gets towards the outside. (Trostmann & Dunker, 2014)

Similar to the point-by-point laser triangulation, the planes of the laser line, the optics and the camera ideally employ the Scheimpflug principle, so that all points on the line are in focus. In reality this is not always ensured because the optics need to be tilted which is rather expensive. Figure 27 shows the setup of a light section measurement. (Beyerer, León, & Frese, 2012, pp. 308-309)

The height information is obtained for each image section which provides the profile of the surface. By moving the object perpendicularly to the direction of observation, for example with a belt conveyor, the whole surface is measured. The accuracy is determined by the detection of the middle of the laser line. The intensity of the laser as well as the integration time of the image sensor is set automatically to assure that the line is visible in the image. The measurement speed is limited by the necessary integration time which increases if the fraction of the diffusely reflected light decreases. Since the accuracy of the measurement is not constant over the whole measurement area, the uncertainty of the measurement increases with the measurement distance. The accuracy of the measurement depends on several factors such as the triangulation angle and the properties of the measured surface which might cause speckle. Also surfaces with a lot of rills or highly reflecting surfaces can cause significant errors in the measurement. For larger measurement distances, the mechanical stability of the setup is critical, since deformations by forces, vibrations or temperature can cause disturbances. (Trostmann & Dunker, 2014)

The height information can be obtained by the lateral displacement of the detected light section and the triangulation angle as

$$h = \frac{d}{\tan \theta} \quad (4.16)$$

Dimensions and working distance of a light section sensor depend on the necessary triangulation angle and the resulting minimal distance between image sensor and laser source. With an increasing triangulation angle the resolution also increases, but it is limited by the width of the laser line and the decreasing portion of the diffusely reflected light by the surface. As a consequence, triangulation angles between 10° and 25° are used. (Trostmann & Dunker, 2014)

Light section measurements are very accurate and have a high resolution. One major drawback of using the laser technology are possible injuries, especially to the eyes of a worker which can occur because of the high intensity of laser light. Thus, extensive precautions have to be taken which also significantly increase the costs and dimensions of a measurement setup.

4.2.1.1.5 Structured light (areal scanner)

For the acquisition of arbitrary formed objects with complex surfaces, the measuring of discrete points is not practical because it is usually very time-consuming and some areas of the surface may not be reachable. Furthermore, when using a laser grid instead of a single line, the unique identification of a certain line is challenging since the grid is monochromatic and every line looks the same to the camera. For that reason, the use of an areal scanner, such as a structured light projection system, is preferable. Either several lines are projected onto the surface of the measured object which also provides the challenge of uniquely identifying the different lines, or alternatively the use of inhomogeneous patterns is possible. The reflected light beams need to be uniquely identifiable to assure that the triangle is unambiguously defined and triangulation can be performed. The patterns can either be generated with a laser and special optics or with a computer controlled video projector. (Luhmann, 2014, p. 10)

For the structured light illumination, the Scheimpflug principle cannot be fulfilled for the whole surface of the object, but only for one plane which is chosen to be the average object distance. The measurement area and resolution are therefore limited by the depth of sharpness. To capture the surface of an object $z(x, y)$, an inhomogeneous light pattern $b(x, y)$, very often a sequence of fringe patterns, is projected onto the surface of the object. The pattern is distorted by the geometry of the object and the scene is captured by one or more cameras. This requires a synchronized projection of patterns and image acquisition. By analyzing the distorted pattern with one of the fringe analyzing techniques, such as Fourier transform methods, phase stepping and spatial phase detection methods, a wrapped phase map is usually generated. By using a suitable phase unwrapping algorithm a continuous phase distribution is obtained which is proportional to the object's height variations. By calibration of the system for mapping the unwrapped phase distribution to the real world 3D-coordinate system, the surface of the object can be reconstructed. Since only the geometrical movement and the distortions of the pattern and not its intensity are evaluated, the result of the measurement is almost independent of the optical properties of the surface, such as color, reflectivity or distortion behavior. It is only important that a sufficient part of the light is scattered, or in other words, the object must not reflect or absorb the light completely. The accuracy of such systems also depends on the number of different patterns which are used. When performing the triangulation principle with areal patterns, the problem of ambiguity between image pixels and pixels of the projected pattern occur. The unique identification of an object point can be performed with coded sequences which provide an unambiguous code word for every pixel. (Beyerer, León, & Frese, 2012)

A flow chart of a typical structured light projection measurement is shown in Figure 28:

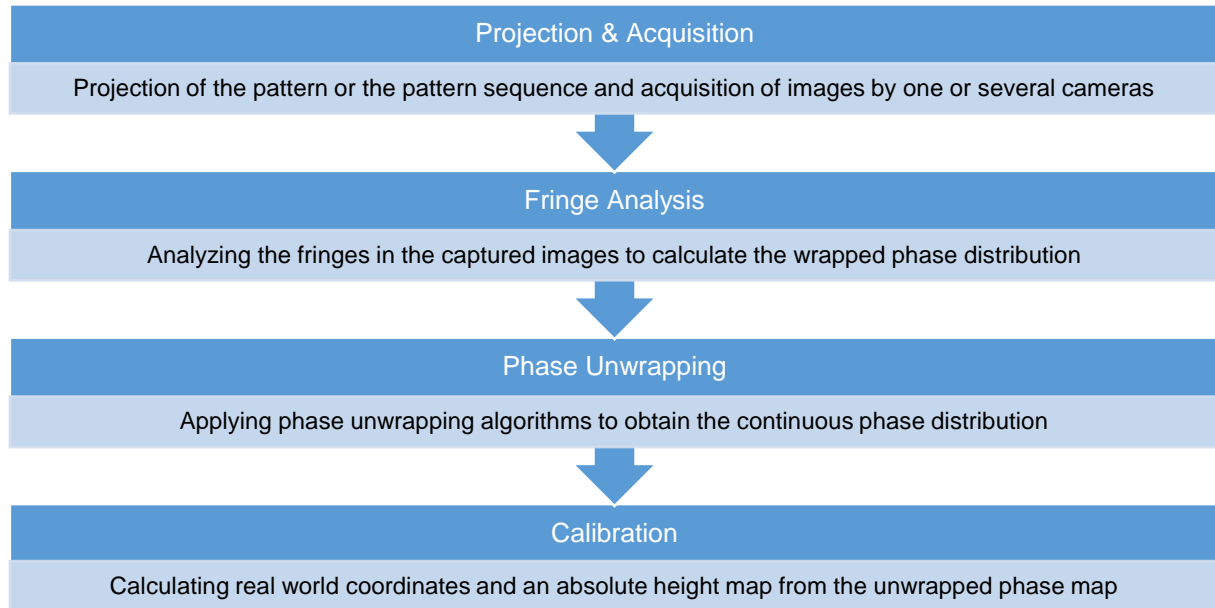


Figure 28: Flow chart of a typical fringe projection process (Gorthi & Rastogi, 2010)

The measurement process with structured light methods has several steps and in each step there exist various variants. These techniques are classified mainly depending on the type of fringe analysis method that is used. A summary of the variety of possibilities for each step is given by Gorthi and Rastogi. (Gorthi & Rastogi, 2010)

There are two basic approaches for a structured light projection system. Methods which use one camera and one projection unit, or methods which use two or more cameras and a projector. For the former methods, the projector is one point of the triangulation and the calibration of the camera and the projector is required. For the latter methods, the projector only provides the desired illumination structure and is not a point of the triangulation, so, only the cameras need to be calibrated. Both approaches use a pattern coding technique. (Bräuer-Burchardt, et al., 2012)

Different pattern coding techniques were reviewed by Salvi (Salvi, Pagès, & Batlle, 2004) and a recent classification was carried out in the dissertation of Navarro Fernández (Navarro Fernández, 2012). Navarro reviewed different structured light methods and analyzed the advantages and disadvantages of each method. The first differentiation is if the method leads to a sparse or a dense reconstruction of the measured object. A sparse reconstruction method assigns the same code word to a region of similar pixels which are neighbored. The size of that region determines the accuracy of the method. A dense reconstruction method uses either a sequence of patterns, which are superimposed over time, or a smooth profile pattern to calculate the surface. For dense methods, every pixel receives a unique code word. The second criteria of the classification is the coding strategy, which can either be time-multiplexing, spatial neighborhood or direct coding. The methods were then analyzed by the features which are listed below.

- Number of projected patterns. This determines whether the method can be used for a moving scene.
- Number of cameras which are used for the reconstruction.
- Axis encoding. This depends on how many axis are encoded.
- Pixel depth. It refers to the color and brightness of the projected pattern. Binary (B), grayscale (G) or color (C) are the three possibilities.
- Coding strategy. This refers to the periodicity of the projected patterns. Can either be absolute (A) or periodic (P).
- Sub-pixel accuracy. It describes whether the features are found with sub-pixel precision which provides a more accurate reconstruction of the surface.
- Color. This shows if the method can deal with colored objects or not.

The classification for a sparse reconstruction is displayed in Figure 31 which is subdivided into a spatial-multiplexing and a time-multiplexing group (Navarro Fernández, 2012). The spatial-multiplexing group includes all methods for which the code word of an object point is generated by its pixel value as well as from the values of the surrounding pixels. The variation of the color or of the intensity are used to create the code word. Spatial-multiplexing only needs one or a few patterns to create the code word, which makes it suitable for moving scenes. However, the resolution is usually lower than the one of methods based on time-multiplexing encoding. The three coding strategies of the spatial-multiplexing group are De Bruijn patterns, non-formal coding and M-arrays. The non-formal coding strategies usually use a brute-force algorithm to generate the code words. Different visual features are used to identify every neighborhood. De Bruijn method uses a striped or multi-slit color pattern for encoding and the position in the image is determined by the color of the stripe (or slit) and the surrounding stripes. Multi-slit patterns are more accurate than striped patterns, however, usually yield a lower resolution. A De Bruijn sequence of rank n on an alphabet of size k is a cyclic word in which each of the k^n words of length n appears exactly once. (Pagès, Salvi, García, & Matabosch, 2003)

A simple example of a De Bruijn circle with $n = 3$ and $k = 2$ is shown in Figure 29 (a).

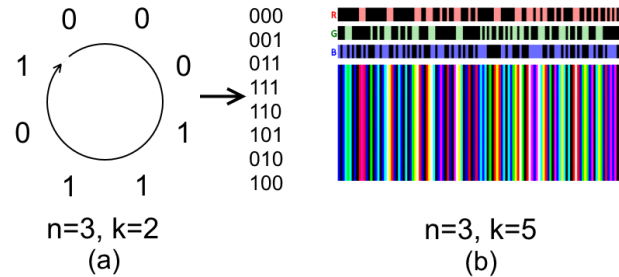


Figure 29: De Bruijn circle (a) and De Bruijn pattern (b) (Geng, 2011)

When going around the circle, there is no repeated three-digit pattern in the sequence. This feature can be used to create a stripe pattern sequence that does not repeat itself. This unambiguity makes the decoding step possible. An example of a De Bruijn pattern with $n = 3$ (R, G, B) and $k = 5$ (5-bit) containing 125 stripes is shown in Figure 29 (b). Neighboring stripes of a De Bruijn pattern must have different colors, otherwise stripes with a larger width occur, which confuses the 3D-reconstruction algorithms. (Geng, 2011)

M-arrays (perfect maps) take advantage of coding both axis to include a higher degree of redundancy. The coding is done with a certain alphabet of symbols or colored dots in a grid. The basic concept is to label every sub-window in the projected pattern so that the pattern in any sub-window is unique and fully identifiable. Figure 30 (a) shows a pseudo-random binary array (PRBA) pattern whose grid intersections are marked by dots. PRBA patterns are defined by an n_1 by n_2 array encoded with a pseudo-random sequence so that any k_1 by k_2 sub-window has fully defined absolute coordinates within the array. (Salvi, Pagès, & Batlle, 2004)

The PRBA sequence uses the primitive polynomial modulo 2^n method which states

$$2^n - 1 = 2^{k_1 k_2} - 1, \quad n_1 = 2^{k_1} - 1, \quad n_2 = \frac{2^n - 1}{n_1}. \quad (4.17)$$

Instead of using a PRBA, a multivalued pseudo-random array can be used and converted into a projection pattern with unique sub-windows. Mini-patterns are assigned to each value and form a special code word as shown in Figure 30 (b). Another method of generating a pseudo-random array is by filling the pattern with random code words consisting of colored dots. By filling the full pattern step-wise and

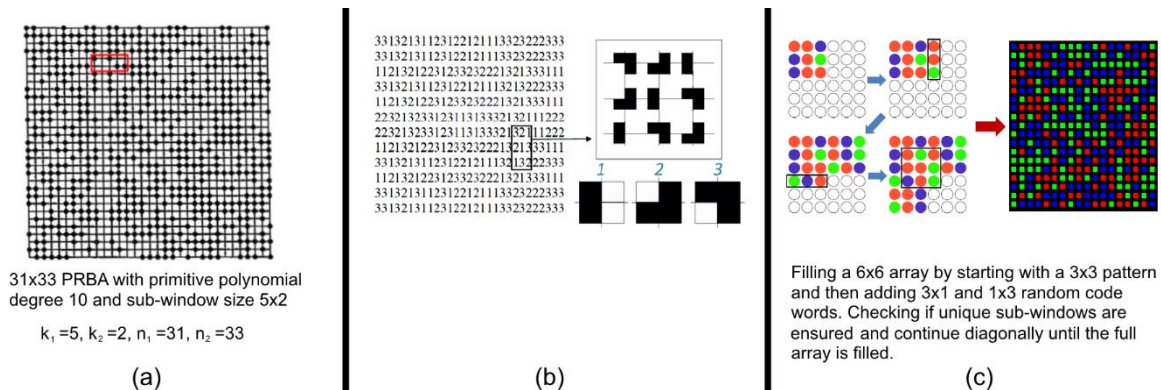


Figure 30: Different M-arrays: (a) Pseudo-random binary array (Geng, 2011), (b) Multivalued pseudo-random array, (c) Color-coded pseudo-random array (Salvi, Pagès, & Batlle, 2004)

checking the uniqueness of each sub-window while doing so, a pattern as displayed in Figure 30 (c) is formed. There are also many other possibilities to improve specific aspects of 3D-surface reconstruction systems by combing several of the strategies explained above. (Geng, 2011)

The time-multiplexing group is based on creating the code word by projecting a sequence of patterns onto the object and consequently the code word is only complete if all patterns are projected. This property usually limits the time-multiplexing methods to static objects. To make time-multiplexing methods suitable for moving objects, either the length of the sequence needs to be reduced or high-speed projection and acquisition need to be used. Time-multiplexing methods are easy to implement and achieve a very high resolution and accuracy. Usually, the first projected pattern corresponds to the most significant bit, following a coarse-to-fine gradation. The accuracy of these methods directly depends on the number of projected patterns as every pattern provides a finer resolution. Additionally, time-multiplexing methods are rather robust to noise because the code word basis is small. Several time-multiplexing methods are developed such as binary codes, n-ary codes and temporal hybrid codes. N-ary codes have a bigger alphabet than binary codes, which effectively reduces the number of projected patterns. Moreover, the distance between pixels with the same code word is reduced. Hybrid methods combine spatial and temporal information. (Navarro Fernández, 2012)

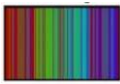
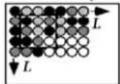
| | | Author | Year | Patterns | Cameras | Axis | Pixel depth | Coding strategy | Subpixel acc. | Color | | |
|--|----------------------|---|--|----------|---------|------|-------------|-----------------|---------------|-------|-----|-----|
| S P A R S E | Spatial Multiplexing |  De Bruijn | Boyer | 1987 | 1 | 1 | 1 | C | A | Yes | No | |
| | | | Salvi | 1998 | 1 | 1 | 1 | 1 | C | A | Yes | Yes |
| | | | Monks | 1992 | 1 | 1 | 1 | 1 | C | A | Yes | No |
| | | | Pages | 2004 | 1 | 1 | 1 | 1 | C | A | Yes | No |
| | | Non formal | Forster | 2007 | 1 | 1 | 1 | 1 | C | A | Yes | No |
| | | | Fechteler | 2008 | 1 | 1 | 1 | 1 | C | A | Yes | No |
| | | | Tehrani | 2008 | 1 | 2 | 1 | 1 | C | A | No | Yes |
| | | | Maruyama | 1993 | 1 | 1 | 2 | 2 | B | A | No | Yes |
| | | | Kawasaki | 2008 | 1 | 1 | 2 | 2 | C | A | No | Yes |
| | | | Ito | 1995 | 1 | 1 | 2 | 2 | G | A | No | Yes |
| | | M-Array |  M-Array | Griffin | 1992 | 1 | 1 | 2 | C | A | Yes | Yes |
| | | | | Morano | 1998 | 1 | 1 | 2 | C | A | Yes | Yes |
| | | | | Pages | 2006 | 1 | 1 | 2 | C | A | Yes | No |
| | Albitar | | | 2007 | 1 | 1 | 2 | B | A | No | Yes | |
| | Time Multiplexing |  Binary codes | Posdamer | 1982 | >2 | 1 | 1 | B | A | No | Yes | |
| | | | Ishii | 2007 | >2 | 1 | 1 | B | A | No | Yes | |
| Sun | | | 2006 | >2 | 2 | 1 | B | A | Yes | Yes | | |
| N-ary codes | | Caspi | 1998 | >2 | 1 | 1 | C | A | No | No | | |
| Shifting codes | | Zhang | 2002 | >2 | 1 | 1 | C | A | Yes | No | | |
| | | Sansoni | 2000 | >2 | 1 | 1 | G | A | Yes | Yes | | |
| | | Gühring | 2001 | >2 | 1 | 1 | G | A | Yes | Yes | | |

Figure 31: Pattern classification for sparse reconstruction methods (Navarro Fernández, 2012)

For a dense reconstruction of an object, the depth of a point is determined by its gray or color value with respect to the projected pattern. The classification for dense reconstruction methods by Navarro is shown in Figure 32. There are some time-multiplexing methods which can be used, such as discrete or continuous phase shifting, which includes single and multiple phase shifting. Phase shifting additionally includes the phase information to determine the depth of a point. Another group uses frequency-multiplexing, here phase decoding is performed by analyzing the frequency of the image. The last group for a dense reconstruction is the spatial-multiplexing group and especially the grading methods. These methods refer to all the techniques containing the entire code word for a given object point in its pixel value. (Navarro Fernández, 2012)

Navarro then also performed a series of experiments to evaluate the performance of some of the coding strategies and he comes to the conclusion that the time-multiplexing shifting approaches deliver the best results. However, the necessary number of projected patterns to reconstruct the surface limits these

methods to static scenes and the non-linearity of the camera, which produces leakage from white to black fringes, and makes the techniques susceptible to noise, which increases the uncertainty of the measurement. Among the one-shot techniques, De Bruijn patterns have the highest accuracy.

| | | | Author | Year | Patterns | Cameras | Axis | Pixel depth | Coding strategy | Subpixel acc. | Color |
|----------------------|--|--|------------|------|----------|---------|------|-------------|-----------------|---------------|-------|
| DENSE | Time multiplexing | Single phase shifting  | Srinivasan | 1985 | >2 | 1 | 1 | G | P | Yes | Yes |
| | | | Ono | 2004 | >2 | 1 | 1 | G | P | Yes | Yes |
| | | | Wust | 1991 | 1 | 1 | 1 | C | P | Yes | No |
| | | | Guan | 2004 | 1 | 1 | 1 | G | P | Yes | Yes |
| | | Multiple phase shifting  | Gushov | 1991 | >2 | 1 | 1 | G | A | Yes | Yes |
| | | | Pribanic | 2009 | >2 | 1 | 1 | G | A | Yes | Yes |
| | Frequency Multiplexing | Single coding frequency  | Takeda | 1983 | 1 | 1 | 1 | G | P | Yes | Yes |
| | | | Cobelli | 2009 | 1 | 1 | 1 | G | P | Yes | Yes |
| | | | Su | 1990 | 2 | 1 | 1 | G | P | Yes | Yes |
| | | | Hu | 2009 | 2 | 2 | 1 | G | P | Yes | Yes |
| | | | Chen | 2007 | 1 | 1 | 1 | C | P | Yes | No |
| | | | Yue | 2006 | 1 | 1 | 1 | G | P | Yes | Yes |
| | | | Chen | 2005 | 2 | 1 | 1 | G | P | Yes | Yes |
| | | | Berryman | 2008 | 1 | 1 | 1 | G | P | Yes | Yes |
| | | | Gdeisat | 2006 | 1 | 1 | 1 | G | P | Yes | Yes |
| Zhang | | | 2008 | 1 | 1 | 1 | G | P | Yes | Yes | |
| Lin | | | 1995 | 2 | 1 | 1 | G | P | Yes | Yes | |
| Huang | | | 2005 | >2 | 1 | 1 | G | P | Yes | Yes | |
| Jia | | | 2007 | 2 | 1 | 1 | G | P | Yes | Yes | |
| Wu | | | 2006 | 1 | 1 | 1 | G | P | Yes | Yes | |
| Spatial Multiplexing | Grading  | Carrhill | 1985 | 1 | 1 | 1 | G | A | Yes | No | |
| | | Tajima | 1990 | 1 | 1 | 1 | C | A | Yes | No | |

Figure 32: Pattern classification for dense reconstruction methods (Navarro Fernández, 2012)

Time-multiplexing strategies are based on temporal encoding which means that a sequence of patterns is projected onto the measured object. The code word is then formed by the illuminance values for that pixel, one bit for every projected pattern. One example for a time-multiplexing method is using an n-bit binary code which uses either fully bright (logical 1) or fully dark (logical 0) pixels to form the code word. The binary encoding however, has the drawback that the error in the decoding step is dependent on the bit-number where it occurs. As a consequence, the effect of the error on the measurement result differs significantly. If the error, for example, occurs in the highest bit-number, the implied measurement error is 2^{n-1} lines. A more robust encoding is the Gray-code⁴, which is also a binary code. For every bit of the code word an image is projected onto the surface as illustrated in Figure 33. The frequency of the pattern is doubled from one projection to the next. A synchronized camera observes the reflected pattern and captures an image for every projection. The triangulation requires the calculation of the edge between two consecutive stripes, which can be done by projecting a normal and an inverse stripe pattern. Then, by searching for the intersections of both profiles, the stripe edge position can be computed. A binary

⁴ The name Gray refers to the name of the inventor Frank Gray and not to the color.

jumps and eliminate the discontinuity and retrieve the absolute phase information. One possibility is to add or subtract multiples of 2π with

$$\phi(x, y) = \phi'(x, y) + 2k\pi \quad (4.22)$$

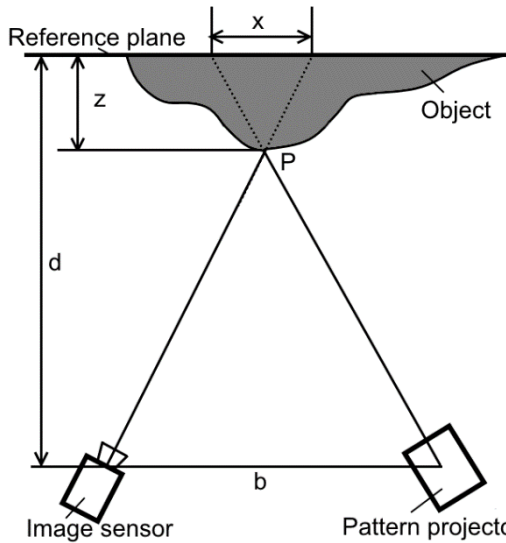


Figure 35: Phase shifting reference plane principle. (Geng, 2011)

Phase unwrapping methods only unwrap the phase relatively and do not solve for the absolute phase. How the 3D-coordinates can be calculated from the difference between the measured phase and the phase from a reference plane for a simple case is shown in Figure 35. (Geng, 2011)

From the similarity of the triangles follows

$$\frac{z}{x} = \frac{d-z}{b} \quad (4.23)$$

which leads to

$$z = \frac{d \cdot x}{b+x} \quad (4.24)$$

and for $x \ll b$ reduces to

$$z \approx \frac{d \cdot x}{b} \propto \frac{d}{b} (\phi - \phi_0) \quad (4.25)$$

A combination of Gray-code and phase shifting is also a widely used method. Patterns based on Gray-code have a unique code for every pixel and no spatial neighborhood information is needed to calculate the surface. Phase shifting methods usually have a higher resolution, however, the drawback is that they cause ambiguity because the unwrapping algorithms do not solve for the absolute phase. This problem is solved by combining the phase shifting method with the Gray-code method. This also combines the advantages of both strategies: The unambiguity and robustness of the Gray-code and the higher resolution of the phase shifting method which leads to a highly accurate 3D-reconstruction. Additionally, the redundancy of the combination of the two methods can be used to detect errors in the Gray-decoding because an incorrect decoding contradicts the results of the phase shifting (Wiora, 2001). A combination of the two methods has however also drawbacks. The first one being the increased measurement time because of the higher number of patterns which requires a very fast projection and acquisition of the pattern sequence to compensate. Furthermore, colorful objects with significant contrast can hardly be reconstructed with the phase shifting method. Also the camera has to have a significantly higher resolution than the projector because it integrates over a certain area and the pixel values are affected by its neighbors. As a result, very often the phase shifting method is substituted by a line shifting method which uses one pattern of binary stripes with a certain width and shifts the pattern as often as the width of the stripes is in pixel to cover the full resolution of the pattern. Since this pattern is also periodic, the Gray-code is necessary to solve the ambiguities that come up. Additionally, two patterns, one fully illuminated and one fully dark, are projected for gray level normalization. (Salvi, Pagès, & Batlle, 2004)

Another approach is to use a so-called Rainbow 3D-Camera which projects one spatially varying wavelength illumination onto the objects surface. The rainbow projector is one point of the triangulation which establishes a correspondence between projection angle, plane of light and particular spectral wavelength. These projected landmarks are easy to identify by a color camera for each object point, and with the known baseline between projector and camera and the respective viewing angle, triangulation can be performed. It is also possible to use various continuously varying color patterns to encode the pixels. They can be obtained by using an intensity variation pattern for each color channel of a projector, such that when they are superimposed, they form a continuously varying color pattern. (Geng, 2011)

The strengths of structured light projection methods is their high accuracy, the flexible configuration and measurement setup with several simultaneously working cameras and the wide variety of suitable algorithms. Additionally, decreasing prices and the constant development of high-speed hardware in regards to resolution and speed are advantages of structured light projection systems. (Berndt, Boochs, & Kühmstedt, 2014)

Fringe projection methods are one of the most active research areas in optical metrology. The use of fringe projection to reconstruct the surface of an object has a wide variety of applications. (Gorthi & Rastogi, 2010)

4.2.1.1.6 Deflectometry

Deflectometry is used to inspect highly reflecting surfaces. The principle is based on looking at the reflection of the surroundings in the surface and searching for local distortions caused by defects. Deflectometry measurement techniques have an extremely high resolution while relying on standard components. A camera captures the reflection of a pattern which is shown on a screen or monitor by the object's surface as shown in Figure 36.

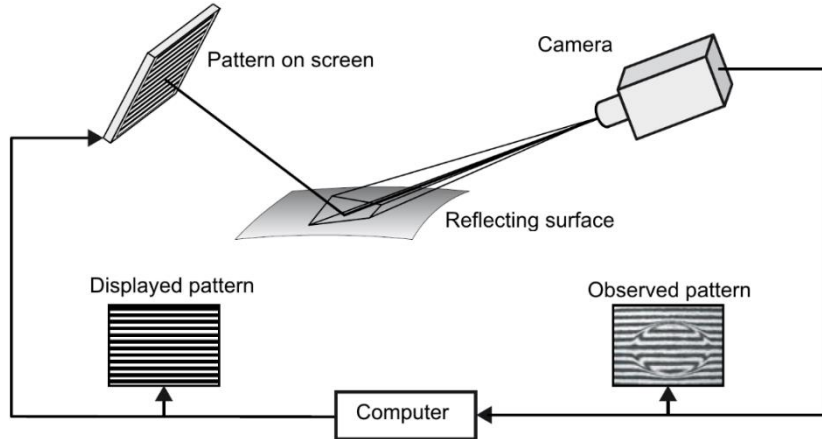


Figure 36: Deflectometry principle: A pattern is displayed on a screen and the reflection on the surface is observed by a camera. A computer then analyzes the distortions caused by surface defects. (Beyerer, León, & Frese, 2012, p. 320)

Due to the reflecting surface, the camera is not focused onto the surface but rather observes the screen directly through the reflection. This requires a highly reflecting surface and therefore deflectometry is not applicable for non-reflecting or diffuse surfaces. (Heizmann & Werling, 2014)

Figure 37 shows the increased sensitivity of deflectometry to the tilt angle of the surface. When the camera is focused onto the surface (a) the camera always captures the same pixels of the projection, regardless of the tilt angle of the surface. If the camera is however focused onto the screen (b), which is the case for deflectometry, the camera shows a different area of the screen when the surface is tilted.

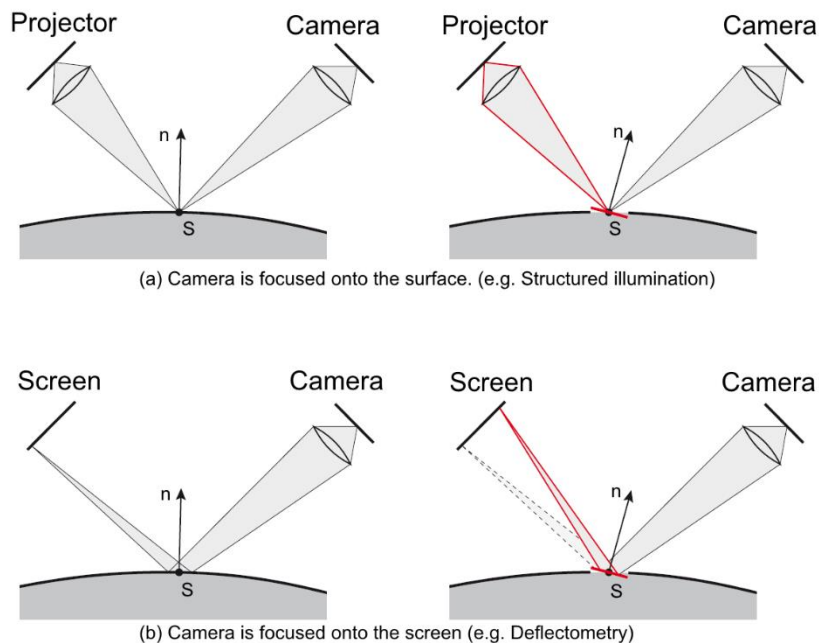


Figure 37: Comparison of the light path of structured light and deflectometry (Beyerer, León, & Frese, 2012, p. 322)

To detect defects, it is often sufficient to take one shot with a suitable pattern. For a full reconstruction of the surface, the pixels of the camera and the screen need to be related to each other. This can be done by using a pattern sequence such as Gray-code, phase shifting, etc. Gray-code usually has a lower resolution, whereas phase shifting is more robust and also allows focusing onto the surface instead of the screen. (Beyerer, León, & Frese, 2012, pp. 320-322)

4.2.1.1.7 Moiré method

The Moiré effect is created by the superposition of two periodic structures which leads to an interference structure with a lower local stripe density than the individual structures. Figure 38 shows how the Moiré effect can be generated. Either by overlaying two patterns with varying gap width between the stripes (a), by rotating one structure relative to the other (b) or by overlaying two patterns with different magnification (c).

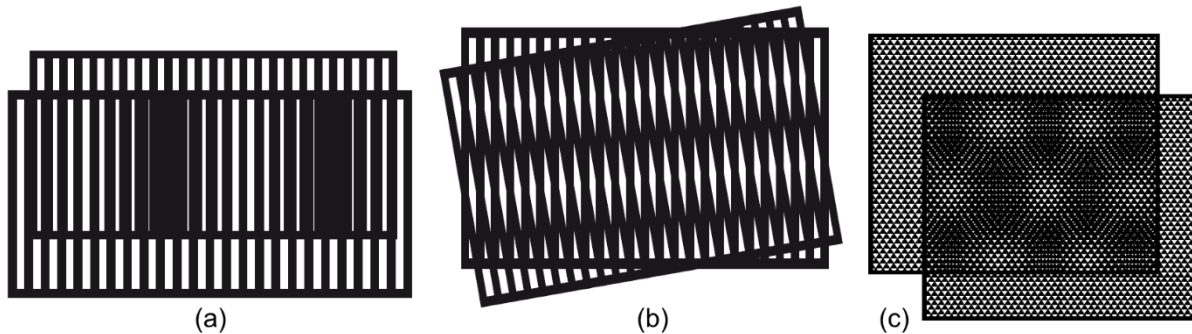
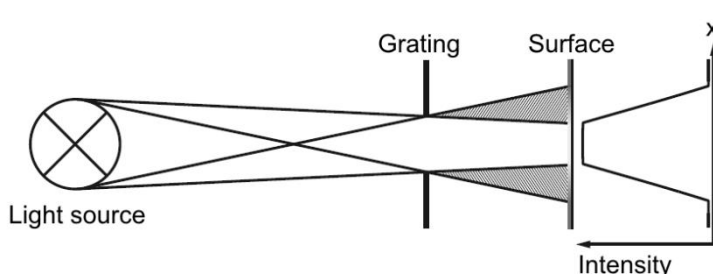


Figure 38: Generation of Moiré patterns by overlaying two patterns with: (a) varying gap width, (b) rotated orientation, (c) different magnification. (Beyerer, León, & Frese, 2012, p. 331)

Applications which make use of the Moiré effect, for example, the measurement of mechanical tensions in stressed components, use a pattern on the surface of an object and observe it with an interference pattern. The interference allows the analysis of the profile and possible defects of the surface. Methods which project a certain light structure onto an object and use a reference pattern to interfere with the observed scene, are called Moiré methods. The Moiré stripes appear with maximal intensity where the transparent areas of both gratings overlap. The local density of these stripes is proportional to the gradient of the profile of the surface. Hence, the stripes form level curves which are however ambiguous. The ambiguity can be resolved by taking and analyzing several shots with different distances to the object. There are two possibilities on how to create the level curves, which is either by analyzing the distorted stripe pattern or by measuring the optical interference with a reference pattern. The latter is usually the faster method as the analysis is done optically. The level curves allow direct interpretation of the scene. (Beyerer, León, & Frese, 2012, pp. 330-338)

Shadow Moiré:

For the Shadow Moiré method a grating is directly placed above the surface of the measured object which is illuminated by a point light source at a certain angle and a camera captures the Moiré pattern. The camera is almost positioned perpendicularly to the surface to avoid distortions. Parallel light is not used because of the dimensions of the necessary lenses and mirrors. Instead a point source at a rather large distance to the surface is used. Only in the deepest shadow the grating shadows the light source completely. When moving towards the center of illumination, areas with half shades occur, where the light source is only partly covered by the grating as displayed in Figure 39. Between the area where the light source is fully visible and the area with the deepest shadow, the intensity of the illumination decreases gradually. This area increases the uncertainty of the measurement.



The measurement is also influenced by the fact that the grating cannot be placed arbitrarily near to the object which causes problems with the shadowing. Furthermore, perspective distortions of the projection and the captured image occur. (Beyerer, León, & Frese, 2012, pp. 338-340)

Figure 39: Shadowing of the light source by a grating (Beyerer, León, & Frese, 2012, p. 339)

Projection Moiré:

For the Projection Moiré method, a grating pattern is projected onto the surface of an object, and a reference grating is mounted in front of the camera or directly on the camera chip which allows the inspection of objects at a larger distance. Because the projector is mounted at a certain angle, perspective distortions of the projection occur. This has an effect when using periodic gratings because the Moiré stripes then do not correlate to the level curves of the surface. This can either be rectified by using special unequally spaced gratings or post processing using a calibration-image. Usually, the profile of the surface cannot be determined unambiguously from the level curves, which then requires several shots of the scene using phase shifted grating structures. (Beyerer, León, & Frese, 2012, p. 340)

4.2.1.1.8 Light field cameras

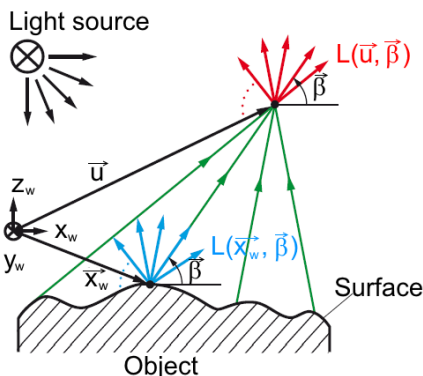


Figure 40: Light field: includes all possible images of the measured object. (Beyerer, León, & Frese, 2012, p. 350)

A light field describes the density of the light beams which are coming from one object point and travel in a certain direction as illustrated in Figure 40. The light field $L(\vec{x}_w, \vec{\beta})$ is then a function in the 5D-space of the point $\vec{x}_w = (x_w, y_w, z_w)^T$ and the direction $\vec{\beta} = (\beta_1, \beta_2)$. If $L(\vec{x}_w, \vec{\beta})$ is known for all points of the objects surface, the induced light field $L(\vec{u}, \vec{\beta})$ in the surrounding space is unambiguously defined. The direction spread of the density of light beams in every point in space is then given. In other words, the light field includes all possible images of the measured object which can be obtained at the given setup of an object and a light source. If it was possible to have the full light field at the disposal, one would be able to calculate images of arbitrary camera positions and parameters. (Beyerer, León, & Frese, 2012, pp. 349-350)

A normal camera captures only one part of the light field in form of a two-dimensional image. The information of where the light beams come from is therefore lost. A light field camera, or plenoptic camera, is able to capture a certain part of the light field on one plane. Figure 41 shows that a light field camera is built up of an objective, a micro lens array with $(N')^2$ lenses and an imaging sensor with N^2 pixels, with the requirement that $N > N'$. (Beyerer, León, & Frese, 2012, p. 351)

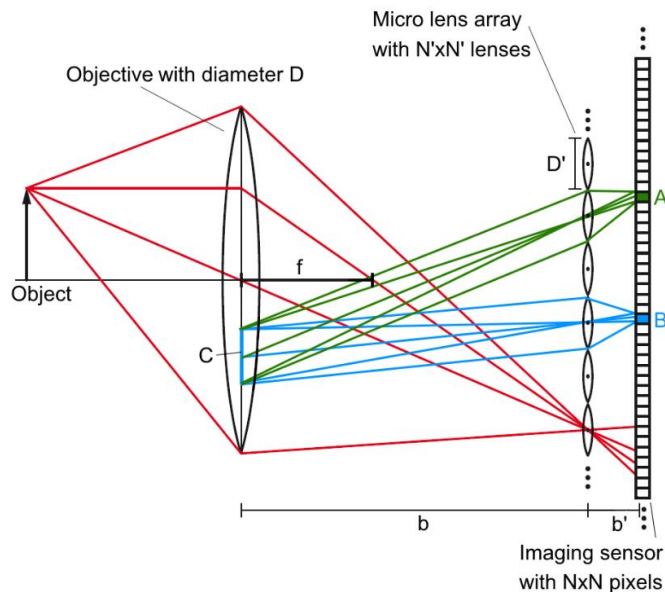


Figure 41: Light field camera principle: A micro lens array focuses different areas of the objective, for example area C, onto the imaging sensor which creates several images from different perspectives. (Beyerer, León, & Frese, 2012, p. 352)

The objective focuses the scene onto the plane of the micro lens array instead of the imaging sensor (normal camera). Every micro lens focuses the plane of the objective onto the imaging sensor, which enables the measurement of the intensity in dependence to the direction the light comes from. The pixel

position behind the micro lens is corresponding to the direction of the incident light and as a result one sector of the light field is captured. The images of the objective and the micro lens array must not overlap nor leave gaps in between to make use of the full resolution, so the requirement

$$\frac{D}{b} = \frac{D'}{b'} \quad (4.26)$$

has to be fulfilled. As shown in Figure 41 the area C is mapped by the micro lens onto the pixel A of the imaging sensor. Only light which passes through the area C reaches that pixel. Pixel A is then assigned to a partly area of the objective. The other micro lenses also map the area C on their respective pixels, as, for example, pixel B. All these pixels capture light which comes from an object point through area C. An image with $(N')^2$ pixels of the area C is generated. Every pixel, which is mapped by the same micro lens as pixel A, shows a different area of the objective. The objective is subdivided into n areas. A light field camera captures n images with $(N')^2$ pixels from different perspectives simultaneously, which can then be analyzed with stereo methods to reconstruct the 3D-shape of the measured object. Additionally, this also makes the placement of virtual cameras with arbitrary synthetic perspectives and the calculation of their images possible. For the calculated synthetic images, the depth of sharpness and the focused area can be altered inside certain limits. The light field camera is especially suited for close field or macro images. (Beyerer, León, & Frese, 2012, pp. 352-355)

4.2.1.2 Optical methods based on intensity

Optical methods based on intensity reconstruct the shape of an object by observing the change of the intensity of the scattered and transmitted light. (Beyerer, León, & Frese, 2012, p. 272)

4.2.1.2.1 Silhouettes capturing

A silhouette of an object is the projection of its structure onto a plane which enables to inspect deviations from a reference as displayed in Figure 42. This method can be used if a full 3D-reconstruction is not needed. When using the bright field method, the camera is directly aiming onto an areal light source with the measured object in between. The object blocks the light from the light source and the shadow and the silhouette can be seen. The dark field method can also be used to capture the silhouette and is used to inspect transparent glass or plastic bottles. For this approach an aperture, which is slightly bigger than the field of view of the camera, is placed in between the object and the light source. The scattered light especially illuminates the edges and corners of the transparent object. (Beyerer, León, & Frese, 2012, pp. 355-358)

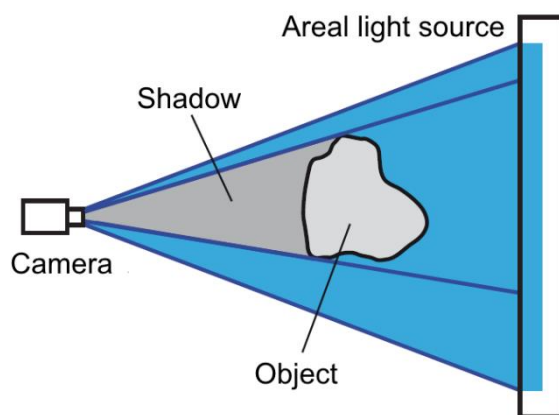


Figure 42: Silhouette capturing method with bright field configuration. (Beyerer, León, & Frese, 2012, p. 356)

4.2.1.2.2 Shape from shading

This method reconstructs, with known illumination parameters, the normal of the surface and by integration the 3D-shape of the object. This is possible due to the relation that the density of beams coming from a surface is dependent on the normal and the direction of the illumination. As a result, a numerical stable solution is difficult to find. Another possibility is to use several images with different illumination, which is called photometric stereo method, which can also employ a color coded sequence. (Beyerer, León, & Frese, 2012, pp. 362-364)

Main field of application is the 3D-reconstruction from satellite images. (Gockel, 2006)

4.2.1.2.3 Autofocusing

Light of a laser diode is guided by movable lenses and a collimator onto the object. The reflected light is split up by a beam splitter and shines onto a detector. The lens is moved so that the image blur on the sensor is minimized. From the correct position of the lens, where the image is focused, the distance can be calculated. Autofocusing is a point-by-point measurement technique and consequently very time-intensive when a full surface needs to be measured. (Beyerer, León, & Frese, 2012, pp. 364-365)

4.2.1.2.4 Confocal microscopy

One property of microscopes is that they have a very narrow depth of sharpness which can be used to perform a 3D-reconstruction of the surface of an object. This property can be used because in the image only structures are identifiable which are very close to the focal plane. All the other structures are blurred significantly and are almost not visible in the image. The distance between measured object and objective lens is systematically varied and a series of images is captured. For each pixel of this series of focused images, the local maximum of a significant feature of the image is determined. The object can then be reconstructed by taking the conditions of the single images into consideration. The focus sequence method is an areal measurement method. For the method of confocal microscopy, the object is additionally illuminated, typically with a laser light source. The pinhole aperture makes sure that only focused light is incident on the object. Figure 43 shows the principle of confocal microscopy. The illumination from a light source (blue path) passes the aperture, the dichroic mirror and a lens focuses the light onto the object. The light is reflected back from the object on the dichroic mirror which deflects it onto a second aperture which makes sure that only focused light (red path) hits the detector. If the point P is not in focus, the reflected light (green path) is blocked by the aperture. (Beyerer, León, & Frese, 2012, pp. 365-370)

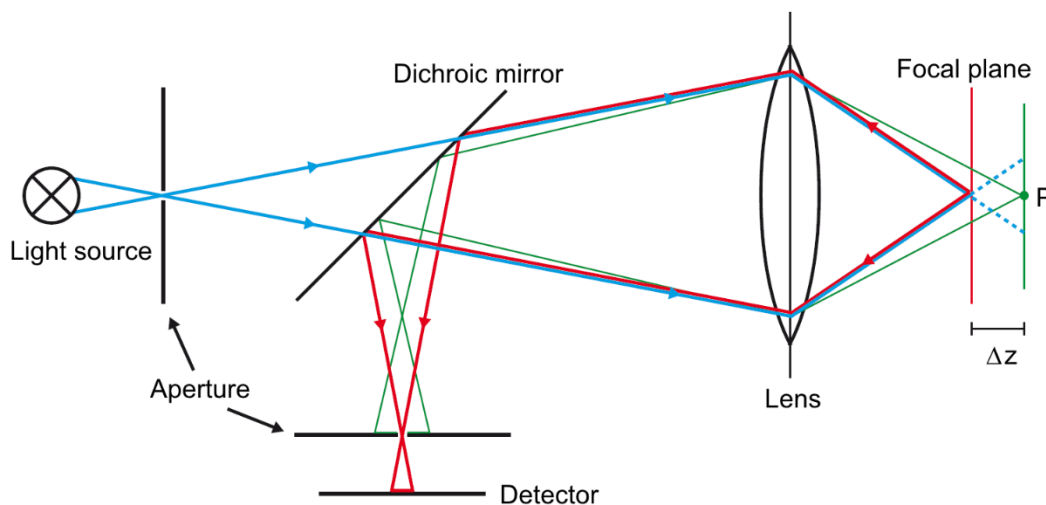


Figure 43: Confocal microscopy principle: Light (blue path) passes through an aperture and a dichroic mirror and is focused onto the object by a lens. The focused reflection by the object (red path) is deflected by the dichroic mirror onto a detector. An aperture blocks reflections by the object which are not focused (green path). (Beyerer, León, & Frese, 2012, p. 367)

The intensity of the illumination at the point P decreases with $(\Delta z)^{-2}$ because the illuminated area increases with $(\Delta z)^2$. This also decreases the intensity of the reflection from the object point P on the aperture of the detector. As a consequence the intensity at the detector decreases approximately with $(\Delta z)^{-4}$. The maximal intensity is present on the focal plane which is found by moving the object along the z-axis and taking a sequence of images. Different to the focus sequence method, confocal microscopy is a point-by-point measuring method. The vertical measurement can be done by either moving the object or the objective. (Beyerer, León, & Frese, 2012, pp. 365-370)

An alternative to analyze the spectrum is to use an objective with a strong chromatic aberration. Since each wavelength has a different focus the search for the distance with maximal intensity is substituted by the search for a certain wavelength. The vertical scan leads to confocal curves for each object point and the maximal intensity shows the location of that point. From the sequence of images not only the 3D-structure is obtained, but also the information about the reflectance of the objects surface. An image where all areas of the object are in focus can be generated by fusion of the single images. (Taphanel, 2014)

The main application of confocal microscopy are the capturing of profiles of technical surfaces and the 3D-microscopy of partly transparent objects in the field of medicine and biology. Confocal microscopes are limited to the measuring of flat surfaces. Furthermore, the measurement speed is rather low, which makes a real time measurement of the full surface impossible. (Hill, 2014)

4.2.1.3 Optical methods based on run time

Run time methods measure the time which is required by the light to cover the distance to the object and back. Alternatively, the phase distortion of the light can be measured by using the interference effect. (Beyerer, León, & Frese, 2012, p. 272)

4.2.1.3.1 Time-of-flight

The time-of-flight method is based on the measurement of the time that a light wave needs to travel to the object and back. Two measurement methods can be used. The first one being a pulse time-of-flight for which the distance d that is covered by the light in the measured time can then be calculated as

$$d = \frac{c}{2} \cdot t \quad (4.27)$$

where c is the speed of light in air. To obtain an accurate measurement of the distance a very precise time measurement is necessary. The accuracy also depends on the laser pulse power, shape and frequency. A point sensor typically uses a pulsed laser beam as a light source which requires the synchronization of the time measurement with the pulse of the laser. Also a certain delay time needs to expire to make sure that no echo signal is on its way back. Pulse time-of-flight systems usually operate at distances of several meters to kilometers for which a resolution in the area of centimeters is sufficient. In this category the so-called LIDAR-sensors (Laser Illuminated Detection And Ranging) can be found which use a laser to scan a two-dimensional cross-section of the object room. The scan motion is performed with a rotating mirror which makes the sensor fast on one axis, but rather slow on the second axis. When dealing with dynamic scenes distortions occur, since the measurement of the object points does not happen simultaneously. LIDAR-sensors are usually used for orientation in the field of robotics or driving assistance systems, for atmospheric research and meteorology, for the measurement of whole buildings and industrial plants, or the documentation of cultural heritage. (Beyerer, León, & Frese, 2012, pp. 370-371)

Alternatively, a code sequence can be modulated for the light and instead of measuring the time directly, the phase shift between the sent and received signal is analyzed. Within half of the wavelength of the modulation frequency, the phase shift is unique and proportional to the distance of the reflecting point. For these phase time-of-flight systems the distance d can then be calculated as

$$d = \frac{c \cdot \varphi}{4\pi \cdot f_m} + n \cdot \frac{c}{2f_m} \quad (4.28)$$

where φ is the phase shift and f_m is the modulation frequency. These phase time-of-flight systems use a continuous signal with constant frequency which is modulated, and capture the object points simultaneously. This requires a full illumination of the whole area. For safety and cost reasons LEDs in the infrared part of the color spectrum are used. The illumination has to be synchronized with the sensor control. For bigger distances interference can occur which causes ambiguity. The accuracy of a phase time-of-flight system increases with the modulation frequency. The advantages are the low required computing power and the low sensitivity to external light. The resolution is however limited by phase noise caused by changes of temperature, density of the air and instabilities in the supply voltage. Also the reflectance of the object influences the accuracy of the measurement, since dark and bright areas of an object lead to different distance measurements. An example is the latest Kinect system for the Xbox One from Microsoft which uses the time-of-flight technology for motion capturing for video games. Because of the relatively low resolution, time-of-flight sensors can, as of 2015, only be used for macroscopic measurement scenarios on the scale of centimeters and above. (Bednara, Höfler, Nowak, & Wölfelschneider, 2014)

4.2.1.3.2 Interferometry

Interferometry is a phase-based measurement method which is used to measure precisely the profile of a reflecting or a diffuse surface. The uncertainty of the measurement can only be as small as the roughness of the surface. The principle of interferometry is based on the optical interference between an observed light wave and a reference light wave. The two waves are generated by splitting up coherent, monochromatic light. The reference wave covers a path of known length and the measurement wave covers the path which hits the measured object. The difference between the two optical path lengths causes a phase difference between the two waves. If both waves are recombined they will interfere with each other and an interference pattern will be generated. The intensity of the pattern is observed and analyzed. From the evaluation of one or more interference patterns, the properties of the measured object can be calculated. Because of the periodic nature of coherent light waves, the interference pattern is also periodically dependent on the optical path difference. Thus, regulation measures, which limit the possible surface variations to certain values, need to be taken to

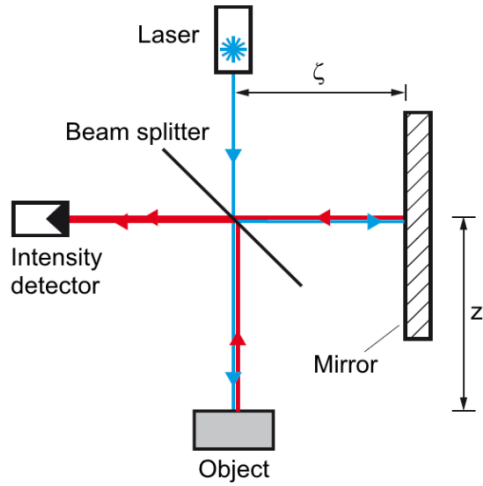


Figure 44: Interferometer principle: Monochromatic light, usually from a laser, is split up into a reference wave (mirror) and measurement wave (object). The two waves are then superimposed and the interference is observed with a detector. (Beyerer, León, & Frese, 2012, p. 372)

gain unambiguous information from the observation of the interference pattern. Also additional measurements with varied wavelengths can be done to decrease the ambiguity. For smooth surfaces with a roughness which is small in comparison to the wavelength of the used light, macroscopic interference patterns are observable. These patterns are characterized by interference stripes which are used in the classic interferometry. If the wavelengths, however, are small in comparison to the roughness of the surface, speckle dominate the pattern. Such speckle patterns are used in the speckle-interferometry. Usually, lasers with a coherent wavelength which is large in comparison to the dimensions of the setup are used as a monochromatic light source. The laser light is split up into the reference wave which is reflected by a mirror onto the detector and covers the distance ζ , and the measurement wave which is reflected by the object onto the detector and covers the distance z . Figure 44 shows the principle of an interferometer. (Beyerer, León, & Frese, 2012, pp. 371-372)

Because the distances are covered twice, the optical length is $2z$ and 2ζ respectively. At the detector the interference of the two light waves can be observed. The reference and the object need to have a similar reflectance to generate distinct interference stripes. The maximum intensity is reached if the optical path difference is

$$\delta = 2z - 2\zeta = k\lambda, \quad (4.29)$$

which causes constructive interference. The intensity reaches a minimum if the optical path difference is

$$\delta = k\lambda + \frac{\lambda}{2}, \quad (4.30)$$

which causes destructive interference. The intensity is periodical with period $\frac{\lambda}{2}$ in z and ζ

$$I(z, \zeta) = I\left(z + k\frac{\lambda}{2}, \zeta\right) = I\left(z, \zeta + l\frac{\lambda}{2}\right). \quad (4.31)$$

Therefore, the intensity measurement only leads to unambiguous results in the interval $z \in \left[z_0, z_0 + \frac{\lambda}{4}\right]$. This interval can be increased by using light sources with long wavelengths which hit their economic and technical limits in the infrared part of the spectrum. (Beyerer, León, & Frese, 2012, p. 373)

Using several different wavelengths allows interferometry with synthetic wavelengths, which can be significantly longer than the physical wavelengths. For the easiest case of using only two different wavelengths λ_1 and λ_2 with the condition $\lambda_1 > \lambda_2$ the synthetic wavelength

$$\Lambda = \frac{\lambda_1\lambda_2}{\lambda_1 - \lambda_2} \quad (4.32)$$

is obtained. The synthetic wavelength is longer than both physical wavelengths if

$$0 < \lambda_2 < \lambda_1 < 2\lambda_2 \quad (4.33)$$

is satisfied. For $\lambda_1 \in (\lambda_2, 2\lambda_2]$ it follows that $\Lambda \in [\lambda_1, \infty)$. This increases the interval of unambiguity to $\frac{\Lambda}{4}$. The two different wavelengths can be used to either capture sequential interference patterns and analyze them, or to perform optical parallel measurements. To reconstruct the profile of the surface requires phase unwrapping methods. The height can then be calculated from the reconstructed phase. (Beyerer, León, & Frese, 2012, p. 374)

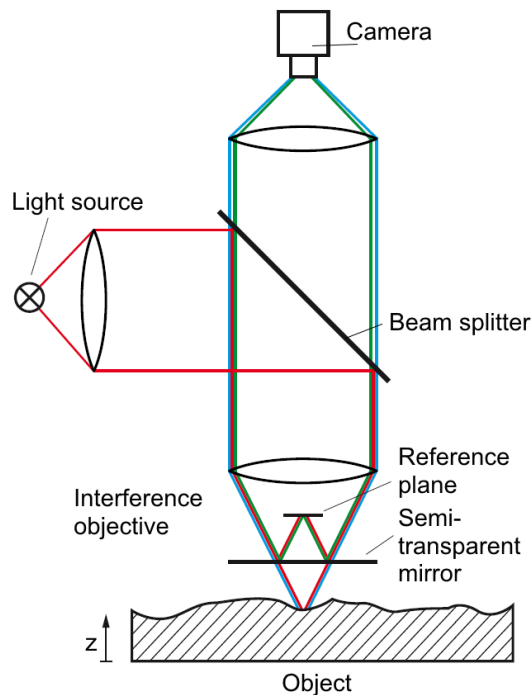


Figure 45: Interferometer using white light. (Beyerer, León, & Frese, 2012, p. 378)

White light with a much shorter coherent length can also be used for interferometry instead of lasers. The maximum constructive interference is achieved when $z = \zeta$. In some spectral ranges constructive interference occurs, while at the same time in other spectral ranges destructive interference occurs. This is due to the fact that all wavelengths are present in white light at the same time. As a result, the variable spectral composure of the observed interference pattern is dependent on the difference $z - \zeta$, which means that the interference pattern which is captured by the camera is color coded. The reference plane of a white light interferometer can be moved, which allows the calculation of the maximum interference for each pixel, from which the profile of the surface can be reconstructed. Figure 45 shows the principle structure of a white light interferometer where the reference plane is integrated into the interference objective. The object is moved along the z-axis and the interference patterns are captured in the corresponding heights by the camera. The analysis of this image sequence leads to the required height information. This principle is called vertical scanning interferometry (VSI).

Another method is the so-called phase shifting interferometry (PSI), where the object is only moved for a tiny fraction of the wavelength of the used light and the

change of the interference stripes is analyzed. This method is similar to the laser interferometry and only applicable for very smooth surfaces which do not exceed a quarter of the wavelength of the used light. Consequently, the VSI method is the commonly used method. (Riedel, 2014)

Most of the white light interferometers are built similarly to microscopes and can only deal with relatively small objects in the area of several millimeters. They are mostly used to measure the roughness and the microstructure of a surface and are limited to flat surfaces. Furthermore, the measurement speed is rather low which makes a real time measurement of the whole surface impossible. (Hill, 2014)

4.2.1.3.3 Digital holography

Holography uses a coherent light source, typically a laser, a capturing medium and a camera to capture the phase information of the reflected light by the object. Holographic capturing means that, similar to photography, the intensity of the reflected light by an object is captured and saved, but additionally a reference wave, which is generated by splitting up the initial light, is superimposed with the captured wave. This leads to constructive and destructive interference and creates a certain interference pattern, the so-called hologram. The classic holography uses a capturing medium, usually some sort of wet chemical photographic plate, to capture the reflected light wave and a reference light wave. The hologram is then illuminated by the reference wave and a camera captures the phase information of the reflected wave from the object. Digital holography uses digital cameras instead of the photographic plate and the reconstruction happens on a computer. Due to the developments of processors and graphics cards, the numerical reconstruction is performed in milliseconds. By analyzing the reconstructed phase map in the plane of the objects surface, the topography of the object can be determined. Digital holography also enables a multi-focus rendering to reconstruct several different planes which are in focus. Hence, no optical focus is required, which differentiates holography from other measurement systems. To overcome the limitations of the classic holography, laser systems which can switch quickly between wavelengths are used. This avoids the limitations of the measurement area and the requirement for smooth surfaces. By subtraction of the reconstructed phase distributions at different wavelengths, the superposition caused by speckle is eliminated. Furthermore, synthetic wavelengths can be calculated and as a result the unambiguous measurement interval is increased. Holography can be used to compare arbitrary formed objects, which have a rough surface, with a reference object. Applications of holography are to measure the difference between a measured object and a reference object, which are physically different, or measure an object under stressed und unstressed conditions. The resolution is only limited by the size of the camera chip and the measurement distance, since no projection system is required. Digital holography is used in manufacturing processes such as deep drawing, stamping, injection molding or electronics. (Carl, 2014)

4.2.1.3.4 Speckle interferometry

The interferometric acquisition of a rough surface shows an interference pattern which is dominated by speckle. Changes in the interference pattern are highly sensitive to the deformation of the measured surface. The two images, the unstressed $g_1(x)$ and stressed $g_2(x)$, are taken and the difference is calculated. While in the separate images no macroscopic interference patterns can be observed, the calculated difference image shows a significant interference pattern. A special application of speckle interferometry, the shearography, is the measuring of inner defects of an object under stress. (Beyerer, León, & Frese, 2012, pp. 378-379)

4.2.1.4 Measuring range and uncertainty of optical methods

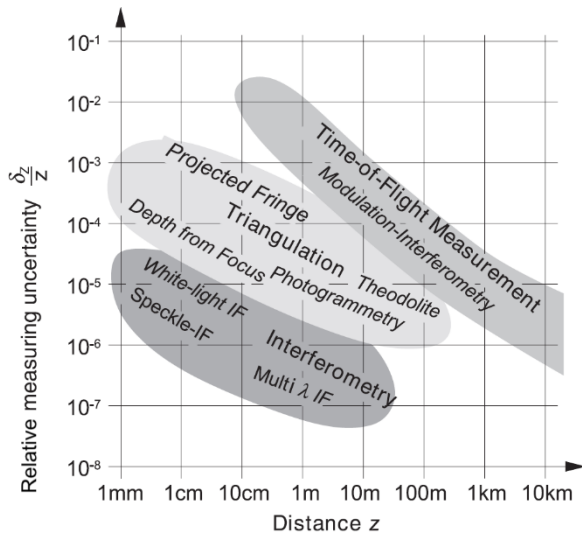


Figure 46 summarizes the measuring range and resolution of the optical methods presented in this chapter. On the y-axis the relative uncertainty of the measurement is plotted and on the x-axis the distance to the object is plotted. It should be noted that, due to electronic and mechanical instabilities, the accuracy of the measurement can be much worse than the measuring uncertainty. (Schwarte, Häusler, & Malz, 2000)

Figure 46: Measurement uncertainty of optical methods in relation to the measurement distance. (Schwarte, Häusler, & Malz, 2000, p. 180)

4.2.2 Acoustic methods

Instead of using light waves to measure the shape of an object, sound waves can be used as well. The SONAR (Sound Navigation And Ranging) is one example of acoustic methods which is commonly used to determine the distance to an object. But also cameras which have an automatic focus very often use this technique to determine the range. The method is very similar to the optical time-of-flight method, but instead of using a light source to emit the measurement waves a sound source is used. The sound wave is reflected by the surface of an object and the distance between the source and surface can be calculated using the known speed of sound. Since sound waves have some of the same basic properties as light waves, they can also interfere with each other, which often causes problems. Also noise coming from the surroundings influences the measurement significantly. An example for an application of an acoustic method are ultra-sound devices, which are used to display a cross-section of an object and capture material data of the inside of an object. (Ali, 2005)

4.2.3 Magnetic methods

Magnetic methods use magnetic touch probes which measure the strength of a magnetic field to sense the location and orientation of an object. This principle can only be used for materials which interact with the magnetic field. Magnetic methods are also used in similar fields of application as acoustic methods when the internal material properties and structure of an object are of interest. In the field of medicine magnetic resonance imaging is used to activate atoms in the material by applying their resonance frequency and then measuring the response. (Ali, 2005)

4.3 Practical problems of 3D-data acquisition

4.3.1 Calibration

The calibration is one of the most important parts of installing and using a 3D-measurement system. The calibration includes the extrinsic parameters, such as the position and orientation of the sensor, and the intrinsic parameters which are determined by the distortions of the objective and non-linear electronics in the cameras. The calibration ensures that all systematic errors are known and can then be included into the calculation which reduces or completely eliminates their influence. Calibration is also very important when using multiple views because the known position and orientation of the different perspectives is needed to combine the scans. (Martin & Várady, 1996, pp. 13-14)

4.3.2 Accuracy

The accuracy of optical 3D-measurement systems typically depends on the resolution and the chosen field of view of the used sensors. Furthermore, the working distance, the appropriate illumination and the precision of the moving parts of the measurement system also contribute to the overall measurement error. Mechanical and optical properties are influenced by the ambient conditions, such as temperature, humidity and altitude, which also influence the accuracy of the measurement system. (Martin & Várady, 1996, pp. 13-14)

4.3.3 Accessibility

Very often certain areas of the measured object are very small, narrow or steep which makes the acquisition difficult. Some features of an object, such as bores and holes, are usually very difficult to capture by the measurement system. Also edges of dense packed objects are very hard to detect. There are different solutions to obtain a complete scan, such as performing multiple scans of the object which includes moving the object and the measurement system relative to each other. (Martin & Várady, 1996, pp. 13-14)

4.3.4 Occlusion

Occlusion is the blocking of sight path of the sensor and usually occurs when using only one measuring device from one perspective and fixtures which hold the object in place. Then some areas of the object cannot be seen by the sensor and therefore it is not possible to reconstruct them. Occlusion can be reduced by using multiple shots from different perspectives and combining them. The images can either be captured simultaneously by several sensors, which is usually more accurate, or sequentially by moving the sensor or the object. Occlusion is one of the major challenges for optical sensors, but also acoustic and magnetic scanners can be affected by that issue. (Martin & Várady, 1996, pp. 13-14)

4.3.5 Noise and incomplete data

Noise is usually generated by the environment of the measurement system and the measured object. Vibrations, extraneous light and reflections are the main sources of noise. To eliminate the noise from the acquired data, several filter approaches are used, as, for example, surface smoothing algorithms. This might, however, only be desired in certain areas of the measured object and may cause problems when the unique identification of certain features is necessary. Another problem occurs when data is missing due to occlusion or inaccessibility of the areas. Additionally, the data at and around edges is usually unreliable. (Martin & Várady, 1996, pp. 13-14)

4.3.6 Surface finish

The surface of the object can significantly influence the measurement process, depending on its roughness and reflectance. Optical methods usually perform better when measuring smooth surfaces because less noise is generated. On the one hand, when using a rather low illumination intensity, the signal-to-noise ratio is decreased, which makes the acquisition of areas with a low reflectance almost

impossible. On the other hand, when using a high illumination intensity, depth from regions with a high reflectance cannot be recovered due to pixel saturation. Objects which are built up of regions with different optical properties are consequently difficult to reconstruct. Regarding structured light projection techniques, most binary coded techniques assume that the objects have a uniform reflectance, otherwise, the reconstruction would not be possible. (Martin & Várady, 1996, pp. 13-14)

4.4 Performance evaluation of 3D-data acquisition systems

There are many factors which can be used to evaluate the performance of a 3D-data acquisition system. The following three aspects are the most commonly used ones.

4.4.1 Accuracy

The accuracy of 3D-measurement systems defines the maximal deviation of the calculated position of the object point from the actual position of the object point. The accuracy of the measurement very often depends on the measurement direction. There is not a norm which defines what value has to be provided by the manufacturers of 3D-measurement systems to describe the accuracy of their system. Some manufacturers use an average error, others provide the uncertainty of the measurement or present the standard deviation or any other statistical value. This makes a direct comparison of 3D-data acquisition systems rather difficult. (Geng, 2011)

4.4.2 Resolution

The optical resolution is defined as the capability of an optical system to distinguish individual points in an image. When evaluating 3D-data acquisition systems, the smallest area of the objects surface which the system can resolve defines the resolution of the system. Another possibility to describe the resolution is the maximal number of measurement points which a 3D-measurement system can capture with a single shot. These two definitions can be converted to each other. (Geng, 2011)

4.4.3 Speed

The measurement speed is especially important when capturing fast moving scenes, such as the analysis of vibrations, and for real time systems to interact with their surroundings. If only a single shot is taken by the 3D-acquisition system, then the frame rate represents maximal measurement speed. For sequential 3D-acquisition systems, the required computing speed additionally increases the measurement time. This is especially the case, if these systems have to deal with moving objects because the movements have to be considered in the calculation. This requires post processing of the images, which provides an integrated result, rather than a snapshot of the scene. (Geng, 2011)

4.4.4 Primary performance space

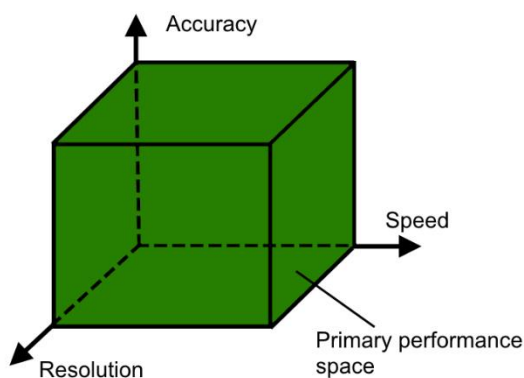


Figure 47 shows the primary performance space of every 3D-measurement system which is defined by the three factors accuracy, resolution and speed. It should be noted that there is always a trade-off between these three factors. Of course, an evaluation can be extended at will by several other factors, such as the price and reliability of the system. Each type of 3D-measurement system has certain advantages and disadvantages and has to be evaluated by its overall performance for the intended application. (Geng, 2011)

Figure 47: Primary performance space for 3D-measurement systems consisting of accuracy, speed and resolution. (Geng, 2011)

4.4.5 Other requirements

Additionally to the fundamental factors, secondary requirements exist which should ideally be fulfilled by a 3D-measurement system. These are, for example, an automated calibration process and an automated data acquisition process to efficiently assure the accuracy and the quality of the measurement. The accuracy and the uncertainty of the measurement should be displayed to the user. The hardware composition should be flexible as well. The system should also be robust to variations of the optical properties of the measured objects, such as reflections, to reduce the measurement error. (Gühring, 2002)

5 Projection techniques

The goal of this work is to provide a projection unit for a fast bin picking application which uses a structured light method to compute the 3D point cloud. The algorithm uses a sequence of patterns, which are projected very fast onto the objects. The patterns are binary (1-bit) and therefore only require one color (logical 1) and black (logical 0). Each scene is captured by high speed CCD cameras. The projector only projects the pattern sequence and is not used for the triangulation thus calibration is not necessary. The projector should only use green light (500 to 600 nm) as illumination because the CCD cameras have the highest sensitivity in that part of the spectrum. Furthermore, chromatic aberration of the lens systems is not a problem when using a monochromatic light source.

5.1 Basic principle

Regardless of the projection technology, the projection process requires a common series of optical operations which differ slightly depending on the technology which is used. The basic principle of a device which projects images onto a surface is shown in Figure 48:

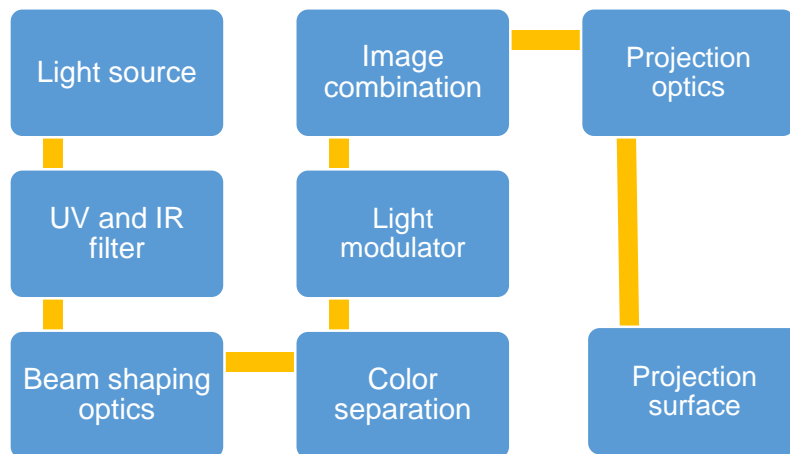


Figure 48: Basic principle of a projecting device

A light source supplies a light modulator with light. Usually, reflectors and lenses direct the light from the light source to the light modulator and from the light modulator into the projection optics. The projection optics then focuses the image onto the projection surface. A controller is used to synchronize the light source with the light modulator.

5.2 Light modulation

5.2.1 Slide projector

A slide projector is an opto-mechanical device for displaying photographic slides on a projection surface. A slide projector is usually built-up as illustrated in Figure 49:

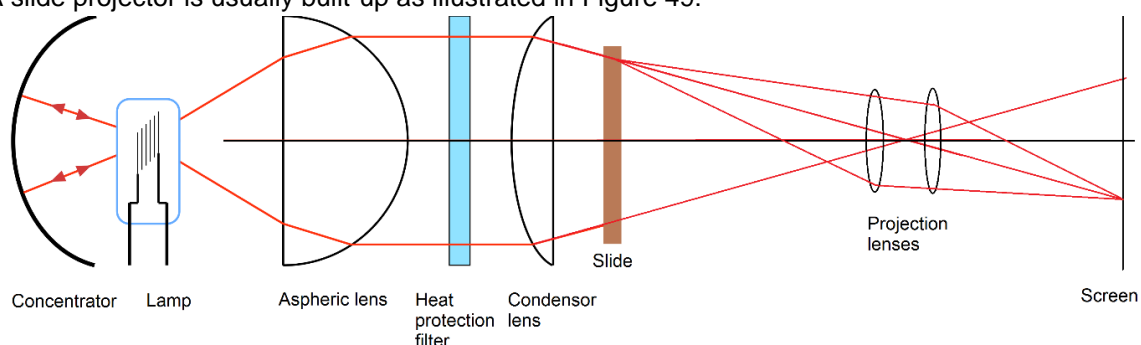


Figure 49: Slide projector principle: Light passes a lens system and illuminates a slide which contains the image. Projection lenses then focus the projection onto a screen.

The light of the lamp is concentrated and directed by a lens system to the slide. The light then shines through the slide which produces the image. An objective lens system is used to image the slide on the screen.

Slide projectors have mainly been used between 1930 and 2000, but have since been replaced by image files on digital storage media shown on a projection screen by using a video projector or a video monitor. Kodak produced the last series of slide projectors in 2004 and apart from second hand, there are only few available on the market. Switching slides can either be done manually or, if a slide magazine is used, automatically. The time between two subsequent slides is limited by the switching mechanism which normally leads to a projection frequency of 1 Hz or lower.

5.2.2 Movie projector

A movie projector is an opto-mechanical device for displaying motion picture film by projecting it onto a screen. The principle is similar to the slide projector and shown in Figure 50:

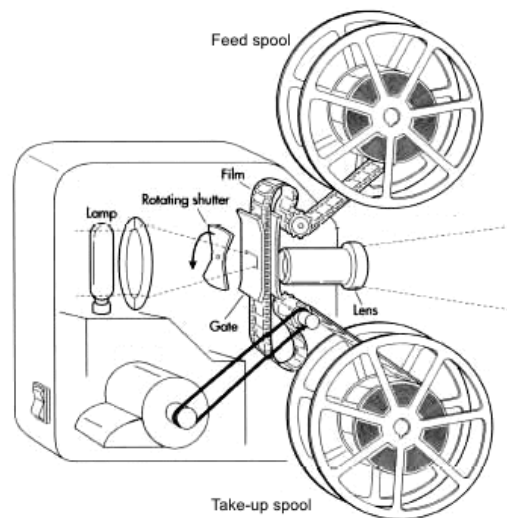


Figure 50: Movie projector principle: A film is fed from the upper spool and stopped at the gate. Light illuminates the image and a lens projects the image onto a screen. During the change of one image to the next, a rotating shutter blocks the light path. (Munday, 2006)

The single slides are connected to a film which enables a faster slide switching mechanism and as a result higher frame rates. A light source shines through the film and the image is projected onto the screen. The frame which needs to be displayed is stopped in the light path. To avoid that the viewer notices the frame changing, a shutter between the light source and the film interrupts the emitted light. The shutter gives the illusion of one full frame being replaced exactly on top of another full frame. For cinemas a frame rate of 24 Hz is standard, which is due to the fact that usually the human eye notices flickering if the frame rate is lower than 16 Hz. Physiologists have found that the human eye can differentiate even small changes in luminosity at refresh rates of 40 Hz and below, resulting in a sensation that the image is flickering (Chen, 2011). Modern shutters are designed with a flicker rate of 48 Hz or sometimes even 72 Hz which reduces the perception by the human eye of screen flickering. Since the film is usually made of polyester, the frame rate of a movie projector is limited by the durability of the film.

Similar to slide projectors, movie projectors are being replaced by digital projectors and are not produced anymore. The company Steenbeck still produces editing tables for archives and restoration facilities. Steenbeck's flatbed editors scan the images with a rotating prism, so there is no intermittent movement of the film. Due to this mechanism in combination with soft-edged nylon rollers, the flatbed editors are very gentle to film stock. This also enables frame rates of up to 200 Hz. (STEENBECK, 2013)

5.2.3 Rotational light modulator

An interesting prototype of a high speed projector was developed by Patrick Wissmann at the University of Technology Aachen in cooperation with the SIEMENS AG Corporate Technology. The approach was to develop a high-speed and low-cost projector for structured light pattern sequence projection. (Wissmann, Forster, & Schmitt, 2011)

Instead of single slides, a fast rotating binary spatial light modulator (SLM) is used to project the pattern sequence at speeds of several hundred Hz, while enabling a rasterization as low as 2 μm . The concept of the projection unit is shown in Figure 51.

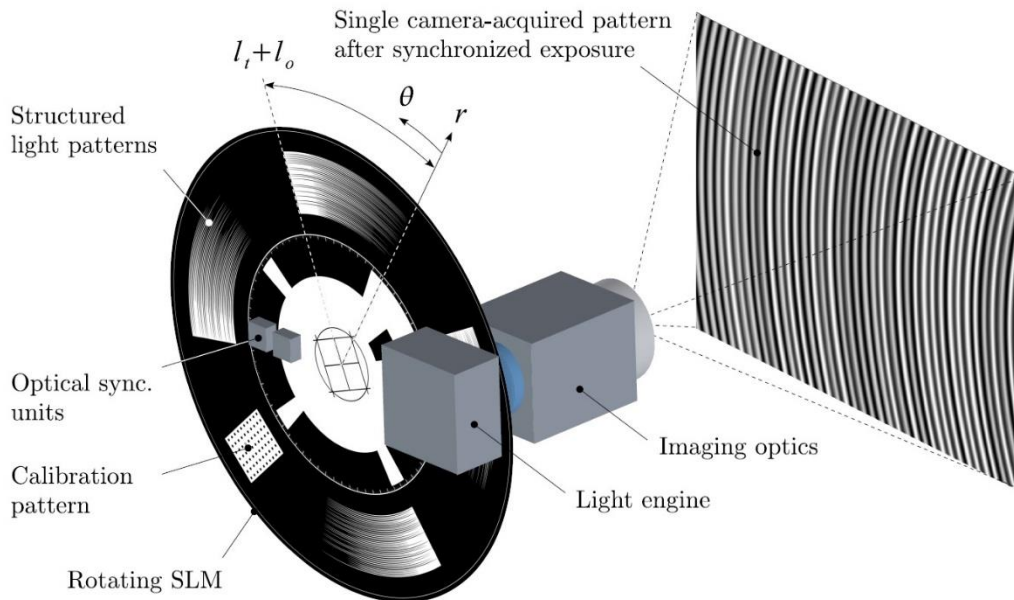


Figure 51: Concept of rotational pattern projection. (Wissmann, Forster, & Schmitt, 2011)

The binary patterns were manufactured via chrome disposition on glass substrate. The series of structured light patterns is realized by rotational motion. The patterns are aligned around the center of the spatial light modulator illuminated by a light engine and projected onto the measurement surface by the imaging optics. The two generations of the prototype are shown in Figure 52.



Figure 52: First (left) and second (right) generation of analogue pattern projection unit. (Wissmann, 2013)

The projection frequency is 400 Hz for 8 bit/pixel, and with two high-speed cameras and the used algorithm a 3D-reconstruction rate of 20 Hz is achieved. The rotational speed of the SLM is set by the controller of a brushless electric motor. A microcontroller is used to control the pattern projection sequence which is synchronized with the SLM rotation. A light-emitting diode (LED) is used which is only activated during certain times within a projection cycle to increase the lifetime and remove the necessity for using active cooling. The SLM of the first generation has a grouped distribution of translucent and opaque pattern regions. (Wissmann, 2013)

For the second generation, the design was further optimized, with the focus on increasing the robustness, reducing the size and making the projection unit more cost-efficient. Furthermore, the SLM makes use of a dither strategy which means that the given grey-scale image is converted into black and white pixel. The ratio of black to white pixel in the new image then approximates the average level of grey in the original image. (Wissmann, 2013)

The technical specifications of the two generations are summarized in Table 1.

| Property | 1 st generation | 2 nd generation |
|---------------------------------------|----------------------------|----------------------------|
| Radial pixel number | 2560 | 3520 |
| SLM pixel size in μm | 5 | 2 |
| SLM resolution in Mpixel ⁵ | 324 | 494 |
| SLM speed in rpm ⁶ | ≈ 2500 | ≈ 2500 |
| SLM diameter in mm | 90 | 55.6 |
| Projected area in mm^2 | 200 x 150 | 170 x 130 |
| Working distance in mm | 220 | 310 |

Table 1: Technical specifications of the analogue pattern projection unit (Wissmann, 2013)

Wissmann pointed out several challenges in the manufacturing process of the prototype. Apart from mechanical errors caused by concentric and axial run-out, the alignment procedure often lead to eccentricity. The manufacturing process of the SLM was another source for errors and Wissmann concluded that a more accurate process needs to be developed. However, the prototype showed the capability of projecting patterns at high speeds while relying on of-the-shelf components. Wissmann pointed out the cost efficiency and provided a further outlook for a hand-held 3D-scanner. (Wissmann, 2013)

5.2.4 Array Projector

A concept developed by the FRAUNHOFER Institute for Applied Optics and Precision Engineering (IOF) enables pattern projection with rates of several kHz. The goal was to fulfill three aspects: fast pattern changing, high illumination and compact design. This concept was inspired by the structure of compound eyes of insects (Breitbarth, 2012). The principle of the array projector is shown in Figure 53 and is very similar to the principle of a slide projector:

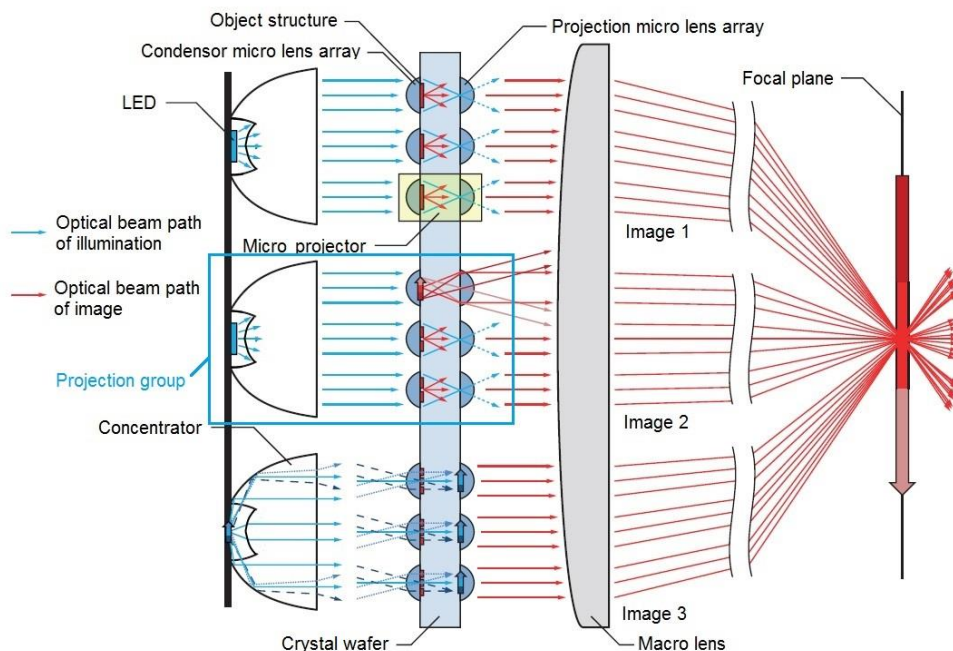


Figure 53: Array projector principle: a projection group contains the same image and consists of a LED, a condenser lens array and a projection lens array. By powering the LED, the image is projected and the frame rate only depends on the switching speed of the LED. A macro lens focuses the images of the different projection groups. (Heist, Sieler, Breitbarth, Kühmstedt, & Notni, 2013)

⁵ Megapixel

⁶ Revolutions per minute

One projection group consists of an LED with a concentrator which provides the illumination for three micro projectors, which all project the same image. The micro projectors are aligned in one array on the crystal wafer, which serves as a fixture. The images are created by the light which passes through a micro projector. All the images are then multiplexed and focused by a macro lens onto the focal plane. This principle eliminates the necessity to move the SLM, and thus the projection frequency is only dependent on the speed at which the LEDs can be switched on and off, enabling a theoretical frequency of several MHz. The main challenges in the manufacturing process are to miniaturize the single channel projectors, make replicas and align them on one array and finally multiplex the single images on the measurement surface. (Heist, Sieler, Breitbarth, Kühmstedt, & Notni, 2013)

The lenses of the micro projector are made of polymer resin and the object structure is created lithographically on the crystal wafer. The overall depth of the array projector is not dependent on the number of projection groups and since the LEDs are only active for the projection, active cooling is not necessary (Breitbarth, 2012). Pictures of the prototype are shown in Figure 54.

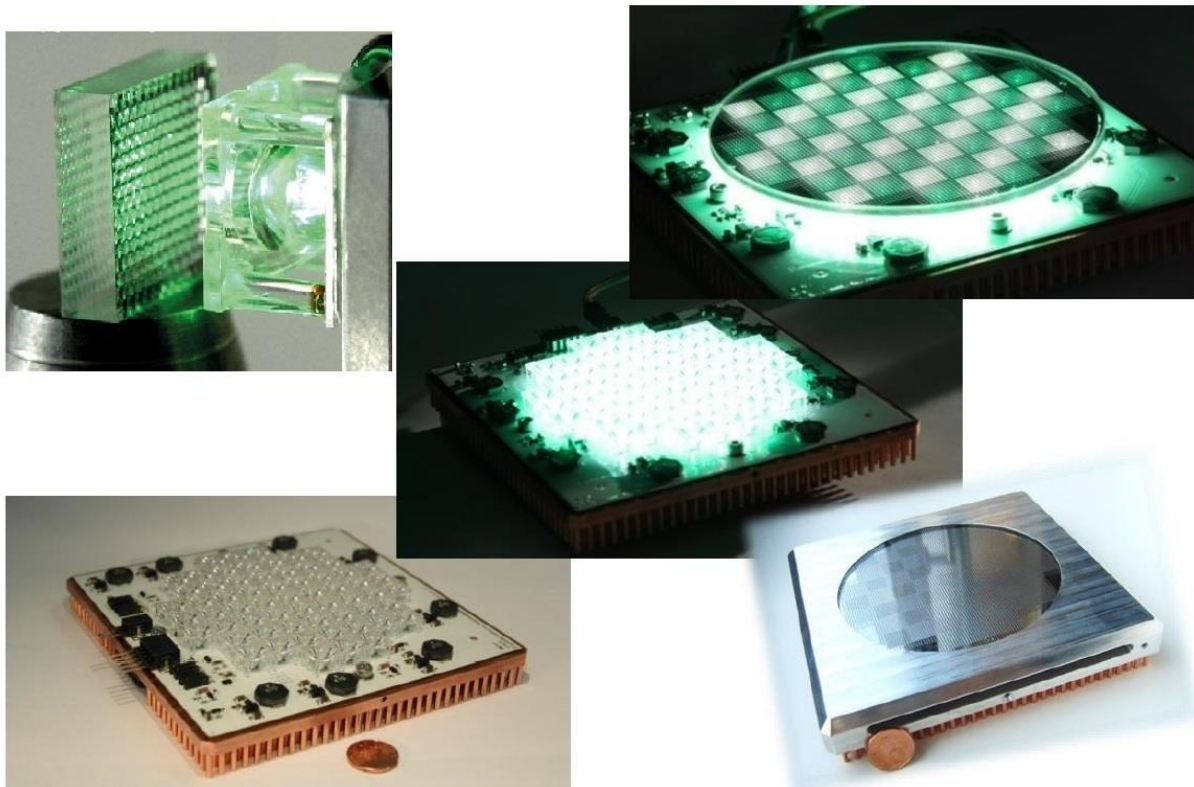


Figure 54: Array projector and crystal wafer (top left) (Notni & Kühmstedt, 2013)

The technical specifications are listed in Table 2:

| Property | Value |
|--|----------------|
| Pixel number | 400 x 300 |
| Pixel pitch in μm | 1.5 |
| Working distance in mm | 1000 |
| Projected area @ working distance in mm^2 | 200 x 200 |
| Maximum illuminance in Lx | 1700 |
| Dimensions in mm^3 | 136 x 136 x 25 |
| Frame rate in Hz | 1000 |

Table 2: Technical specifications array projector (Heist, Sieler, Breitbarth, Kühmstedt, & Notni, 2013)

5.2.5 CRT – Cathode Ray Tube

Cathode Ray tube devices modulate the direction of an electron beam with magnetic fields to project a scene onto a surface. The principle of the cathode ray tube, which was for a long time the common technology used in television sets, is shown in Figure 55.

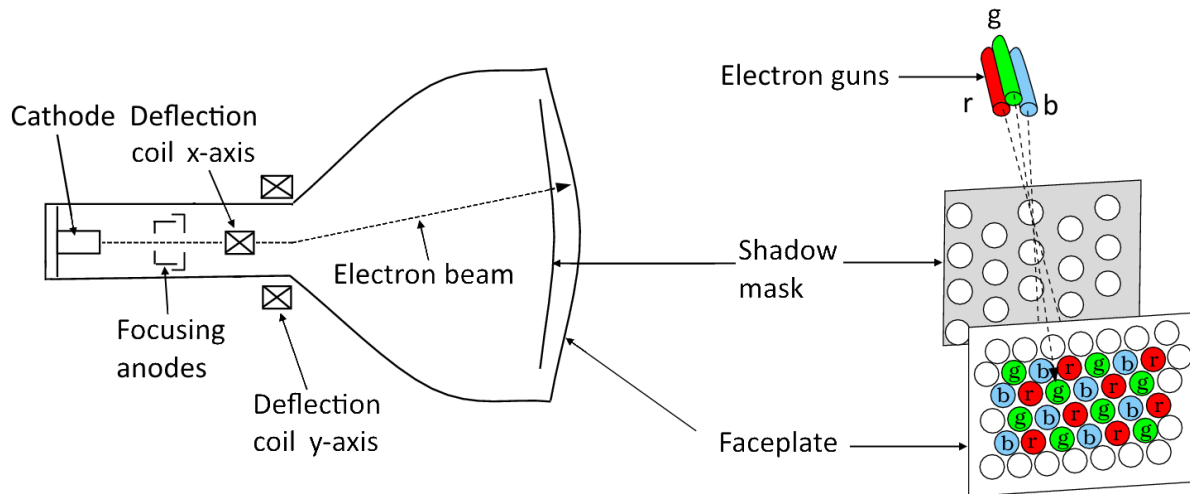


Figure 55: Cathode ray tube principle: the cathode, consisting of three electron guns, emits an electron beam which is deflected by two coils. A shadow mask assures that the correct phosphor on the faceplate is illuminated. (Wandell, 2012)

The cathode is the source of electrons and has one electron gun for each primary color (RGB) arranged either in a straight line or in an equilateral triangular (also called delta) configuration. The electron guns produce beams of rapidly moving electrons which are focused by cylindrical anodes and scan a faceplate made of glass and painted with phosphor. The phosphor, one for each color, absorbs these electrons from the scanning beam and emits light. The intensity of the electron beam can be modulated. Two pairs of deflection coils, one pair for the x-axis and one pair for the y-axis, deflect the beam by an applied potential difference. To separately control the emission of the three types of phosphors, the color of the emitted light can be varied. A metal plate, the so-called shadow mask, prevents electrons from hitting the wrong phosphor by absorption or scattering. The electron beam starts scanning in the top left corner of the screen and rapidly screens line by line down the bottom right corner. (Wandell, 2012)

CRT is a pulse-type display, which means that when it receives the input signal for a black to white transition at the beginning of the frame and immediately reaches full white illumination which then decays rather quickly. In case of a transition from white to black, an inevitable activation of the phosphor occurs due to the passing electron beam. The luminance signal diagram is shown in Figure 56.

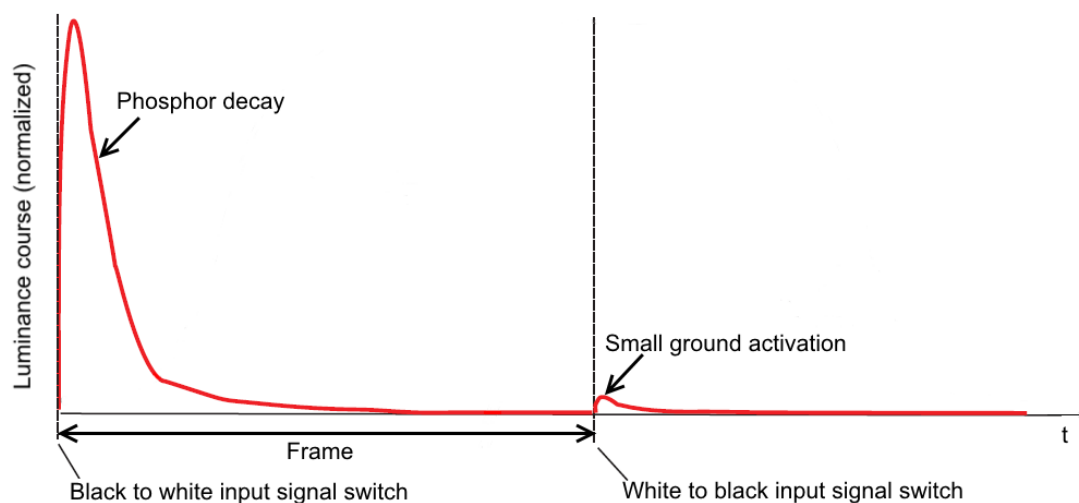


Figure 56: Luminance of a pulse-type display such as a cathode ray tube: For the black to white transition, the maximum luminance is reached shortly after the start of a new frame and decays over time. For the white to black transition, an inevitable activation of the phosphor occurs when the electron beam passes the phosphor. (Elze & Tanner, 2012)

This principle of a CRT can also be used for projection units. Most modern CRT projectors have three separate CRTs, one for each color and optics which interlay the monochromatic images to generate the image as shown in Figure 57.



Figure 57: Sony G70 CRT projector.

Such projectors are able to work with a vertical scan frequency of up to 120 Hz, some even 210 Hz. For such high frame rates, the resolution needs to be reduced, but since the CRT is not fixed to a certain resolution raster, the resolution is variable without deinterlacing. However, CRTs have almost disappeared from the market and have been substituted by the technologies presented below. New projectors are hardly produced anymore and only the ones available on the market are sold by second-hand dealers and are often sold “as-is”. As a result, they often need essential repairs and although replacement parts are still produced, they are only available from a few manufacturers. (VDC, 2015)

Moreover, the dimensions and weight of these projectors are very big and the setup of CRT projectors and the adjustments take considerably more time than comparable projectors and the brightness is considerably lower. Also, the optics are often designed for distances used in simulators and home theaters and thus are not suitable for 3D-measurement applications. Below are the summarized specifications of CRT projectors.

| | Minimum | Maximum |
|----------------------------------|-----------------|------------------|
| Luminous flux in Lm | 450 | 1600 |
| Horizontal scan frequency in kHz | 15 | 180 |
| Vertical scan frequency in Hz | 37 | 210 |
| Pixel number | 640 x 480 | 2500 x 2000 |
| Weight in kg | 30 | 85 |
| Dimensions L x W x H in mm | 600 x 500 x 260 | 1100 x 750 x 350 |
| Size of projection in mm | 650 | - |

Table 3: Technical specifications of CRT projectors (Palme, 2015)

The horizontal scan frequency describes how often the electron beam can refresh one single horizontal line per second. The vertical scan frequency describes how often the electron beam can refresh one vertical column. Due to the working mode of a CRT, which refreshes the display line-by-line, the electron beam has to refresh all horizontal lines to fully refresh one vertical column. Hence, the maximum frame rate of a CRT is defined by its vertical scan frequency.

5.2.6 LCD – Liquid Crystal Display

A liquid crystal display is a hold-type display, which means that, once the display has received an input signal, the brightness increases until the desired level is reached. This level is then held until another input signal is received as displayed in Figure 58.

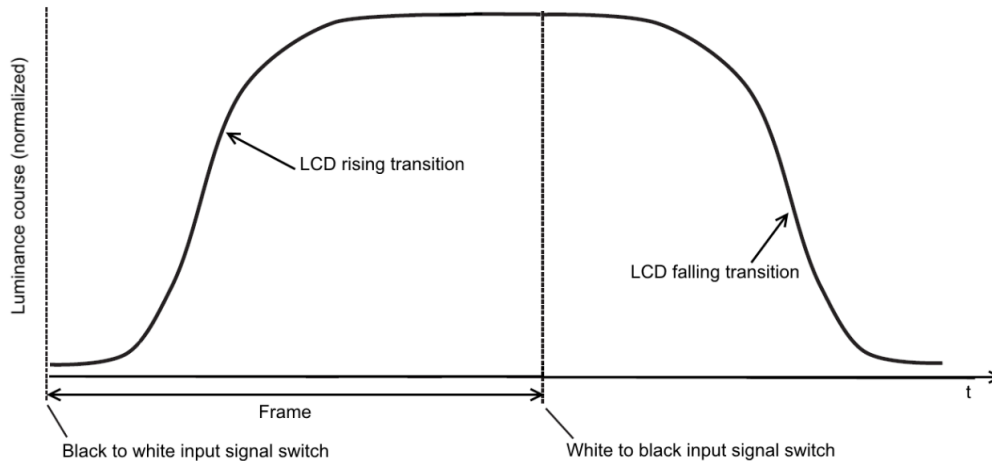


Figure 58: Luminance of a hold-type display such as a liquid crystal display: For a black to white transition, the maximum luminance is reached after a certain amount of time. For a white to black transition, the LCD also requires time to reduce the luminance. (Elze & Tanner, 2012)

The principle of a liquid crystal display relies on the ability to polarize light and control its polarization. In order to obtain the desired polarization effect, birefringent materials can be selected in regard to their particular anisotropic features. Since rotating a solid anisotropic crystal is rather difficult to control, liquid crystals are used instead. (Chen R. H., 2011, p. 61)

A backlight provides the illumination of the LCD cell. The unpolarized light is initially linearly polarized. The linear polarized light then enters the liquid crystal layer. Depending on the alignment of the liquid crystal molecules the polarization state of the linear polarized light is changed by applying an electric field. The primary colors (RGB) are then generated by subpixel color filters. Depending on the operation mode of the LCD, a second linear polarizer then either blocks the light or lets the light pass. Thus the light's intensity is modulated pixel by pixel to generate the projected image. A basic buildup of a liquid crystal cell (which corresponds to one pixel of the image) is shown in Figure 59. Note that color filters are only used for displays. A LCD projector or LED backlight display generates the colors differently as discussed in this section. (Chen R. H., 2011, p. 239)

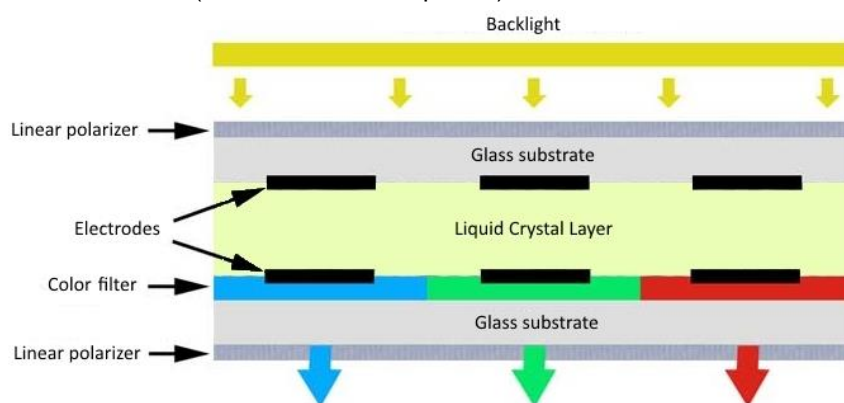


Figure 59: Structure of a liquid crystal cell: The backlight provides the illumination which is then linearly polarized. The linear polarized light enters the liquid crystal layer and depending on the state of the crystal and the voltage at the electrodes, the light is modulated or not. The light then passes subpixel color filter (RGB) and a second linear polarizer either blocks or lets the light pass.

The transparent indium tin oxide (ITO) electrodes are applied on the glass layer and supply the liquid crystal cell with the required operating voltage. The addressing of each cell is performed by thin film transistors (TFT), which allow a precise control of each pixel of the liquid crystal display. (Chen R. H., 2011, pp. 321-323)

The existence of liquid crystals and their electro-optical effects had already been discovered at the end of the 19th century, but until a first prototype was developed and the commercial use was possible, almost a full century had passed. Liquid crystals can be classified as displayed in Figure 60.

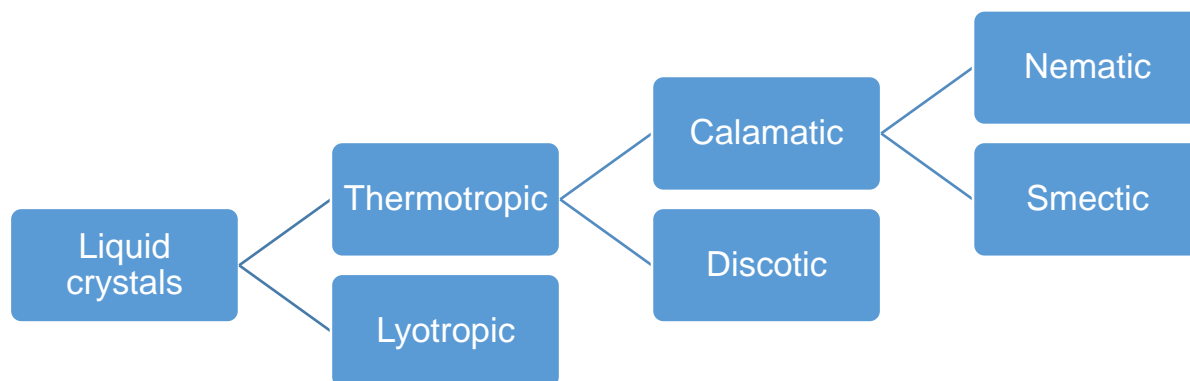


Figure 60: Classification of liquid crystals into thermotropic and lyotropic liquid crystals. The thermotropic can be distinguished by their shape into calamatic and discotic liquid crystals and several others. The calamatic liquid crystals can have different phases such as nematic or smectic. (MERCK, 2015)

The lyotropic liquid crystal phases form in the presence of solvents and for that reason are concentration-dependent. Lyotropic liquid crystals are used for detergents, cosmetics and pharmaceuticals and in medicine. (Chen R. H., 2011, pp. 90-91)

Thermotropic liquid crystals phases are observed by temperature change. Thermotropic liquid crystals molecules can have different shapes and besides the discotic and calamatic liquid crystals, several other shapes exist. Liquid crystals are a mesophase between the solid and the liquid phase of organic crystals and have consequently features of both solid and liquid. A categorization of the phases is shown in Figure 61. (Chen R. H., 2011, pp. 78-79)

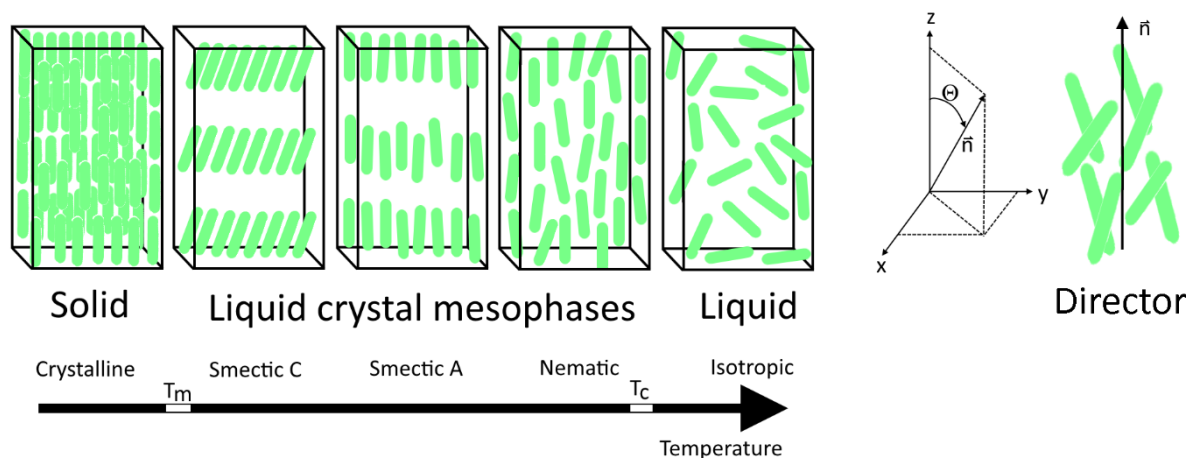


Figure 61: Mesophases of thermotropic liquid crystals: With increasing temperature, the solid crystal becomes liquid, which however does not occur instantly. The crystal transforms into several different mesophases with different alignment of the molecules. (Chen R. H., 2011, pp. 80, 92)

Solid crystalline has both positional and orientational order and all the molecules have the same direction of their long axis, the so-called principle molecular axis or director \vec{n} . At the melting temperature T_m , the crystal structure melts to an anisotropic fluid. The first mesophase is built up of smectic C liquid crystals, which have positional and orientational order. Additionally smectic C liquid crystals have a clear positional layer separation. The director \vec{n} is tilted by an angle θ with respect to the smectic layer normal. As the temperature is increased further the smectic A mesophase is obtained, in which the molecules are more vertically oriented, but are still positioned in layers. The director \vec{n} is parallel with respect to the smectic layer normal. Further increasing the temperature leads to the nematic mesophase. The nematic liquid crystals keep the vertical orientation of the smectic, but no clear positional layer separation is observable anymore. Exceeding the clearing temperature T_c the fluid clears to an isotropic liquid, which has neither positional nor orientational order. (Chen R. H., 2011, pp. 79-83, 92)

Liquid crystal molecules can also be made chiral, either by substituting one or more atoms or by adding chiral dopants at different concentration to the liquid crystal. The introduction of chirality to a system changes its properties and several phases show helical superstructures, where the movement of the director \vec{n} along the z-axis describes a spiral as shown in Figure 62. Chiral nematics also have additional phases, the so-called Blue Phases, which have different properties than ordinary nematics. The name of the blue phases is derived from Reinitzer's first observation in 1888, which was a blue flash of light at the transition from the liquid crystal phase to the isotropic fluid phase. There are numerous chirality related effects observed, such as structural and molecular optical activity, which can be exploited in display technologies. Also electric effects such as (anti-)ferroelectricity occur in the blue phases. (Dierking, 2014)

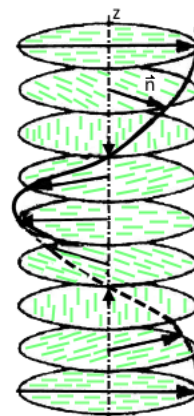


Figure 62: Helical superstructure caused by the introduction of chirality to the liquid crystal (Dierking, 2014)

The three different types of Blue Phases are BPI (body-centered cubic structure as illustrated in Figure 63), BPII (simple cubic structure) and BPIII (symmetry as isotropic phase).

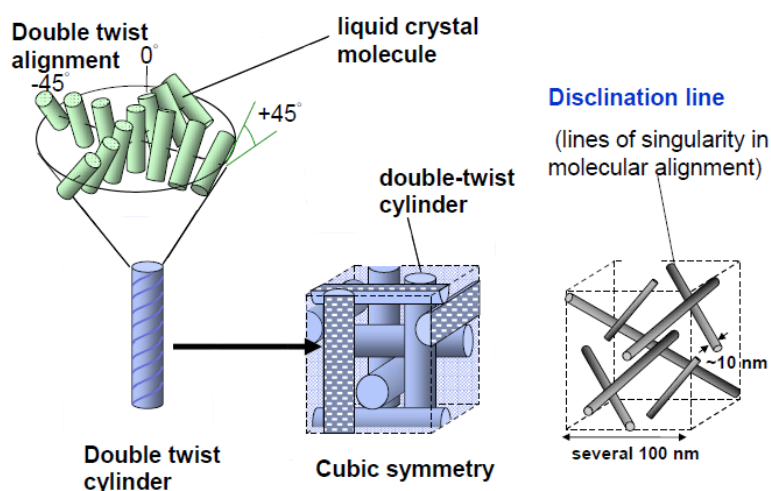


Figure 63: Structure of Blue Phase I: The liquid crystal molecules are aligned in a double twist cylinder. The double-twist cylinders have cubic symmetry in the structure. (Kikuchi, 2010)

The temperature-chirality diagram for the three Blue Phases is shown in Figure 64. "Crit." is the critical point where the phase boundaries vanish.

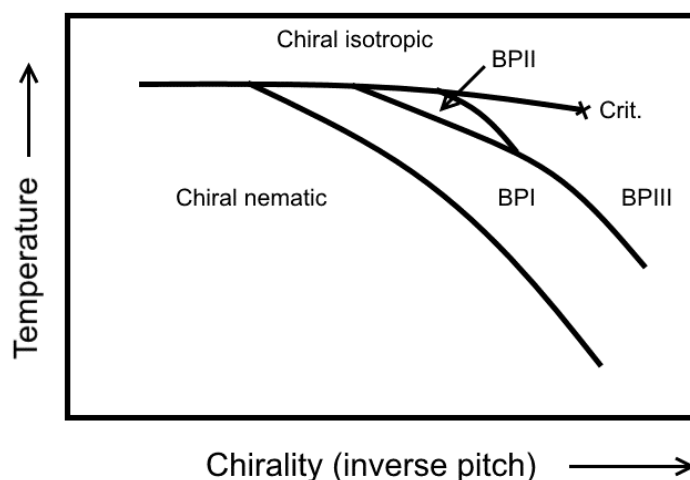


Figure 64: Temperature - Chirality diagram of the three different Blue Phases. Introducing chirality generates Blue Phase I, whose stability increases for increasing chirality. Blue Phase II is obtained for intermediate chirality. Blue Phase III is observed at maximum chirality and its stability also increases until it is dissolved at the critical point. (Dierking, 2014)

Another possibility of adding chirality to a liquid crystal mesophase is using the smectic C liquid crystals and adding a dopant. This causes the tilted layers to twist following a chiral helix. Thus the orientation of the director \vec{n} changes when progressing through the liquid crystal layer. Due to the intrinsic charge separation the chiral smectic C is thus polar. Since the molecules of the smectic C liquid crystal have a natural directional orientation, similar to magnetic materials, the intrinsic polarization is called ferroelectric. Ferroelectric liquid crystals (FLC) are currently a very active field of research. Smectic A liquid crystals are nonpolar due to the vertical orientation of the molecules, and even the addition of a chiral dopant will not change this. (Chen R. H., 2011, pp. 86-88)

The property that makes the use of liquid crystals as a display technology possible is the ability to change the orientation of the liquid crystal molecules without changing the orientation of the whole crystal. To control the birefringence of the liquid crystal, the molecules need to have a suitable dynamic response to electric fields and the correct dielectric anisotropy. (Chen R. H., 2011, pp. 92, 97)

A certain liquid crystal layer with a birefringence of $\Delta n = n_e - n_o$, with n_e being the effective higher refractive index in the direction of the extraordinary beam and n_o being the effective lower refractive index in the direction of the ordinary beam, and thickness d causes a phase difference φ for light with wavelength λ as (Chen R. H., 2011, p. 243)

$$\varphi = \frac{2\pi}{\lambda} \cdot \Delta n \cdot d. \quad (5.1)$$

The best results are obtained with molecules which have a long rod-like structure with a stiff spine and flexible ends. The flexible ends provide the function of a joint, the stiff spine makes sure that the molecules are able to maintain the positional and orientational order and the long rod-like structure reduces the intermolecular collisions and further promotes parallel ordering. The molecules are intrinsic dipoles and therefore react to external electric fields, which induce dipole moments and change the orientation of the molecules and as a result the refractive index of the liquid crystal layer. (Chen R. H., 2011, pp. 97-99)

This effect is called the Kerr effect. The change of the refractive index Δn is

$$\Delta n = \lambda \cdot K \cdot E^2 \quad (5.2)$$

where E is the amplitude of the electric field, λ is the wavelength and K is the Kerr constant. The change to the refractive index Δn is linearly proportional to E^2 . As the electric field increases, the birefringence will gradually saturate until it reaches the maximum of the liquid crystal. (Rao, Zhibing, Sebastian, Kuan-Ming, & Shin-Tson, 2010)

The material properties of the liquid crystal define the features of the LCD as, for example, the response time, operating voltage, electric resistivity, viewing angle and contrast. The refractive indices and the thickness of the liquid crystal layer determine the phase retardation of the light which passes through. The elasticity and the dielectric constant of the liquid crystal layer define the threshold voltage and resistivity. The response time, which is the time required for the transition black to white to black by the liquid crystal display (ISO 9241-302:2008), depends on the viscosity, the thickness, the elasticity and the temperature of the liquid crystal layer. (Chen R. H., 2011, pp. 99-100)

Smectic liquid crystals have a high viscosity and can retain their orientation in absence of an electrical field, which is why they usually consume less energy than the nematic liquid crystals. They are used in static or slow-moving displays such as advertising panels. The nematic liquid crystals have a low viscosity and are more sensitive to electric fields, which enables faster response times (<40 ms) and consequently the use for fast-motion displays and projectors. The Blue Phase⁷ liquid crystals have the fastest response time (<1 ms) and several advantages in the production process, as they are easier to manufacture. (Chen R. H., 2011, pp. 80, 81, 388)

Different nematic liquid crystal layers have been developed to increase the contrast and viewing angle and reduce the operating voltage and response time. Due to the anisotropy of the liquid crystal its dielectric constant is different in different directions. The liquid crystals dielectric anisotropy $\Delta\varepsilon$ is defined as the difference between the dielectric constant parallel to the principle molecular axis ε_{\parallel} and the dielectric constant perpendicular to the principle molecular axis ε_{\perp} of the liquid crystal as

$$\Delta\varepsilon = \varepsilon_{\parallel} - \varepsilon_{\perp}. \quad (5.3)$$

When $\Delta\varepsilon > 0$, the anisotropy of the liquid crystal is positive and the intrinsic electric dipole moment is aligned parallel to the principle molecular axis of the liquid crystal. When $\Delta\varepsilon < 0$ the anisotropy of the liquid crystal is negative and the intrinsic electric dipole moment is aligned perpendicularly to the principle molecular axis. The applied electric field of most liquid crystal displays is aligned perpendicularly to the glass substrate surface because of an easier manufacturing process. As a reaction to the applied electric field E the liquid crystal molecules will rotate to align the intrinsic dipole

⁷ Blue Phase liquid crystals are, as of 2015, currently developed and are an active research field.

moment p with the electric field as illustrated in Figure 65 (left). The twisted nematic (TN) liquid crystals, for example, usually have a positive anisotropy hence in the equilibrium position the intrinsic dipole moment p is oriented parallel to the glass substrate surface. The vertical alignment (VA) liquid crystals usually have a negative anisotropy so in the equilibrium position the intrinsic dipole moment is aligned perpendicularly to the glass substrate surface. (Chen R. H., 2011, pp. 349-351)

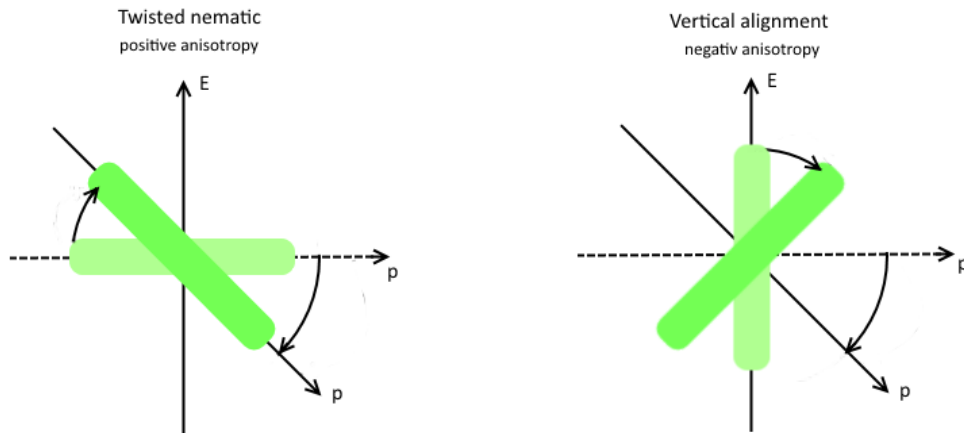


Figure 65: Rotation of the twisted nematic (TN) with positive anisotropy and of the vertical alignment (VA) with negative anisotropy. As a reaction to the applied electric field E the liquid crystal molecules will rotate in the effort to align the intrinsic electric dipole moment p to the electric field. (Chen R. H., 2011, p. 350)

The TN mode is the commonly used liquid crystal layer and was the breakthrough that made LCDs practical. The two glass substrate surfaces are rubbed in one direction and as a result the nematic liquid crystals orientate parallel to the rubbing direction. If the rubbing directions of the two substrates are perpendicular to each other, the liquid crystal will twist. The optical axis of the two linear polarizers are parallel to the respective rubbing direction, so their optical axis are also perpendicular to each other. When the incident light passes through the twisted nematic layer, it will rotate and follow the 90° twist. When the electric field is applied, a dipole moment is induced and the molecules align along the electric field because of its positive anisotropy. As a result the twist is removed, the polarization of the incident light does not rotate and the light is therefore blocked by the second polarizer as displayed in Figure 66. This is the so-called normally white mode, which, besides a very good contrast, additionally conserves power. (Takatoh, et al., 2005, pp. 103-104)

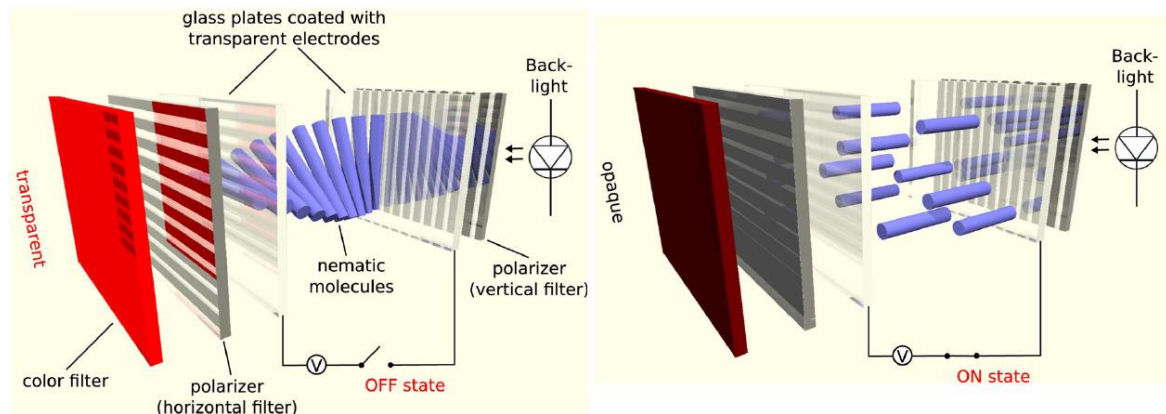


Figure 66: Twisted nematic in normally white mode (Elze & Tanner, 2012)

In the VA mode, which was developed by researchers of MERCK, the nematic liquid crystals are aligned with their molecular axis perpendicular to the glass substrate as shown in Figure 67.

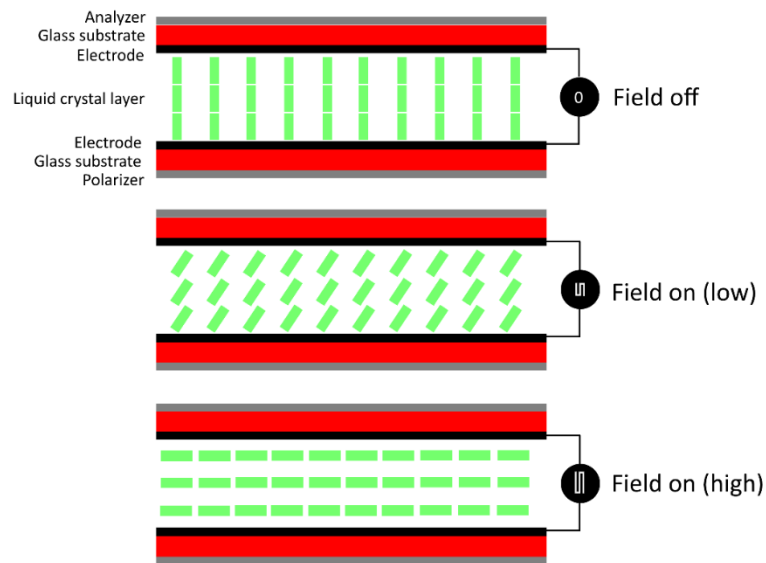


Figure 67: Vertical alignment (VA) liquid crystals (Chen R. H., 2011, p. 370)

If there is no electric field applied, the incident linearly polarized light will pass the VA liquid crystal layer without any changes to its polarization state. Thus the analyzer, which is rotated 90° to the polarizer, will block the light. This normally black mode has certain advantages, as it is insensitive to temperature changes, layer thickness or wavelength, which leads to a very good contrast ratio. When an electric field is applied, the molecules will align with the direction of the applied field because of their negative anisotropy. This causes a phase retardation of the linear polarized light and enables the light to pass through the analyzer. The drawback is that the white mode is dependent on wavelength, layer thickness and temperature. The VA liquid crystals enable a smaller cell gap and can thus reduce the response time, the drawback is the poor oblique viewing angle quality. (Chen R. H., 2011, pp. 370-372)

There are two possible modes for the vertical alignment which both try to improve the viewing angle quality by reducing unwanted phase retardation in the middle of the liquid crystal layer. This unwanted phase retardation causes significant light leakage. The first one is the Multiple-Domain Vertical Alignment (MVA) developed by FUJITSU, which introduces an opposite phase retardation to eliminate light leakage. As displayed in Figure 68, protrusions are constructed on both glass substrates which produce an opposite phase retardation. This improves the wide-viewing angle quality significantly and also provides a good grayscale stability. (Chen R. H., 2011, pp. 372-374)

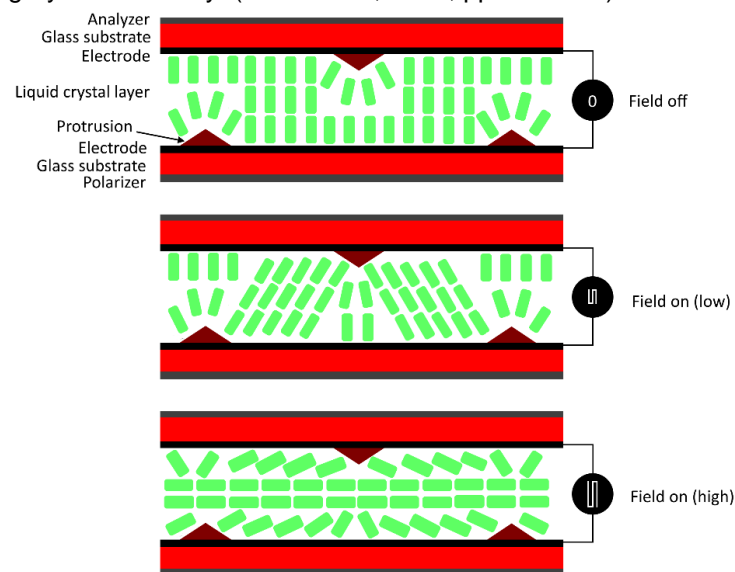


Figure 68: Multi-domain vertical alignment (MVA) liquid crystal. (Chen R. H., 2011, p. 373)

The second vertical alignment mode is called Patterned Vertical Alignment (PVA), which was developed by researchers of SAMSUNG. The PVA mode uses anti-symmetric slits, which cause a slightly bent electric field. This bent electric field generates areas of different tilted molecules as shown in Figure 69. (Chen R. H., 2011, pp. 375-376)

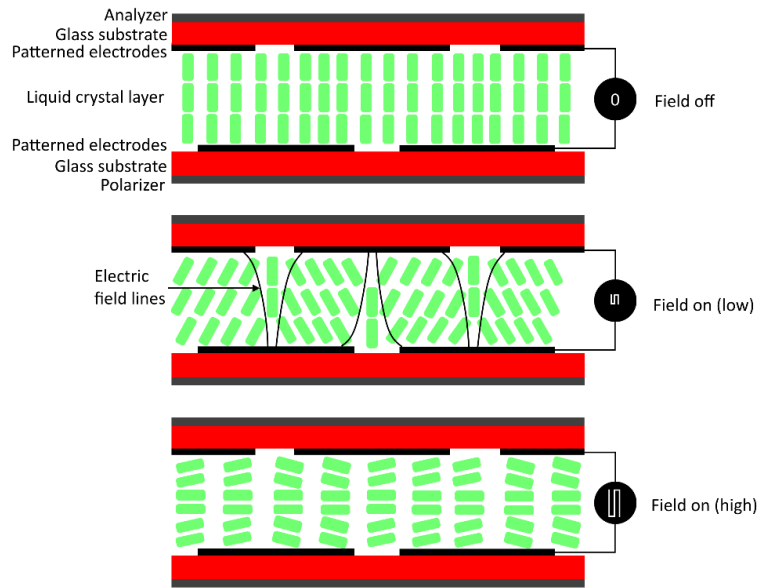


Figure 69: Patterned vertical alignment liquid crystal. (Chen R. H., 2011, p. 375)

Unlike the MVA, the PVA does not have any protrusions, so the normally black mode is unchanged. In the white mode, almost all the molecules are homogeneously aligned, which causes almost no unwanted phase retardation. This provides a very good display contrast. Several companies actively pursue the improvement to vertical alignment modes. (Chen R. H., 2011, pp. 375-376)

Another possibility to improve the viewing angle quality is to use a transverse electric field which restricts the liquid crystal molecules to only rotate parallel to the glass substrate. This mode is called In-plane Switching mode (IPS) and was developed by researchers of HITACHI. As illustrated in Figure 70 the molecules are homogeneously aligned, lying parallel to the glass substrate. (Chen R. H., 2011, p. 376)

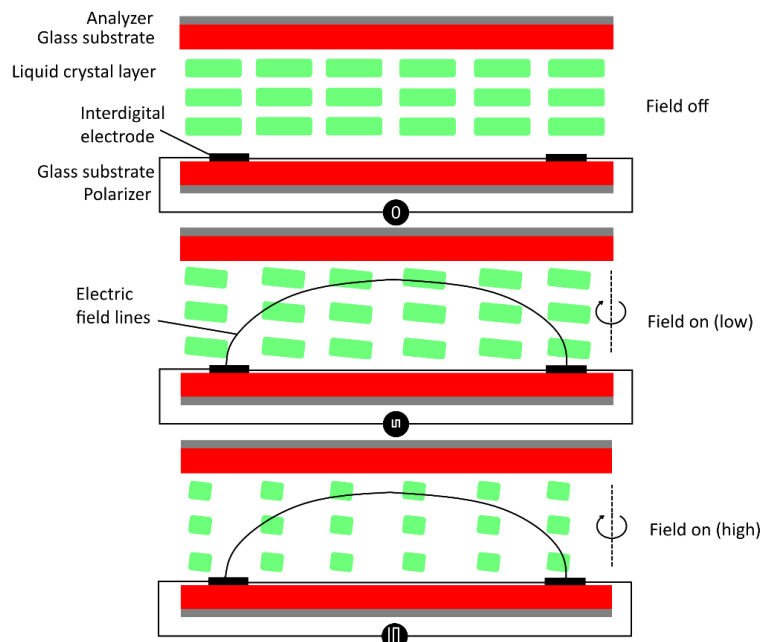


Figure 70: In-plane switching (IPS) liquid crystal. (Chen R. H., 2011, p. 377)

The optical axis of the polarizer and the analyzer are perpendicular, which sets the mode to a normally black mode and consequently it has the same advantages as the VA modes. When an electric field is applied to the liquid crystal, the molecules turn within the horizontal plane and align to the electric field. In theory the molecules should only turn in the horizontal plane, thus no unwanted mid-layer phase retardation occurs. In practice, due to the electrodes only being on one glass substrate layer, the electric field needs a strong vertical component to reach all the molecules. This however, causes the molecules to tilt rather than twist, which causes an unwanted phase retardation. Furthermore, the IPS liquid crystal layers have a relatively low transmittance and the image is not uniform in the areas of the electrodes. The concept was further developed to increase the contrast ration and wide angle image quality. Another

concept was developed by researchers of LG DISPLAYS, which is called Fringing Field Switching (FFS), where molecules are almost in-plane with a uniform transmittance. This is achieved by bringing the interdigital electrodes closer together and adjusting the length of the electrodes to decrease the extent of the vertical electric field. (Chen R. H., 2011, pp. 376-383)

The FFS mode is commonly used for mobile touchscreen devices such as smartphones and tablets, since it offers a low power consumption, a wide viewing angle, high resolution and pressure resistance. A lot of effort has been put into wide viewing angle, high resolution, low power consumption and vivid color. However, relatively slow response times and a low transmittance remain as technical challenges. Particularly televisions, computer gaming monitors and projectors have to deal with dynamic and fast-moving scenes. Thus the response time of the liquid crystal layer is a very important property. How easily the molecules turn in response to the electric field and return back to the equilibrium state when the field is turned off again defines the response time. These motions depend on the properties of the liquid crystal such as its rotational viscosity and elastic coefficient, as well as its dielectric anisotropy. Also the geometry of the liquid crystal layer such as the layer thickness and the pre-tilt angle of the molecules influence the motion significantly. Another factor which influences the response time is the energy density of the applied electric field. The molecules can react to an electric field by three different motions: bend, splay and twist as shown in Figure 71. (Chen R. H., 2011, p. 384)

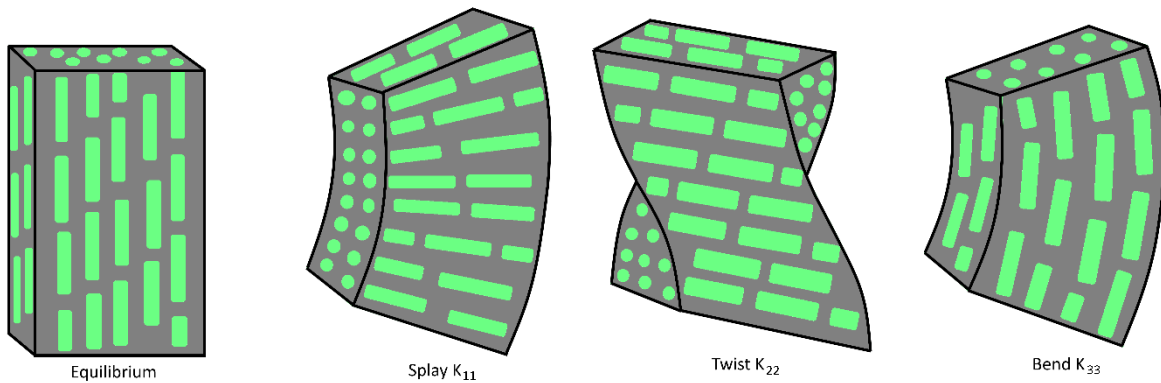


Figure 71: Elastic deformation categories of liquid crystals: Splay, twist and bend. (Chen R. H., 2011, p. 102)

When looking at the different alignment modes of the liquid crystal molecules, one can see that the Vertical Alignment mode mainly responds with bend because the molecules have a negative anisotropy and therefore tilt downwards. The positive anisotropic molecules of the Twisted Nematic mode tilt upwards and respond with splay. The molecules of the In-Plan Switching mode or the Fringing Field Switching mode twist in respond to the electric field. Each alignment mode also has to some extent elastic deformations in the other categories. A comparison of the magnitudes of the elastic coefficients shows that (Chen R. H., 2011, p. 384)

$$\begin{aligned}
 K_{33} &> K_{11} > K_{22}, \\
 \text{Bend} &> \text{Splay} > \text{Twist}, \\
 \text{VA Elasticity} &> \text{TN Elasticity} > \text{IPS Elasticity}.
 \end{aligned}$$

The free relaxation time for liquid crystals can be derived from the Ericksen-Leslie equation as (Meizi, 2010)

$$\tau_{fall} = \frac{\gamma_1 \cdot d^2}{K_{ii} \cdot \pi^2}, \quad (5.4)$$

$$\tau_{rise} = \frac{\left(\frac{\gamma_1 \cdot d^2}{K_{ii} \cdot \pi^2} \right)}{\left[\left(\frac{V}{V_{th}} \right)^2 - 1 \right]}. \quad (5.5)$$

A higher elasticity enables the liquid crystal to return faster to a lower or field-off state, so the VA mode has the fastest response to an applied electric field. The IPS was the slowest, but recent developments have made the response time faster and the use for televisions, computer monitors, smartphones and tablets possible. The TN mode is somewhere in between the VA and IPS and is the most commonly used, because of the relatively low production costs and low operating voltages. From (5.5) it can be seen that the gray-level transitions in the areas of the threshold voltage V_{th} are much slower than those at higher levels. To decrease the response time of liquid crystal panels, almost all LCD panel manufacturers have implemented some sort of overdrive system, where a voltage for a higher gray level is supplied and then lowered to the voltage of the desired gray level. The same principle can be used in the opposite direction and is called undershoot. It is also possible to use pre-tilt voltages. These technologies have decreased the response times significantly. (Chen R. H., 2011, pp. 383-394)

From (5.4) and (5.5) it can also be seen that the response time is proportional to the square of the cell gap d . A thin cell gap helps to reduce the response time effectively. However, to achieve a sufficient phase retardation with a thin cell gap, a high birefringence liquid crystal material is required. The switching time of the nematic liquid crystal is also proportional to the rotational viscosity γ_1 . A low viscosity is desirable to achieve a fast response time. (Meizi, 2010)

A state-of-the-art nematic liquid crystal device has a response time of about 5 ms (Chen Y. , 2014). Elze and Tanner investigated several different LCD displays (MVA, TN with overdrive and IPS) with regard to their response time. They noted that overdrive/undershoot and pre-tilt voltage technologies lead to a much lower response time, but also can be troublesome and lead to deviations in the response time, since they require buffering of the input signal and calculation of the displayed frame in advance. Elze and Tanner also observed a response time variability in repeated measurements. So they determined that these response lags make applications which require an instantaneous update of the panel difficult. (Elze & Tanner, 2012)

To reach a response time which is smaller than 1 ms, a new technology is necessary and as mentioned above, the Blue Phase seems to be a promising liquid crystal to decrease the response time and also save production costs. Blue Phase liquid crystals do not need molecular alignment layers and work in the normally black mode. Moreover, the transmittance is insensitive to the cell gap when in-plane electrodes are used. The response time of a Blue Phase liquid crystal depends on the pitch length of the periodical structure. The boundaries are declination lines instead of two substrates and the distance between them is approximately half of the pitch length of the twisted structure. (Yan & Wu, 2011)

$$\tau_{fall} = \frac{\gamma_1 \cdot p^2}{K_{ii} \cdot (2\pi)^2} \quad (5.6)$$

SAMSUNG introduced the first prototype of a Blue Phase liquid crystal display in 2008. The main challenges were the narrow temperature range of 2-3°C where the crystals exist, the required operating voltage, hysteresis and residual birefringence and relatively low transmittance (Rao, 2012). The temperature range was successfully increased, including room temperature, through a polymer stabilization process by Kikuchi and the temperature range was even further increased by Coles. The highest obstacle to make a technical application possible is the high operating voltage, without sacrificing the other desirable properties (Chen Y. , 2014). Chen Y. demonstrated a hysteresis-free Blue Phase liquid crystal by reducing the operating voltage, which has response times that are lower than 1 ms. The first television prototype was introduced in 2013 and MERCK estimates the earliest launch for Blue Phase liquid crystal panels in 2015 (MERCK, 2013, p. 66).

Another possibility is to use surface stabilized ferroelectric liquid crystals (SSFLC), which have two stable states and as a result possess memory properties without an active electric field which means that they are normally white and normally black. Furthermore, the fast switching (<1 ms) and wide viewing angle due to IPS mode are favorable. (Takatoh, et al., 2005, pp. 141-142)

There are three major liquid crystal suppliers: MERCK, JNC and DIC. Although the liquid crystals themselves only cause 2-3% of the manufacturing costs of a LCD panel, they are the most critical component and can also significantly lower the costs of the other display components. MERCK estimates the development of the LC technologies as illustrated in Figure 72. (MERCK, 2013, pp. 26,58,60)

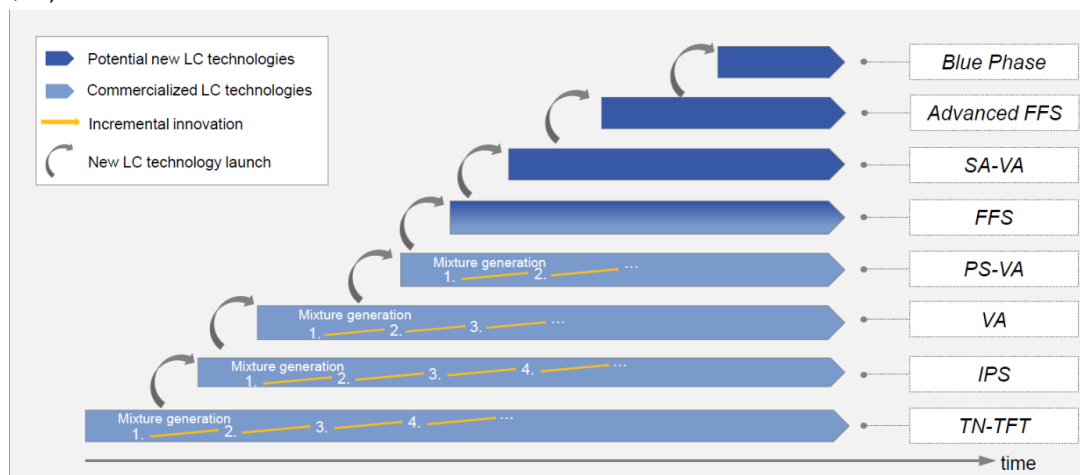


Figure 72: Innovation and differentiation in existing as well as in new liquid crystal technologies (MERCK, 2013)

Since LCDs only change the intensity of the projected image, but do not form colors, the generation of colors needs to be done in a separate step. For televisions, computer monitors, smartphones and

tablets, a backlight is used and in combination with sub-pixel primary color filters (the red, green and blue filters only transmit the wavelengths of their respective colors and absorb the other two) after the liquid crystal layer, colors are derived from the grayscale of the luminance. The drawback of using color filters however is that they absorb light which is as a consequence lost and reduces the brightness. If LEDs are used as a backlight, color filters are not necessary anymore, since the LEDs themselves can produce light in different colors. For projectors, a different approach of color generation is used because projectors are built much smaller and color filters absorb too much light. LCD projectors use three LCD panels, one for each primary color as shown in Figure 73.

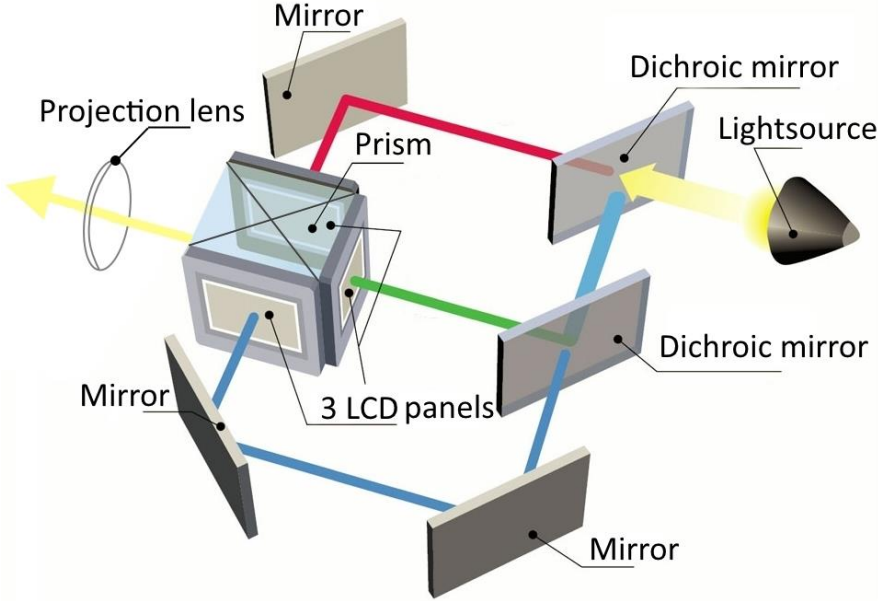


Figure 73: Structure of a 3LCD projector: The white light is split up by a system of dichroic mirrors and each color illuminates one LCD panel. A prism then recombines the colors and guides the light into a projection lens. (DELIGHT 2000, 2013)

The light of a high luminance lamp, usually high-pressure mercury lamps, is split into the primary colors (RGB) by a system of dichroic mirrors and directed to the respective LCD panel. The base glass of the mirrors is coated with a thin film that reflects only light of a specific wavelength. For all the other wavelengths the mirror is translucent, so, each LCD panel forms the image in one of the primary colors. The monochromatic images are then projected onto a dichroic prism. The dichroic prism is created by combining four triangular poles, which exactly interlay the three images to generate the scene as displayed in Figure 74.

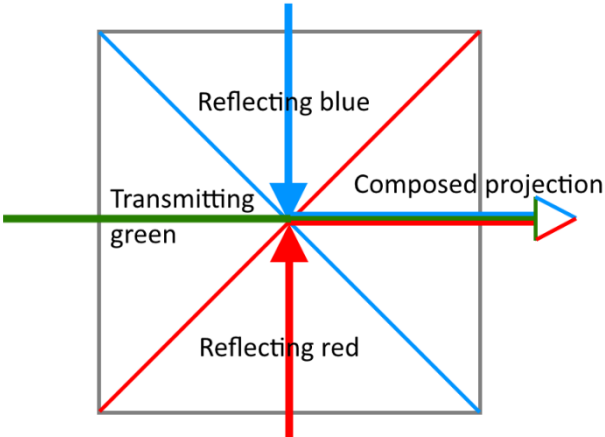


Figure 74: Dichroic prism: The blue and the red light are reflected, while the green light is transmitted. The three colors are combined to one projection.

A system of projection lenses then focuses the image onto the projection surface. Several technologies are used to increase the light output of LCD projectors, such as including an array of micro lenses in front of the LCD panels, to reduce the amount of light which is lost at the opaque regions of the panel. Commonly for such a projector setup, high temperature poly-silicon LCD panels in VA mode are used.

There are currently three manufacturers of LCD projector panels: EPSON, SONY and JVC. Because of the limitations explained above, their projector panels are limited to a response time of about 4-5 ms, which leads to a maximum possible frame rate of 200-250 Hz. Currently, the best LCD panels available for projectors can in fact reach such quick response times, as, for example, the L3C07W-9x LCD module from EPSON. The specifications of the L3C07W-9x module are listed in Table 4. (EPSON, 2014)

| | |
|------------------------------------|--|
| Photo |  |
| Technology | D10 |
| Screen size diagonal in mm | 19.25 (0.76") |
| H x V in mm | 16.32 x 10.20 |
| Pixel number H x V | 1920 x 1200 (WUXGA) |
| Pixel pitch H x V in μm | 8.5 x 8.5 |
| Outside dimension H x V x D in mm | 27.2 x 26.8 x 5x8 |
| Aspect ratio | 16:10 |
| Display colors | Monochrome |
| Micro lens array | With micro lens array |
| Liquid crystal | VA mode |

Table 4: Technical specifications of the L3C07W-9x from EPSON (EPSON, 2014)

Since they are the fastest LCD panels available, they are only included in the highest class LCD projectors, such as home cinema or professional installation projectors. Besides the very high costs, big dimensions and weight of the projector, the optics are often not suitable. There are also several LCD projectors available which can reach a native frame rate of 120 Hz. For high-speed 3D-measurement applications, such a native frame rate without any input lag is required. It is, however, very important to notice that there are often image smoothing or flickering reducing algorithms active, which insert either an interpolated frame in between the input scene or display one frame several times.

This is especially true in the television segment, where the marketing often comes up with very high frame rates, but when looking more closely at the specifications, it becomes clear that these frame rates also include interpolated frames and LED backlight flashing. In practice, when receiving a 60 Hz source input, the television flashes the LEDs to display every image several times, which leads to an advertised "frame rate" of 240 Hz. Then adding interpolated frames, "frame rates" of 480 Hz are reached and if 3D is used, this pushes the "frame rates" to 960 Hz (480 Hz for each eye). Every TV manufacturer has made up its own specification for refresh rates. For example: Samsung's Clear Motion Rate, Sony's MotionFlow, LG's TruMotion, Toshiba's ClearScan and Panasonic's Backlight Scan, to name only a few. The development of such interpolation and backlight flashing technologies may well all be justified, since it enhances the perception of fluent scenes in motion, however, these TV sets do not accept a source input of more than 60 Hz. This is due to the fact that there is simply not enough input material with higher frame rates available on the market. The TV standard in Europe is 50 Hz and in the USA 60 Hz. Gaming consoles are limited to 60 Hz and movies are still shot in 24 Hz, some in 48 Hz. So there is no trigger for developing TVs which can process higher frame rates. Only graphic cards of computers can generate an input of more than 60 Hz, and consequently the development of computer monitors with a refresh rate of 120 Hz, designed for gaming applications, can be noticed. The deciding factor here is the required bandwidth, which is influenced by the frame rate and the size of each frame and therefore defines the requirements for the used hardware and software. TV manufacturers prefer to increase the image quality (resolution and color depth) rather than the frame rate. (Bert, 2012)

Since the LCD projector manufacturers put most of their effort in satisfying the home theater market, LCD projectors with higher frame rates than 120 Hz are not available. However, almost all of the 120 Hz projectors also accept and are able to process a source input with 120 Hz. If the afore mentioned Blue Phase technology is successfully launched to the market and the demand for processing input with high frame rates is increased, then projectors which can reach native frame rates of 240 Hz or even higher might be developed. But until then 120 Hz is the limit for LCD projectors.

5.2.7 LCoS – Liquid Crystal on Silicon

The liquid crystal on silicon displays also rely on the same technical principles as LCDs to change the polarization of linear polarized incident light. But instead of being transmissive devices, such as the LCDs, LCoS are reflective devices. A layer of liquid crystals is applied on top of a reflective silicon backplane as illustrated in Figure 75. Underneath the silicon layer are the control unit and the complementary metal-oxide-semiconductors (CMOS), which is used instead of a TFT on glass. This is also favorable in several ways. The control units are not in the path of the light, CMOS are more reliable and stable than a TFT and they also allow smaller pixel pitches. Furthermore, CMOS are more efficient and the manufacturing variations are smaller. The pixels are aluminum mirrors deposited on the surface of the silicon backplane. On top of the LCoS cell a glass layer is aligned. (Jozsef & Tibor, 2006)

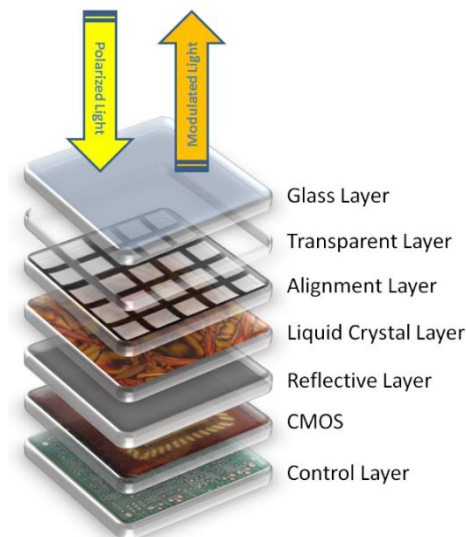


Figure 75: Structure of an LCoS cell. (Lenz & R  ther, 2009)

Since the light is reflected it passes the liquid crystal layer twice. Taking this fact into account, the caused phase retardation (5.1) by the liquid crystal layer can be written as

$$\varphi = \frac{2\pi}{\lambda} \cdot \Delta n \cdot 2d. \quad (5.7)$$

Thus, to accomplish the same phase difference of the two components of the electric field vector \vec{E} as a transmissive liquid crystal layer, the LCoS only requires half of the cell gap. From (5.4) and (5.5) it can be seen that the response time, which is dependent on the square of the cell gap, is reduced. (Zhang, Zheng, & Daping, 2014)

To reduce the cell gap further and therefore decrease the response time, the same challenges as for transmissive LCDs remain. The emerging technology of polymer stabilized blue phase liquid crystals seems also promising for LCoS devices. Liquid crystals which are commonly used for LCoS devices are nematic liquid crystals in VA mode. (Yuan, Fenglin, & Wu, 2013)

As explained in 5.2.6 the VA mode requires a negative anisotropy $\Delta\epsilon < 0$. The VA operates in a normally black state and has as a result a very good contrast.

Advantages of the LCoS technology are the lower response times (<2 ms) due to the smaller cell gap and the higher possible resolution because of the smaller pixel pitches. With the emerging development of the blue phase liquid crystal panels, the response time can be further reduced (<1 ms). (Chen Y. , 2014)

The commonly used structure of an LCoS projector is a 3LCoS panel configuration, one panel for each primary color and is shown in Figure 76.

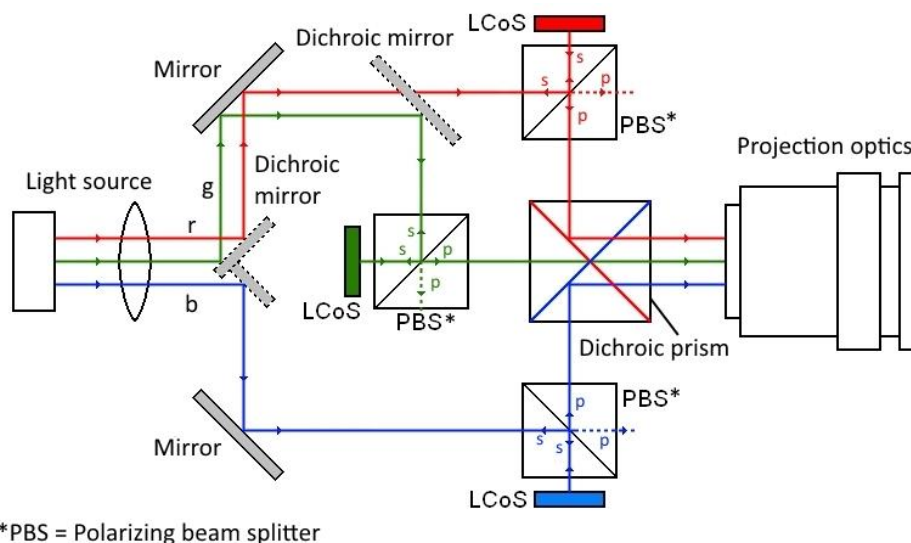


Figure 76: Structure of an LCoS projector: The white light is split up into the primary colors by a system of dichroic mirrors. The three light beams then enter polarizing beam splitters (PBS) which let p-polarized beams pass and reflect s-polarized beams. When the polarization of the light is modulated by the LCoS chip from s-polarization to p-polarization, it passes the PBS and reaches a dichroic prism, where the RGB images are overlaid and guided to the projection optics. Otherwise the light is reflected and stays in the optical system. (Reichl, 2006)

A high brightness light source, usually a Xenon arc lamp, supplies the projector with light. The primary colors are generated by dichroic mirrors and guided to the three LCoS panels. A polarizing beam splitter (PBS) divides the unpolarized monochromatic beams into two orthogonal linearly polarized beams. The p-waves are polarized in the plane of the incident unpolarized beam and the s-waves are polarized orthogonal to that plane. The p-waves can pass the PBS without a reflection and leave the optical system, the s-waves get reflected onto the LCoS panel and depending on the operation state of the LCoS, a change of the polarization happens. In the off-state no change of the polarization occurs, since the LCoS are normally black, and therefore the s-waves get reflected again by the PBS and do not reach the dichroic prism. In the on-state, the LCoS changes the polarization state of the s-waves exactly 90°, and as a result they become p-waves, which can pass the PBS without reflection and reach the dichroic prism. In the dichroic prism the three monochromatic images are interlaid and reflected into the projection optics which focus the image onto a projection surface. The PBS is a very critical component and often the optical properties can vary considerably, which can cause a significant light leakage. As a consequence JVC uses a wire-grid polarizer, which is an inorganic reflective polarized light plate made of aluminum ribs on a glass substrate. The wire grid minimizes the leakage of light to the lens when the image is black. The Wire Grid is shown in Figure 77. The unpolarized light is incident on the wire grid with an angle of 45° and the light transmitted by the wire grid and incident on the LCoS is thus p-polarized. When the LCoS rotates the polarization state of the p-polarized light to an s-polarized light, the light beam is reflected by the wire grid into to projector lens.

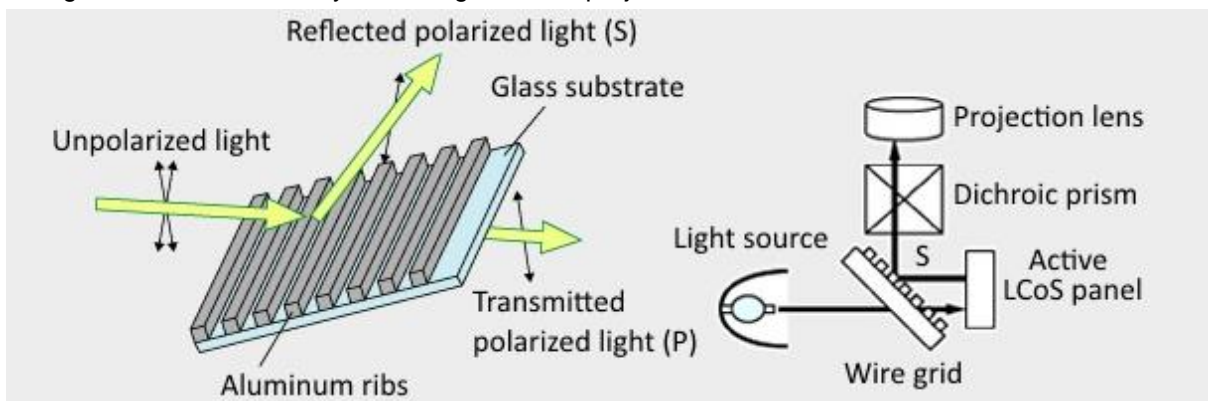


Figure 77: Wire Grid: The unpolarized light is incident on the wire grid with an angle of 45° and the light transmitted by the wire grid and incident on the LCoS is p-polarized (JVC, 2007)

There do also exist configurations with 3LCoS panels and different prisms and optics, two LCoS panels (Murat, et al., 2008) or one LCoS panel, the latter one being used for pico-projectors in combination with three LEDs for the primary colors, which are designed for smartphones and handheld gaming consoles. These pico-projectors usually use ferroelectric liquid crystal panels, but the brightness of such pico-projectors is rather low (~ 100 Lm), and the optics limit the possible projection distance.

There are currently three main manufacturers of LCoS projector panels, which are SONY with Silicon X-tal Crystal Reflective Display (SXR), JVC with Direct-Drive Image Light Amplification (D-ILA) technology and CANON. These panels are only integrated in large venue projectors for museums, planetariums, simulators, digital theaters, production studios and home theaters. Furthermore, the projectors have interpolation algorithms, which hinder the projector to natively project the source input. Although an LCoS panel is able to achieve very low response times, the priorities of the manufactures of LCoS projectors are to increase the resolution (4096 x 2160 pixels) and provide an excellent image quality (high contrast, high pixel density, little artefacts and fluent motion) rather than increasing the frame rate. Similar to the LCD projectors, the available input material on the market defines the development of LCoS projectors. Hence, they use the bandwidth, which is defined by the frame rate and the size of each frame, for a higher resolution and a color depth instead of a higher frame rate. The hardware and software of LCoS projectors is consequently not designed to project an image at high speeds. The LCoS is, however, a promising technology, and further developments in the field of liquid crystals will show if it will enter the low-cost consumer projector market. With the currently available LCoS projectors, however, a high-speed 3D-measurement application is not possible.

5.2.8 DLP – Digital Light Processing

Digital light processing (DLP) uses an electro-mechanical device, called digital micro mirror device (DMD), which is also a fast reflective opto-mechanical device which can precisely modulate incident light. The DMD is built up of micro mirrors made of aluminum, which are aligned in a matrix, with each mirror representing one pixel of the image. Each micro mirror can be tilted (± 12 deg) back and forth. By convention, the positive tilt is toward the light source and is thus referred to as the “on” state. The negative tilt is consequently away from the light source and is defined as the “off” state. Figure 78 shows two pixels, one in the “on” state (logical 1) and one in the “off” state (logical 0) as well as the structure. (TI, 2013)

These are the only two operational states. The flat state (0 deg) only occurs if the mirrors are not energized. (TI, 2010)

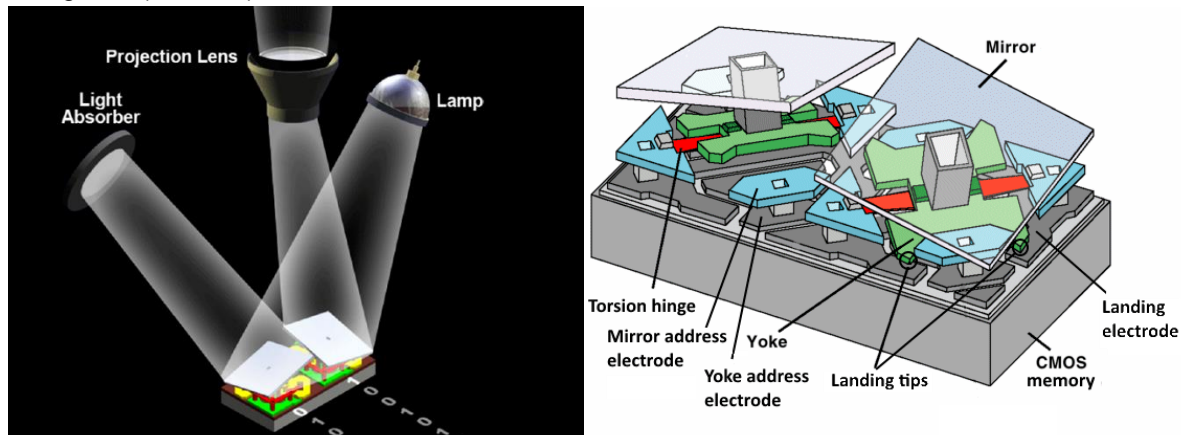


Figure 78: Digital light processing principle (left) (TI, 2013) and structure of a digital micro mirror device (right) (Kuhlmann & Paul, 2002)

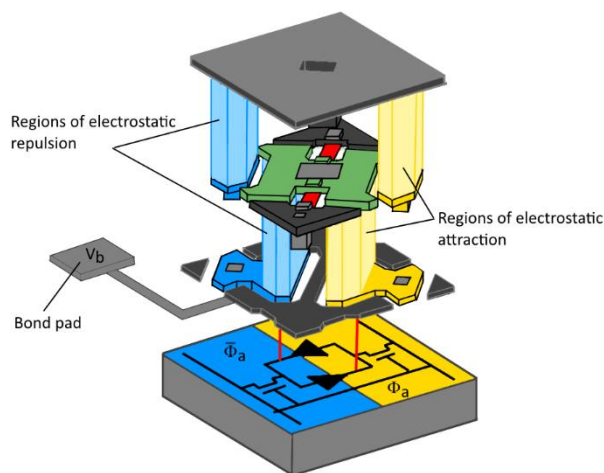


Figure 79: DMD electrical schematic: The regions of electrostatic attraction are highlighted (Hornbeck, 2002)

The mirror is attached to an underlying yoke. The yoke is connected to two torsion hinges, which are also fixed at the hinge support posts and can be twisted in the middle. Two pairs of address electrodes, for the yoke and the mirror, control the tilt of the mirror by electrostatic attraction as shown in Figure 79. This attraction induces a torque which works against the elastic torsion hinges and causes the mirror and yoke to tilt together until the landing tip of the yoke hits a mechanical stop. Due to the mechanical stopping mechanism, the tilting angle is precisely set and limited to $+12$ deg and -12 deg. The electrodes of the mirror and the yoke are connected to a bias bus. The bias bus interconnects them to a bond pad at the chip, which is supplied by an off-chip driver. (Hornbeck, 2002)

Below each micro mirror is a memory cell formed from dual CMOS memory elements. The state of the two memory elements is always complimentary, which means that if one element is logical 1 the other is logical 0. The DMD is operating as a bistable device, which means that it has two equilibriums, where by definition the potential energy is at a minimum. At which tilting angles these equilibrium positions are situated, depends on the difference of the linear hinge restoring torque and a nonlinear counteracting electrostatic torque induced by a bias V_b at the landing electrode. If the two torques cancel each other out, then an equilibrium is reached. Thus, a certain bias V_b can be chosen which puts the DMD into a bistable mode. Figure 80 shows the potential energy as a function of the tilting angle and bias when no address voltage is applied. Note that the bias only determines the operational mode of the DMD and that the address voltage causes the tilting. With an increased bias, the DMD changes its operational mode from monostable (with the equilibrium being at the 0 deg flat state), to tristable (with three equilibriums at 0 deg, $+12$ deg and -12 deg) and finally to bistable (with two equilibriums at -12 deg and $+12$ deg). As illustrated in the bottom diagram, a small address voltage Φ_a is already sufficient enough to switch the mirror from 0 to $+12$ deg. Once a mirror

has reached the maximum tilt angle, the mirror stays put even if the address voltage Φ_a is removed again. This reduces the address voltage requirements and enables the use of CMOS. This was the breakthrough for the DMD technology. (Motamedi, 2004, pp. 403-407)

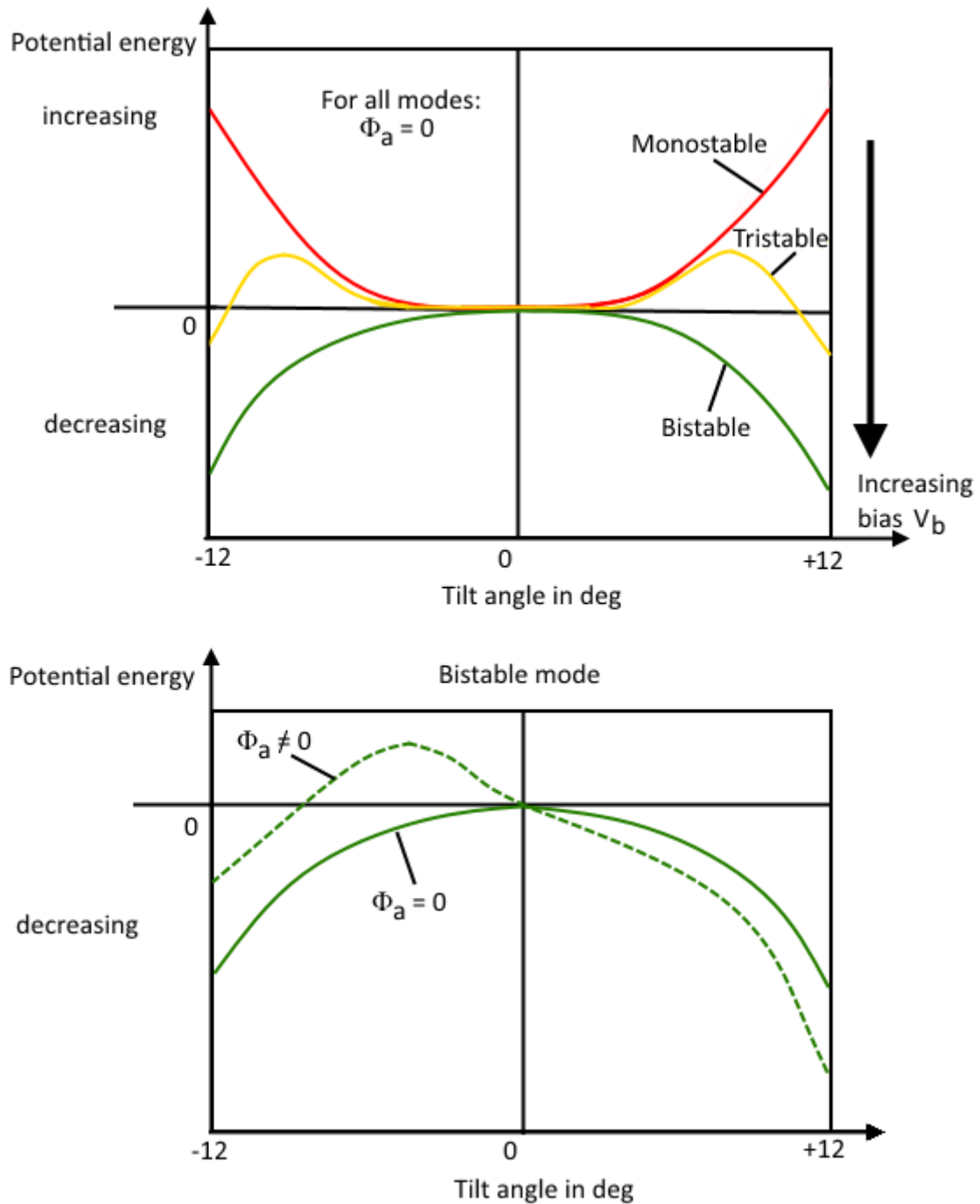


Figure 80: Monostable, bistable and tristable mode of a DMD in relation to the bias voltage V_b (top) and effect of the applied address voltage Φ_a for the bistable mode (bottom). (Motamedi, 2004, p. 406)

The fact that the address voltage can be turned off once the mirror has reached the maximum tilt angle, also allows the CMOS memory to be updated, while the DMD is operating. Consequently the memory state and the micro mirror state are not directly linked. This principle allows the memory state of groups of pixels to be pre-loaded and then, by applying a mirror clocking pulses (MCP), update the micro mirror state simultaneously. This MCP is necessary to overcome the van der Waals forces (surface tension). In the latest architecture of the DMD, the yoke lands on spring tips, which help to overcome the van der Waals forces. The MCP releases the micro mirror for a short time which then lands again based on the state of the CMOS memory. The DMD memory is loaded in rows, which means that in order to change one pixel in a row, the entire row has to be loaded. The DMD array is divided into several blocks and a MCP is always issued to a whole block. The pixels in that block whose memory state has changed move

to the opposite tilt angle, and those whose memory state did not change will remain at the same tilt angle. There are different MCP modes: single block, dual block, quad block, global. (TI, 2013)

The pixel intensity is set by using a binary pulse width modulation. This requires that the time of the video field is split up into bit times which are binary intervals. Hence each bit represents a time duration for light to be on (logical 1) or off (logical 0). During each bit time the memory array is updated for the next bit time. As soon as the memory array is refreshed, all mirrors of the array are released at once and move according to their new address states. This tilting can be done very fast, which enables the possibility to produce grayscale images by rapidly switching the mirror on and off. The DMD uses 8-bit words, representing 2^8 or 256 possible gray levels. (Hornbeck, 2002)

The address sequence, as displayed in Figure 81, is performed once each bit time and can be summarized as follows

1. Reset all mirrors in the DMD array
2. Turn bias off to allow mirrors to begin the tilt to flat state (0 deg)
3. Turn bias back on to enable mirrors to tilt to the addressed states in the memory (± 12 deg)
4. Keep bias on to latch the mirrors, so they will not respond to a new address state
5. Address SRAM array under the mirrors, row by row

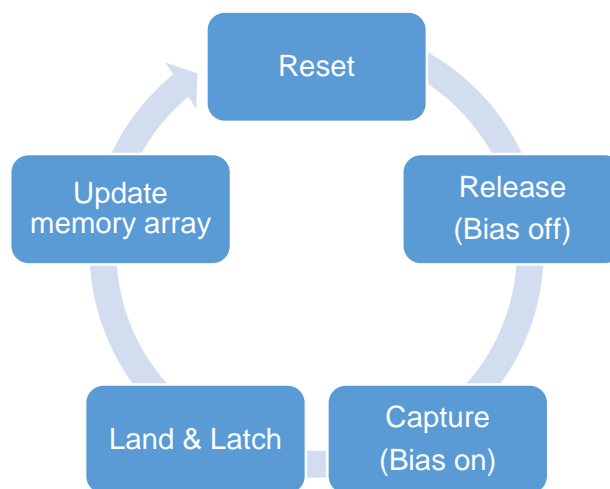


Figure 81: Address and reset sequence of the DMD (Hornbeck, 2002)

The structure of a DLP projector can either be a 3DLP chip configuration or the most commonly used 1DLP chip configuration. Since a DMD does not produce colors by itself, the color sequence has to be produced in another way. The colors from a color filter are obtained by the spatial averaging of the different intensities of the primary colors by the eye. In principle then, the colors could also be produced by time averaging of a sequence of different intensity primary colors. This is the so-called field sequential color (FSC) scheme. The principle was already demonstrated by Maxwell, who showed that different tints on a rotating disc become indistinguishable if the rotation is rapid enough (Maxwell, 1855). This principle is used in most of the 1DLP chip projectors using a so-called color wheel, which basically combines the different color filters onto one device which is shown in Figure 82.

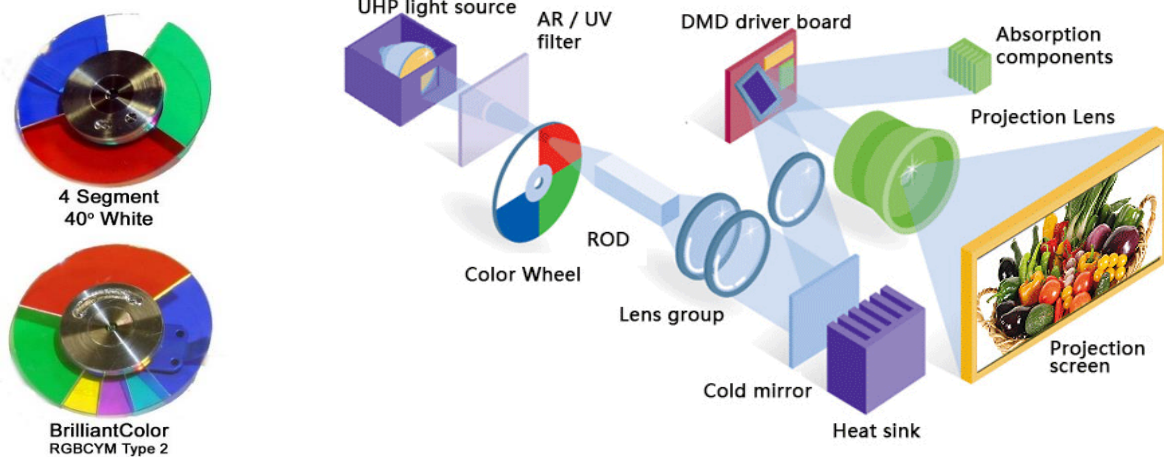


Figure 82: Different color wheels for DLP projectors (left) (Tsolis, 2009) and the structure of a 1DLP projector (right) (SITER, 2014)

The DMD, the light source and the color wheel have to be synchronized with each other, and, moreover, the FSC scheme requires image processing and frame memory. For example, if the refresh rate of the 8-bit image (256 gray levels) should be 60 Hz, then one primary color subfield of the color wheel (RGB) spins with 180 Hz. The maximum allowed switching time for the DMD, without any safety margin, for an 8-bit grayscale can then be calculated as

$$t_{S_{max}} = \frac{1}{180 \cdot 255} \cdot 10^6 = 21.8 \mu s. \quad (5.8)$$

The DMD technology is able to switch significantly faster than $t_{S_{max}}$, which enables the use of the FSC scheme. There are different types of color wheels which can be used, as, for example, shown in Figure 82 on the left, with a white sector to increase the brightness or with additional colors (magenta, yellow and cyan) to increase the contrast. The use of a color wheel has, however, also certain drawbacks. As it is a rotating mechanical device, the degree of wear and tear on the bearing of the color wheel influences the lifetime of the projector. Moreover, since only the preferred wavelength passes the color wheel segment, light is lost which reduces the brightness. Hence, the high-end projectors use a 3DLP configuration as shown in Figure 83. The advantages are that very little light is lost and the color wheel is not required anymore. Challenging is, however, the exact overlaying of the single pixels, which requires precise optical elements.

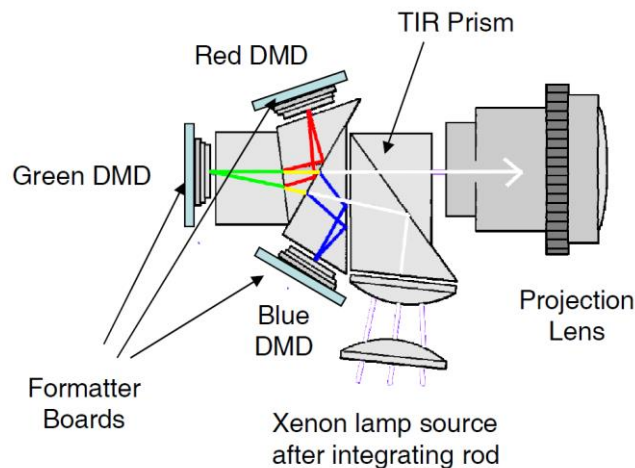


Figure 83: Structure of a 3DLP projector: The light of a xenon lamp is incident on a TIR prism and split up by a system of dichroic prisms. Each of the three DLP chips reflects one of the primary colors which are then recombined by the prism systems and guided to the projection lens. Very precise optical elements and positioning is required.

There are two micro mirror arrangements available for the DMD array. An orthogonal arrangement and a diamond arrangement, in which the micro mirrors are rotated 45°, both shown in Figure 84. The diamond alignment is used for pico projectors because the light source, the DMD and the projection lens are in one horizontal plane. This enables the dimensions of the projector to be smaller. A drawback, however, is that the vertical lines are not straight, but have a jagged structure. The orthogonal alignment is used for the vast majority of the home theater and cinema projectors, since the dimensions of the projector are not the critical design factor.

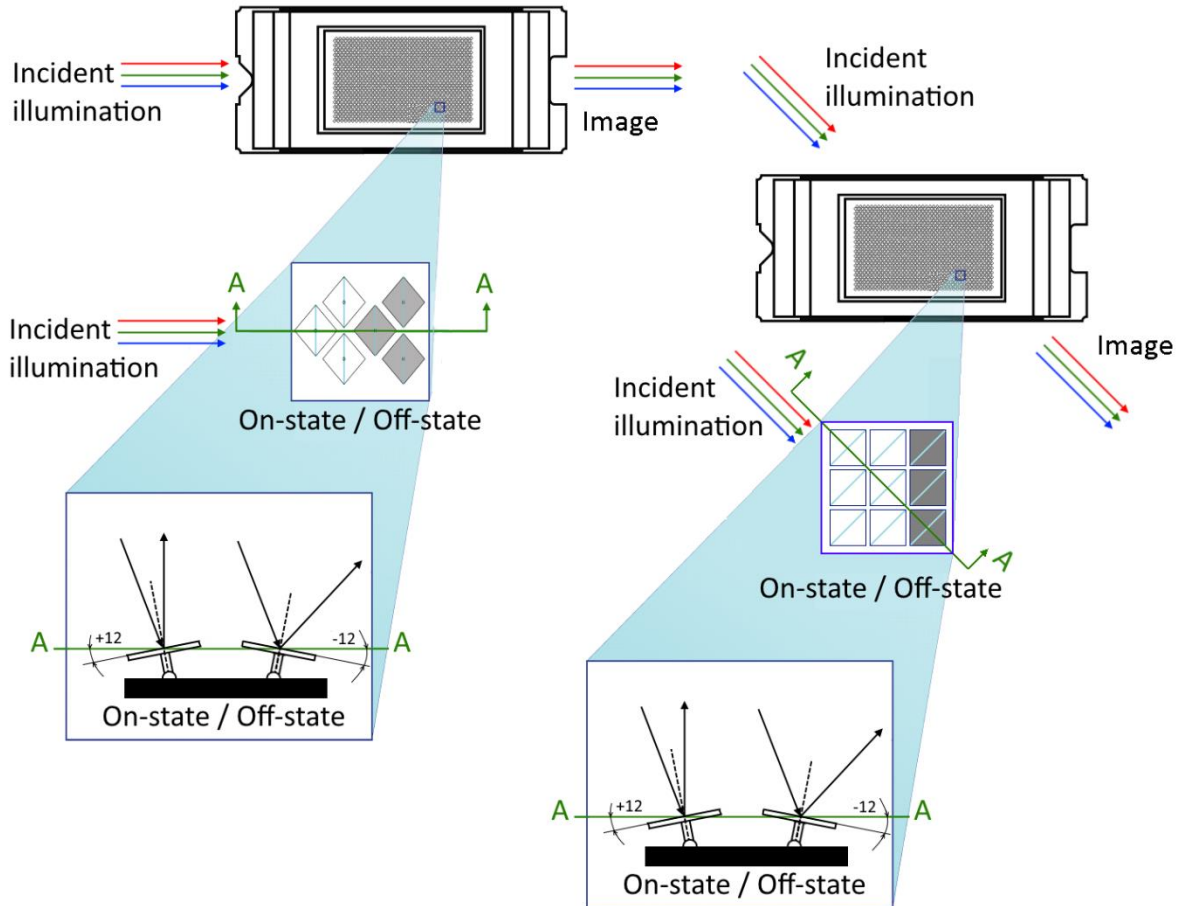


Figure 84: DMD micro mirror alignment. Diamond (left) (TI, 2013) and orthogonal (right) (TI, 2013)

The DMD chips are solely manufactured by TEXAS INSTRUMENTS (TI) and are available in a wide variety of resolutions from 320 x 240 up to 4096 x 2160, which enables the DLP technology to be widely spread over the entire projector market from the pico projectors to the cinema projectors. The different generations of DMDs reduced the pitch between the mirrors and increased the contrast and are called Dark Chips 2 (DC2), 3 (DC3 and DC3+) and 4 (DC4). These generations are used in different types of projectors by lots of manufacturers, starting with the DC2 in low-budget projectors, to DC3 in the home theater projectors, to DC4 in the high-end projectors for cinemas, large venues, museums, simulators and planetariums. Apart from that, TI also offers several DLP Discovery platforms for special applications, which enable the user to control every single micro mirror directly. These platforms include a DMD, a controller and a circuit board and are also used for applications which go beyond the simple projection of an image such as wavelength selection for spectrometry, digital exposure of photopolymer or resin in the manufacturing process, 3D-machine vision, etc. TI does not build projectors by themselves, but they offer evaluation modules for their DLP technology, which include a light source and projection optics manufactured by external companies. These advanced light control chipsets are able to fully use the very fast switching mechanism of the DMD, which enables frame rates for 8-bit images of 120 Hz to 1900 Hz. For special applications, very often monochromatic light is used, which makes the generation of different colors obsolete and frame rates for 1-bit images of up to several kHz are possible.

The consumer projectors, however, are also limited to 120 Hz, which is due to the same reasons as already described above for LCD and LCoS projectors. For the consumer market and the large venue applications, image quality and resolution is more important than the frame rate. Thus, the bandwidth is preferably used to increase the frame size instead of the frame rate. Also, the software and hardware,

such as the color wheel and especially the controller, are not designed to process an input with frame rates that are higher than 120 Hz.

Since LEDs and laser diodes become more powerful and efficient, a configuration with three high power LEDs (RGB), three laser diodes (RGB), one blue laser diode with a phosphor wheel or a hybrid technology, utilizing both LEDs and laser diodes, is possible. These configurations do not only erase the necessity for a color wheel and several optical elements but also significantly increase the lifetime of the light source. Figure 86 shows these configurations, which are already used in several projectors. The hybrid configuration uses a red and a blue LED and one blue laser, part of which is split up to illuminate a rotating phosphor wheel, to change the wavelength of the laser light to green. The reason why these configurations are not used in all 1DLP projectors is simply the fact that in order to reach a similar light output, a color wheel in combination with a xenon lamp is still cheaper to manufacture. For the high-end projectors in cinemas with the 3DLP configurations, however, lasers are already used. The 3 LED configuration is used in the pico projectors because they significantly reduce the dimensions of the projector. Theoretically LEDs and laser diodes, or a hybrid configuration, can be used with all light modulators (LCD, LCoS or DMD).⁸ Currently most LED projectors use the DLP technology, while only some use the LCoS or LCD technology. Laser diodes gain increasing market share, since the developments in recent years increased the available wavelengths and mass production reduced the costs significantly.

Laser diodes have several advantages, such as a longer lifetime, better contrast, image uniformity, no image flicker and higher sharpness of the image. Furthermore, they are more efficient and the operational and maintenance costs are significantly lower in comparison to a xenon lamp. However the image quality depends strongly on the speckles of the laser beam. Speckles are an interference pattern that occurs when coherent light is scattered off an optically rough surface, such as a screen and is most visible on uniform, bright elements of the projected image. Additionally, the acquisition costs for laser-based projectors are usually higher, and in several countries there exist very strict regulations regarding the use of lasers. The IEC, which sets the standards for lasers and their use, has recently changed the categorization of laser illuminated projectors from a laser standard DIN EN 60825-1:2014 to the lamp standard IEC 62471:2006. This is all well justified, since the light emitted from the laser illuminated projectors is processed in such a way that it loses the hazardous qualities of typical lasers which are used in direct projections. However, the regulations in several countries, including the USA, still are an obstacle (LIPA, 2015).

So increasing effort is put into changing these regulations and developing laser diodes to reduce the speckles and lower the price.

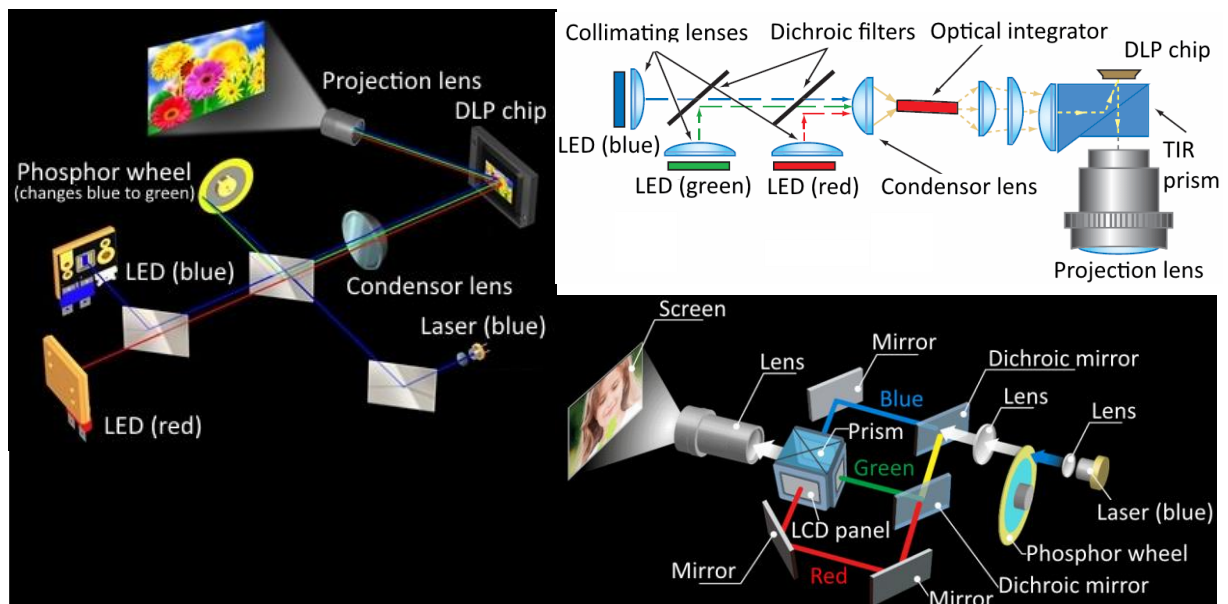


Figure 86: Configuration for LED-based (top right) (TI, 2015), Laser-based (bottom right) (Chinnock, 2013) and Hybrid projectors (left) (Morrison, 2013)

⁸ Very often projectors which use LEDs are advertised as LED projectors, and those which use laser diodes are advertised as laser projectors. This is somewhat misleading, since only the light source and not the light modulator is specified.

5.2.9 Laser projector

Figure 87 shows the basic layout of a laser projector which uses a laser beam as light source. It consists of two laser diodes, one for blue and one for red, and a second harmonic generation (SHG) laser. Dichroic elements combine the light of the three lasers and generate a single white beam. The white beam is then reflected by a beam splitter or mirror onto a biaxial scanning mirror which scans the beam in a predefined raster. (Freeman, Champion, & Madhavan, 2009, p. 30)

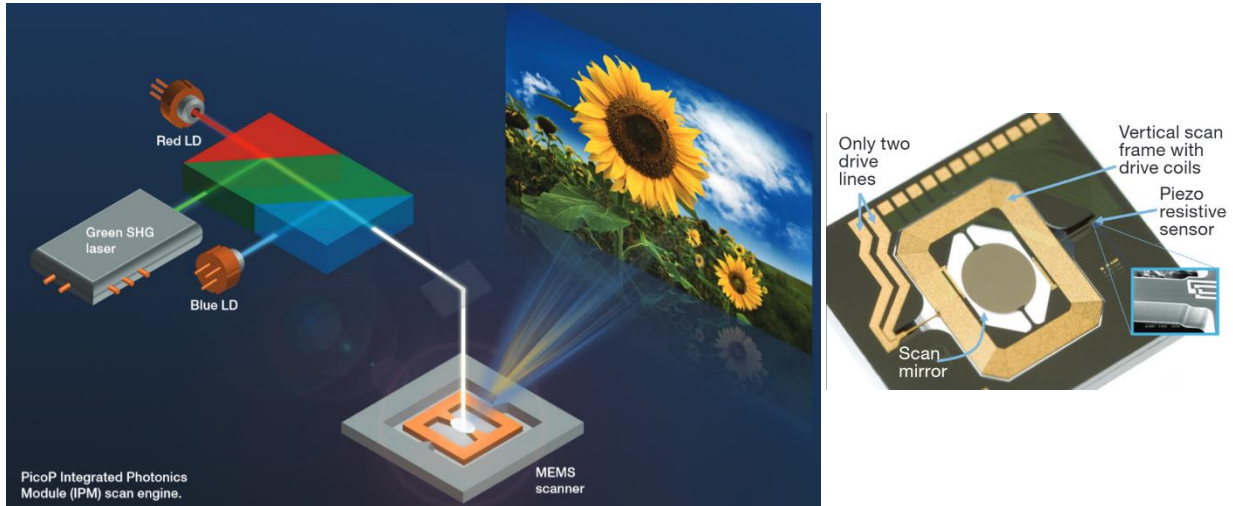


Figure 87: Principle of a laser projector and a MEMS scanner (Freeman, Champion, & Madhavan, 2009)

The modulation of the lasers is synchronized with the position of the scanned beam which allows to create the projected image with the desired color for each pixel. The contrast is theoretically infinite because the lasers are turned off completely for black pixels. As can be seen in Figure 87 there is no projection optics implemented in the design of the projector. This is not necessary because the rate of expansion of the single beam is electronically adjusted to the rate that the scanned image size grows. This principle allows infinite focus which generates a focused image on any surface. This is achieved by dividing the task of the projection. A low numerical aperture single-pixel beam sets the focus and a 2D-scanner generates the image. This 2D-scanner has the function of fast projection optics. However, since the opto-mechanical parts are simplified, the task to generate the desired image with the correct colors and uniform brightness is shifted to the electronics. This requires the possibility to control the laser beams at pixel accuracy. (Freeman, Champion, & Madhavan, 2009, pp. 30-32)

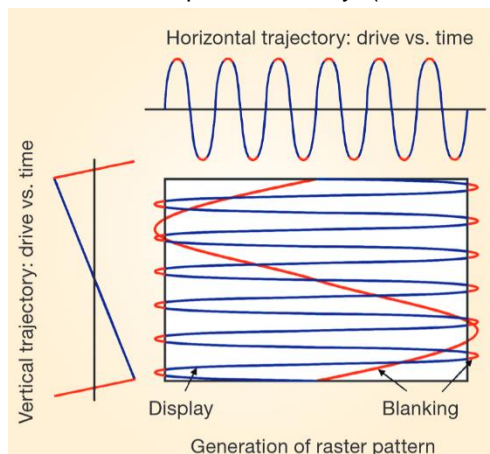


Figure 88: Bidirectional raster scan (Freeman, Champion, & Madhavan, 2009)

The generation of the raster pattern is illustrated in Figure 88. The horizontal axis is scanned at its resonant frequency, which reduces the required power to drive the scan mirror. The scan velocity varies sinusoidal with its position. The scanner draws the image in both directions as it moves the beam back and forth. This scan motion reduces the blanking intervals and results in a brighter projection. The vertical scan direction follows a saw-tooth path which keeps the velocity constant from top to bottom. When the beam reaches the bottom of the image, it returns to the top to start with a new frame. The synchronization of the vertical and horizontal motions is also managed by a controller. The advantage of shifting the image generation from the opto-mechanical devices to the electronics, is that the alignment of the red, green and blue pixels as well as the compensation of chromatic aberration can be performed electronically. (Freeman, Champion, & Madhavan, 2009, pp. 32-33)

This principle is used also for large venue direct projections, where the projection surface is not flat such as in planetariums or flight simulators. There are also some pico-projectors available, which use this technology, such as the PicoP from MICROVISION. The frame rate of the PicoP is typically 60 Hz for an 848x480 image (Freeman, Champion, & Madhavan, 2009, p. 34). However, the brightness is rather low, so, none of these projectors is currently suitable for high-speed 3D-measurement applications.

6 Choosing the projection unit

The requirements of the projection unit defined by KNAPP are as follows:

- Minimum frame rate: 160 Hz (maximum capture rate of used cameras)
- Fast and easy changing of patterns
- Flexible montage of projector
- Includes trigger for cameras
- Includes controller of projector
- Minimum luminous flux : 500 Lm (IEC) (for white light)
- Almost distortion free image (< 1%, precise optics)
- Working distance: 1600 mm
- Illuminated area at working distance: 600 mm x 400 mm
 - The necessary throw ratio of the optics can then be calculated as

$$\text{Throw ratio} = \frac{\text{Working distance}}{\text{Image width}} = \frac{1600}{600} = 2.67 \quad (6.1)$$

- Minimum pattern resolution: 640 pixel x 480 pixel (resolution of the used cameras)

Neither movie projectors nor CRT projectors are suitable for high speed 3D-measurement applications and consequently are not considered as an option for KNAPP. These technologies do not reach the required frame rates and, additionally, are at the end of their lifetime.

The prototypes of Wissmann and FRAUNHOFER IOF are both very promising approaches to high speed projection, but neither of them is currently suitable for the specifications that KNAPP has. Further development of these two concepts would be necessary.

In state-of-the-art LCD projectors VA-mode liquid crystals are used and some 3D projectors operate at frame rates of up to 240 Hz. However, these projectors use internally interpolated frames or black frames which are inserted in between the native input. They sometimes accept a native input of 120 Hz at reduced resolution (especially projectors designed for video gaming or 3D-projection), but most of these projectors can only process input signals with a frame rate of 60 Hz. The reason for the lack of projectors which can process higher frame rates is that there is barely a demand to develop such projectors. The standard input frame rates are 24 Hz, 50 Hz or 60 Hz and only some graphic cards are able to provide higher frame rates. Thus, the focus of LCD projector manufacturers is on increasing the image quality by using the bandwidth for a higher resolution and applying interpolation algorithms to enhance the source input. There are three major manufacturers of LCD panels for projectors, which are EPSON, SONY and JVC. Requests for evaluation modules and single panels were not successful because they are only available to customers who plan to purchase large quantities. The source code of the firmware of the projector is also not available, which makes modifications to the software difficult. Unless further developments of the liquid crystals will be carried out or the demand to process input sources with higher frame rates from the media sector will increase, the use of LCD projectors for high speed structured light illumination is not possible.

LCoS panels are mainly manufactured by SONY, JVC and CANON, all of which use them in high-end cinema projectors. These projectors are designed to project an image with a very high resolution onto a distant screen, and as a result, the priorities for the development are to increase the resolution and provide a good image quality for the viewer. This explains why the projectors can only process input signals which have a maximum frame rate of 60 Hz. There are also some pico-projectors for smartphones and handheld gaming consoles on the market, which use ferroelectric liquid crystals in combination with LEDs, but they are not designed to deliver a high brightness or resolution and are also not able to process high frame rate inputs. Similar to the LCD projectors, the demand for processing higher frame rates needs to increase before LCoS projectors will be developed further. As of 2015, they are not suitable for high speed structured light illumination.

The DMD chips are all manufactured by TI, who also offer the corresponding controllers which enable the DMD chips to reach very high switching speeds. TI do, however, not manufacturer projectors themselves. TI sell the chips and controllers to many projector manufacturers, such as CASIO, ACER, PANASONIC or BENQ, only to name a few. Some of those companies use their own controllers and electronics to operate the DMD. However, since the consumer projectors are designed for the home theater market, the same limitations as for the LCD and LCoS projectors apply. There is barely any input available on the market which exceeds frame rates of 120 Hz, so, the development for processing higher

frame rates is not triggered. There are several DLP projectors on the market which can process a 120 Hz input signal at reduced resolution, either over the HDMI (High Definition Multimedia Interface), DVI (Digital Visual Interface) or DisplayPort. Besides these consumer products, several evaluation modules for the DLP technology are available which consist of the DMD chip, a controller and a circuit board. An overview of the chipsets is provided in Table 5. The chipsets can be ordered as evaluation modules, regardless of the planned quantities and some already come with an optical engine, consisting of a light source and optics, which are manufactured by external companies.

| DMD Chipsets Video and Data Display | | | | | | | |
|-------------------------------------|------------|-------------|-------------|-------------|--------------------------|-------------------------------------|------------------------|
| Chipset | Controller | 8-bit in Hz | 1-bit in Hz | Resolution | Micro mirror orientation | Micro mirror pitch in μm | Array diagonal in inch |
| DLP2010 | DLPC3430 | 120 | N/A | 854 x 480 | Orthogonal | 5.4 | 0.22" |
| DLP3000 | DLPC2607 | 120 | N/A | 854 x 480 | Diamond | 7.6 | 0.30" |
| DLP3010 | DLPC3433 | 120 | N/A | 1280 x 720 | Orthogonal | 5.4 | 0.30" |
| DLP4500 | DLPC6401 | 120 | N/A | 1280 x 800 | Diamond | 7.6 | 0.45" |
| DLP4710 | DLPC3439 | 120 | N/A | 1920 x 1080 | Orthogonal | 5.4 | 0.47" |
| DMD Chipset Advanced Light Control | | | | | | | |
| DLP3000 | DLPC300 | 120 | 4000 | 608 x 684 | Diamond | 7.6 | 0.30" |
| DLP4500 | DLPC350 | 120 | 4225 | 912 x 1140 | Diamond | 7.6 | 0.45" |
| DLP5500 | DLPC200 | 700 | 5000 | 1024 x 768 | Orthogonal | 10.8 | 0.55" |
| DLP6500 | DLPC900 | 250 | 9500 | 1920 x 1080 | Orthogonal | 7.6 | 0.65" |
| DLP7000 | DLPC410 | 1900 | 32552 | 1024 x 768 | Orthogonal | 13.6 | 0.70" |
| DLP9000 | DLPC900 | 250 | 9500 | 2560 x 1600 | Orthogonal | 7.6 | 0.90" |
| DLP9500 | DLPC410 | 1900 | 23148 | 1920 x 1080 | Orthogonal | 10.8 | 0.95" |

Table 5: DMD Chipsets by TI

In the upper section of Table 5 the evaluation modules for pico-projectors are listed, all of which are able to operate at 120 Hz, when the input is stored on the flash memory. They are, however, not able to process signals with a frame rate which exceeds 60 Hz over HDMI and it is not possible to change the images which are stored on the flash memory. In the lower section of Table 5 the Advanced Light Control modules are listed. These come with a software bundle from TI, which allows controlling each micro mirror of the DMD array individually. Furthermore, a flash memory on the circuit board allows the storage of pattern sequences as bmp-files and several input/output trigger enable the synchronization with other components, such as cameras. These modules can reach frame rates of up to 1900 Hz for 8-bit and 32552 Hz for 1-bit images, providing the possibility to be used for very high speed 3D-measurement applications.

Currently, laser projectors are only available as pico-projectors or large venue projectors for planetariums or flight simulators. The lasers of the pico-projectors are not powerful enough and the frame rate is also limited to 60 Hz. For that reason, laser projectors are, as of 2015, not suitable for high speed 3D-measurement applications.

To compare the different projectors a value benefit analysis is used. The requirements are weighted according to the importance and each projector is evaluated. The values for each requirement can be between one and five, one being the worst and five being the best score possible. Including the weighting of the values, a maximum overall score of five is attainable. In a first step only the projectors which reach a frame rate of 120 Hz and operate continuously are evaluated. This eliminates slides projectors, movie projectors, CRT projectors, laser projectors and the projector evaluation modules from TI. There are a lot of 3D projectors available on the market, which use 3D sequential frame projection to project a scene for the left eye and for the right eye alternating with 120 Hz (each eye 60 Hz). These projectors can process a 3D input signal with 120 Hz from a PC's graphics card, but very often the firmware does not allow processing of a 2D signal with 120 Hz. There are, however, workarounds which might or might not work, depending on the projector. Table 6 shows a list of projectors which are suitable for the application of KNAPP and can process a 2D signal with 120 Hz. As discussed above, the necessary throw ratio is 2.67:1. The projectors with a lower throw ratio need an adjustment to the source image to reach the desired image width.

Example:

With a throw ratio of 2.1:1 and operating the projector at a resolution of 1280 x 800 pixels, the required source image must be built up of an “active” area of 1024 x 768 pixels containing the pattern, surrounded by a “non-active” area, to have the correct width on the projection surface.

A list of current consumer projectors which are able to process an input signal of 120 Hz, have suitable optics and are inside the budget that KNAPP provides, is presented in Table 6:

| Manufacturer | Model | Technology | Resolution in pixel | Throw ratio | Price in € | 120Hz@ resolution |
|--------------|-----------|-------------|---------------------|-------------|------------|---|
| BARCO | PFWX-51B | 1xDLP 0.65” | 1280x800 | 2.89:1 | 2500€ | 800 x 600 1024 x 768 1280 x 720 1280 x 800 |
| BENQ | W7500 | 1xDLP 0.65” | 1920x1080 | 2.43:1 | 2000€ | 1024 x 768 1280 x 800 |
| DEPTHQ | HDs3D2 | 1xDLP 0.65” | 1920x1080 | 2.09:1 | 1900€ | 800 x 600 1024 x 768 1280 x 720 1280 x 800 |
| INFOCUS | IN8606HD | 1xDLP 0.65” | 1920x1080 | 2.09:1 | 680€ | 800 x 600 1024 x 768 1280 x 768 1280 x 800 |
| PANASONIC | PT-RZ370E | 1xDLP 0.65” | 1920x1080 | 2.94:1 | 4200€ | 1024 x 768 |
| PANASONIC | PT-EW730Z | 3xLCD 0.76” | 1280x800 | 2.80:1 | 3300€ | 1024 x 768 1280 x 720 |
| PANASONIC | PT-EZ580 | 3xLCD 0.76” | 1920x1080 | 2.80:1 | 3550€ | 1024 x 768 1280 x 720 |
| VIVITEK | H1185HD | 1xDLP 0.65” | 1920x1080 | 2.09:1 | 840€ | 800 x 600 1024 x 768 1280 x 720 1280 x 800 |
| VIVITEK | D5110W | 1xDLP 0.65” | 1920x1080 | 3.05:1 | 1700€ | 800 x 600 1024 x 768 1280 x 720 1280 x 800 |

Table 6: List of projectors which can process a 120Hz input and are inside the provided budget

In a second step a higher minimum frame rate of 160 Hz is chosen as a “knock-out criterion” and only projectors which are able to reach this frame rate and run continuously are taken into consideration. This step eliminates consumer projectors which use LCD, LCoS and DLP, which are only able to process input signals with a maximum frame rate of 120 Hz. The price per unit is not included in the value benefit analysis shown in Figure 89.

| Criteria | Weighting | Rotational light modulator | | Array projector | | LCD Projector | | LCoS Projector | | DLP Projector | | DLP Lightcrafter | |
|---------------------------------|-----------|----------------------------|------|-----------------|------|---------------|------|----------------|------|---------------|------|------------------|------|
| | | Wissmann | Calc | Fraunhofer | Calc | Calc | Calc | Calc | Calc | Calc | TI | Calc | TI |
| Projection frame rate (>160 Hz) | 0,00% | 5 | 0,00 | 5 | 0,00 | 1 | 0,00 | 1 | 0,00 | 1 | 0,00 | 1 | 0,00 |
| Controller and trigger | 5,00% | 3 | 0,15 | 3 | 0,15 | 1 | 0,05 | 1 | 0,05 | 1 | 0,05 | 1 | 0,05 |
| Mounting | 5,00% | 5 | 0,25 | 5 | 0,25 | 2 | 0,10 | 2 | 0,10 | 2 | 0,10 | 5 | 0,25 |
| Continuous operation | 0,00% | 5 | 0,00 | 5 | 0,00 | 5 | 0,00 | 5 | 0,00 | 5 | 0,00 | 5 | 0,00 |
| Brightness (>500 Lm white) | 10,00% | 4 | 0,40 | 5 | 0,50 | 5 | 0,50 | 5 | 0,50 | 5 | 0,50 | 5 | 0,50 |
| Pattern programming | 20,00% | 1 | 0,20 | 1 | 0,20 | 3 | 0,60 | 3 | 0,60 | 3 | 0,60 | 3 | 0,60 |
| Optics (working distance, area) | 25,00% | 2 | 0,50 | 2 | 0,50 | 5 | 1,25 | 5 | 1,25 | 5 | 1,25 | 2 | 0,50 |
| Cooling | 10,00% | 5 | 0,50 | 5 | 0,50 | 2 | 0,20 | 2 | 0,20 | 2 | 0,20 | 5 | 0,50 |
| Dimensions | 5,00% | 4 | 0,20 | 5 | 0,25 | 2 | 0,10 | 1 | 0,05 | 2 | 0,10 | 4 | 0,20 |
| Weight | 5,00% | 5 | 0,25 | 5 | 0,25 | 1 | 0,05 | 1 | 0,05 | 1 | 0,05 | 5 | 0,25 |
| Price | 0,00% | | 0,00 | | 0,00 | | 0,00 | | 0,00 | | 0,00 | | 0,00 |
| Maintenance and lifetime | 5,00% | 5 | 0,25 | 5 | 0,25 | 2 | 0,10 | 2 | 0,10 | 2 | 0,10 | 5 | 0,25 |
| Supplier | 10,00% | 1 | 0,10 | 1 | 0,10 | 3 | 0,30 | 5 | 0,50 | 5 | 0,50 | 3 | 0,30 |
| Overall | 100,00% | | 2,80 | | 2,95 | | 3,45 | | 3,40 | | 3,45 | | 3,60 |
| | | | | | | | | | | | | | 4,35 |

Figure 89: Value benefit analysis of projectors: Consumer projectors with LCD, LCoS and DLP technology cannot process input signals with a frame rate that exceeds 120 Hz and are consequently not an option. The Lightcrafter modules score the highest overall score and are therefore selected.

It can be seen that the DLP Lightcrafter modules from TI in combination with an optical engine by an external supplier achieves the best overall score and consequently is chosen as the most promising technology. Neither the rotational light modulator by Wissmann nor the array projector by FRAUNHOFER IOF are, as of 2015, in production and require additional developments to adjust to the application of KNAPP. Since KNAPP does not provide a budget for further development of these

projectors, they are not considered as an option. This leaves the Lightcrafter modules from TI as the only viable option for KNAPP.

There were three Lightcrafter models available at the beginning of this study. In January 2015 an additional model of the Lightcrafter was introduced, which uses the DLP6500 chip with a resolution of 1920 x 1080 pixels. The different models are compared and the price is included in the evaluation as shown in Table 7.

| | Lightcrafter 4500 | CEL5500 | STAR-065 with DLP Lightcrafter 6500 | STAR-07 with DLP Discovery V4100 |
|-----------------------------|---|---|---|---|
| Manufacturer | TEXAS INSTRUMENTS | DIGITAL LIGHT INNOVATIONS | VIALUX & TEXAS INSTRUMENTS | VIALUX |
| DMD | DLP4500, 0.45" | DLP5500, 0.55" | DLP6500, 0.65" | DLP7000, 0.70" |
| Controller | DLPC350 | DLPC200 | DLPC900 | DLPC410 |
| Resolution in pixel | 912 x 1144 | 1024 x 768 | 1920 x 1080 | 1024 x 768 |
| DMD orientation | Diamond | Orthogonal | Orthogonal | Orthogonal |
| Frame rate in Hertz | | | | |
| 1. Binary from flash memory | 1. 4225 | 1. 5000 | 1. 9500 | 1. 22727 |
| 2. 8-bit from flash memory | 2. 120 | 2. 500 | 2. 250 | 2. 1900 |
| 3. Video from HDMI | 3. 60 | 3. 60 | 3. N/A | 3. N/A |
| Illumination | Red/Green/Blue LEDs | Green LED | Green LED | Green LED |
| Brightness in Lumen | 150 | 120 | 850 | 850 |
| Throw ratio | 1.4:1 | 1.8:1 | 2.1:1 | 2.1:1 |
| PC Interface | USB HDMI | USB HDMI | USB HDMI | USB |
| Syncs/Triggers | 2x Input triggers 2x Output triggers | 3x Input triggers 3x Output triggers | 2x Input triggers 2x Output triggers | 2x Input triggers 2x Output triggers |
| Dimensions in mm | 122x98x48 | 178x97x77 | 142x127x174 | 110x100x120 |
| Weight in kg | 1.3 | 1.6 | 2.1 | 2.1 |
| Price | 1250 € | 4450 € | 4250 € | 7990 € |

Table 7: Overview of the available DLP Lightcrafter moduls

The STAR-07 module from VIALUX is too expensive for the application of KNAPP and is as a consequence eliminated from the selection of projectors. The Lightcrafter 4500 from TI and the CEL5500 from DIGITAL LIGHT INNOVATIONS (DLI) are both suitable from the perspective of the frame rate, but the throw ratio of both optics is too small. Thus, adjustments to either the optics or the source image have to be done. Furthermore, the brightness of the two modules is rather low, so an adjustment to the light source might be necessary as well.

Since the CEL5500 module is more expensive than the Lightcrafter 4500, while having almost identical specifications, the Lightcrafter 4500, shown in Figure 90, was the projector of choice for testing and getting to know the DLP technology.

The STAR-065 module was not released at the beginning of this thesis and was not an option. It is, however, the most suitable one for the application of KNAPP as explained in chapter 8.



Figure 90: Lightcrafter 4500 (WINTeCH, 2015)

7 Prototype of the projection unit

As described in chapter 6 the Lightcrafter 4500 from TI is the projector of choice and is evaluated by the criteria which are set by KNAPP. Important steps are the programming of the sequence, the triggering of the cameras and setting the luminous flux of the illumination and the size of the projected image.

7.1 Sequence programming

TI provides a graphical user interface (GUI) to setup and control the Lightcrafter 4500 module through the universal serial bus (USB) and to apply or save configurations. The Lightcrafter supports two main modes of operation:

- Video Mode, which displays images from the mini-HDMI connector, bitmaps stored on the flash memory, input through the system board connectors and through the flat panel display (FPD) link. The DLPC350 then applies video processing functions, such as scaling, gamma correction and color coordinated adjustments, and sends the processed image to the DMD. The Video Mode is limited to a maximal frame rate of 60 Hz.
- Pattern Sequence Mode, which displays bitmaps stored in the flash memory or input streamed through the Video ports (mini-HDMI, FPD-link). The DLPC350 does not apply any video processing functions and provides a pixel accurate mode where every pixel maps to the native DMD resolution of 912 x 1140. The Pattern Sequence Mode only depends on the bit depth of the images.

The sequence of patterns can be stored on the flash memory of the Lightcrafter 4500 as 24-bit bitmap file, composed of the three (RGB) 8-bit colors, which each have eight bit planes. The bitmaps for the individual bit planes can be generated with any image manipulation program. Figure 91 shows how to create the composed bitmap by combining the individual bit planes.

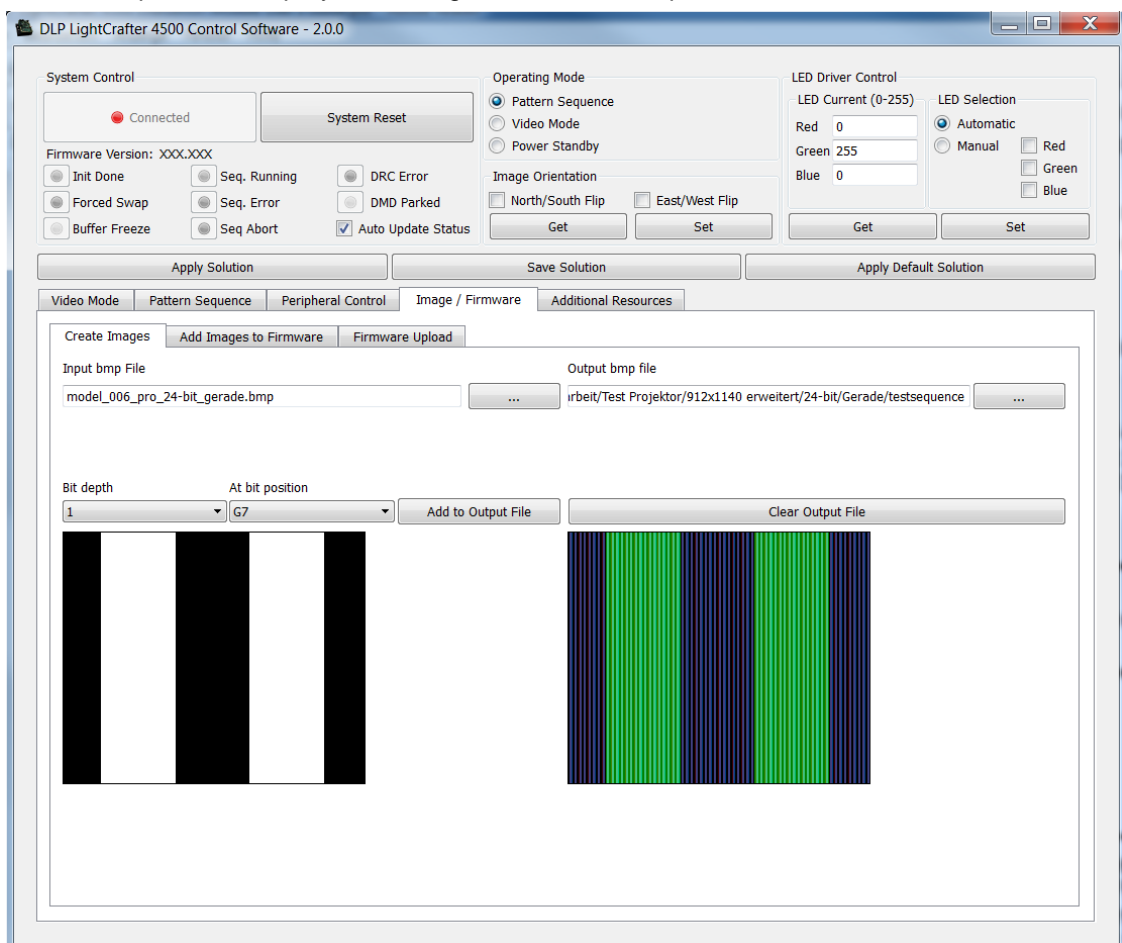


Figure 91: GUI - Creating an image of the pattern sequence

In the tab “Image/Firmware” and the sub-tab “Create Images” of the GUI, the individual bit planes are the input files and can be combined to one 24-bit bitmap, which is the output file. The bit depth of the individual patterns, as well as their bit position, which is labeled from G0 to G7, R0 to R7 and B0 to B7 respectively, can be determined. For each color, bit position 0 is the least significant bit and bit position 7 is the most significant bit. The resulting bitmap is then a combination of the individual bitmaps and looks similar to the image displayed in Figure 92. Note that the image is only colorful because the individual patterns are saved in the bit positions. The actual color of the projection can be chosen when creating the pattern sequence.

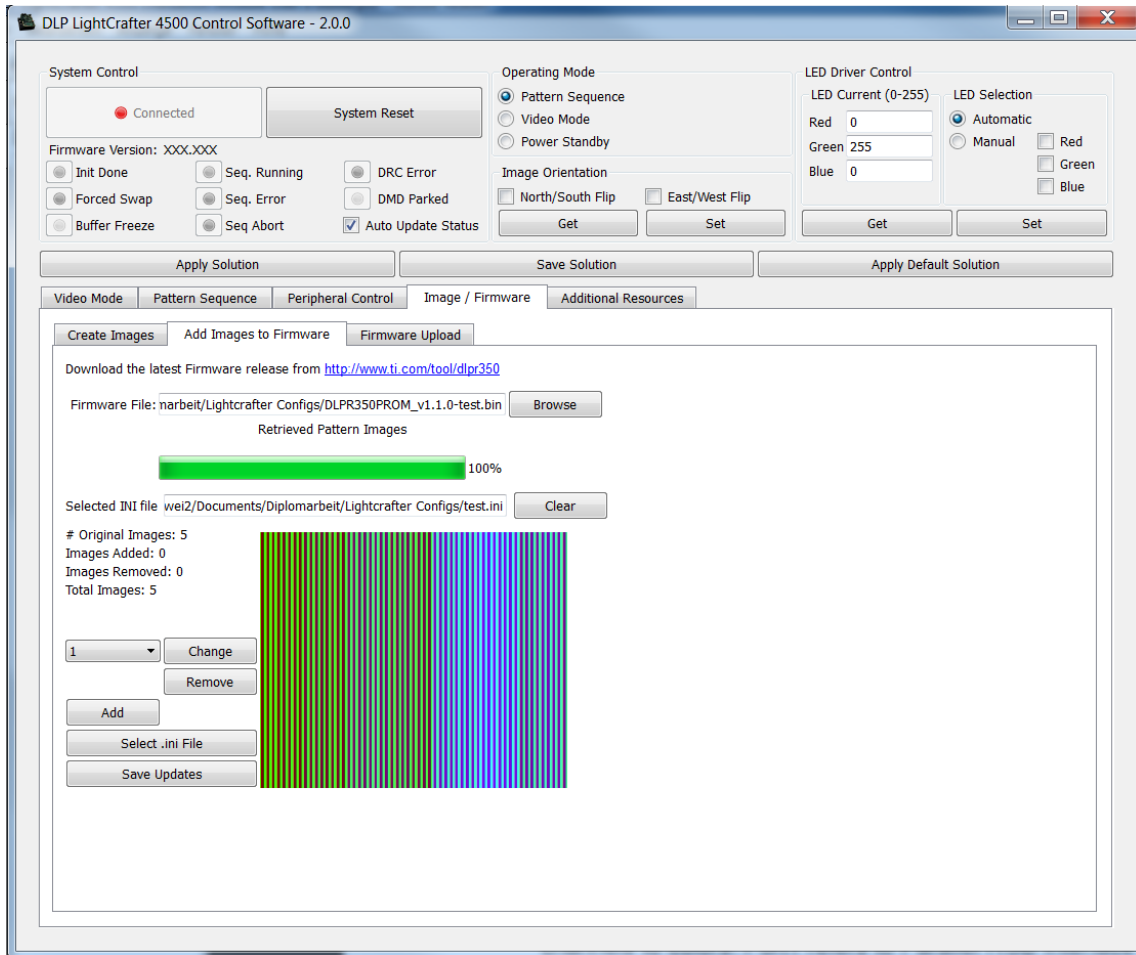


Figure 92: GUI - Adding images and configurations to the firmware

In the sub-tab “Add Images to Firmware” the created bitmap and a configuration file (explained below) can be added to the firmware. The updated firmware can then be uploaded to the Lightcrafter 4500 by using the sub-tab “Firmware Upload”. The flash memory has a capacity of 32 MB, which provides the opportunity to store multiple pattern sequences. The DLPC350 can store two 24-bit images in its internal display buffer, which provides the possibility to buffer a second image, while the first one is displayed. After the image is saved in the buffer, it is sent to the DLP4500 DMD, one bit plane at a time. To load the image into the buffer for the first time takes at worst 200 ms, depending on the complexity of the image. Once it is loaded into the buffer, no additional time is required to repeatedly display the pattern sequence.

In the tab “Pattern sequence” the settings for the pattern sequence can be adjusted as displayed in Figure 93. The configurations can be saved as “Solutions” and included into the firmware to make it the default configuration, which is loaded when the Lightcrafter is started up.

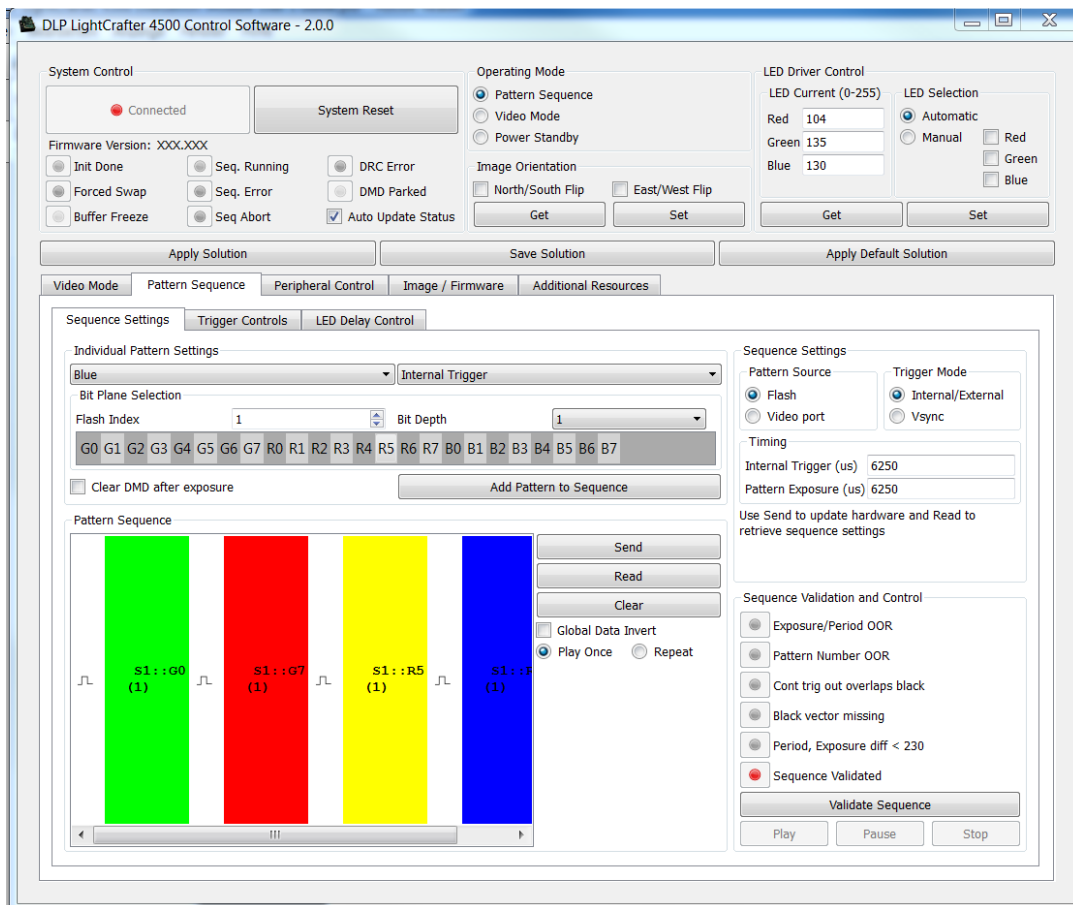


Figure 93: GUI - Pattern sequence settings

To add a pattern to the sequence, the flash index of the stored bitmap and the desired bit plane of the bitmap, are chosen. Additionally, the LEDs which are used for illumination, the bit-depth and an internal or external trigger, which is used to synchronize other components with the Lightcrafter, can be added for each individual pattern of the sequence. If a black image in between the patterns is required, the “Clear DMD after exposure” box needs to be checked.

The pattern source and the trigger mode as well as the timing of internal trigger and pattern exposure can be adjusted on the right hand side, where “Internal trigger” in μs defines the time between patterns and “Pattern Exposure” in μs defines the time a single pattern is displayed.

In the upper right corner, the LED current can be adjusted, ranging from 0 for no current to 255 for maximum current. The sub-tabs “Trigger Controls” and “LED Delay Control” adjust the delay timings of the trigger and the LEDs. After the desired sequence is set, it can be validated and sent to the Lightcrafter.

If the configuration is validated, it can be saved with the “Save solution” button to a configuration file, which can then be included into the firmware and uploaded to the Lightcrafter as described above.

7.2 Triggering of cameras

The Lightcrafter 4500 module has two trigger inputs and two trigger outputs which can be used to, for example, synchronize a camera with the Lightcrafter. TRIG_IN_1 tells the DLPC350 to advance to the next pattern, while TRIG_IN_2 starts and stops the pattern sequence. TRIG_OUT_1 is active for the full exposure time of the pattern, while TRIG_OUT_2 only indicates the start of the pattern sequence as shown in Figure 94, where one sequence consists of four patterns.

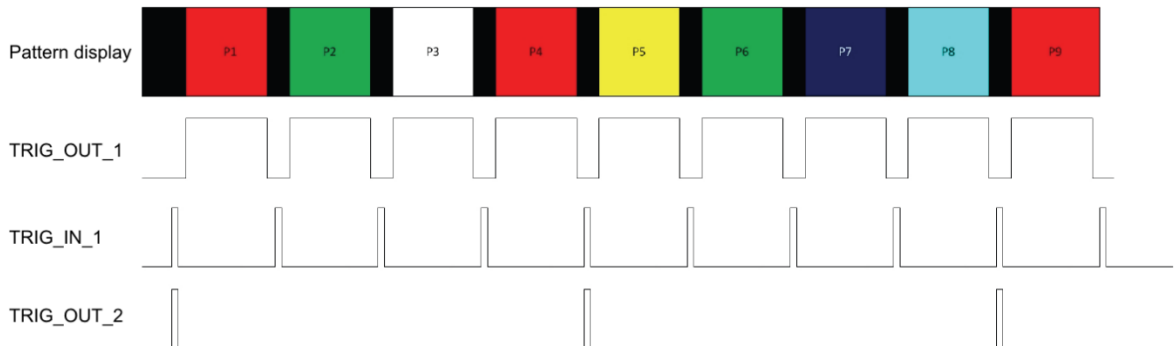


Figure 94: Trigger of Lightcrafter 4500 (TI, 2014)

The location of the trigger connectors and the jumpers to select the voltage are shown in Figure 95.

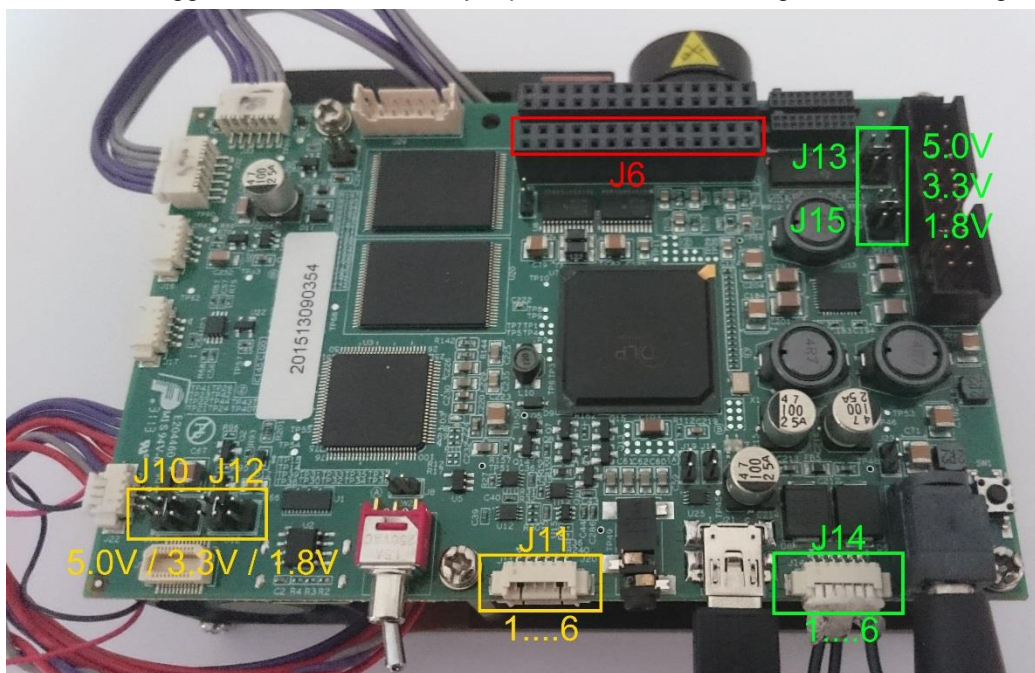


Figure 95: Lightcrafter 4500 Input and Output Connectors

J11 is the input trigger, which uses a 1.25 mm six-pin connector with the pin assignment listed in Table 8:

| | Pin | Supply Range |
|---------------------|-----|--|
| Trigger In 1 Supply | 1 | External or internal 1.8V, 3.3V and 5.0V selectable at J10 |
| Trigger In 1 | 2 | |
| Ground | 3 | Ground |
| Trigger In 2 Supply | 4 | External or internal 1.8V, 3.3V and 5.0V selectable at J12 |
| Trigger In 2 | 5 | |
| Ground | 6 | Ground |

Table 8: Input trigger connector J11 pin assignment of the Lightcrafter 4500

J14 is the output trigger, which uses a 1.25 mm six-pin connector with the pin assignment listed in Table 9:

| | Pin | Supply Range |
|----------------------|-----|--|
| Trigger Out 1 Supply | 1 | External or internal 1.8V, 3.3V and 5.0V selectable at J13 |
| Trigger Out 1 | 2 | |
| Ground | 3 | Ground |
| Trigger Out 2 Supply | 4 | External or internal 1.8V, 3.3V and 5.0V selectable at J15 |
| Trigger Out 2 | 5 | |
| Ground | 6 | Ground |

Table 9: Output trigger connector J14 pin assignment of the Lightcrafter 4500

For testing the trigger features of the Lightcrafter 4500, a BAUMER VisiLine CCD camera (VLG-02M) is connected to the trigger output connector J14. The sequence is displayed with the settings listed in Table 10:

| Parameter | Value |
|--|---------------------|
| Lightcrafter 4500 | |
| Operating mode | Pattern Sequence |
| LED Current R / G / B | 0 / 255 / 0 |
| Clear DMD after exposure | No |
| Pattern Source | Flash |
| Trigger Mode | Internal / External |
| Internal Trigger in μs | 6250 |
| Pattern Exposure in μs (equals 160Hz) | 6250 |
| VisiLine VLG-02M | |
| Trigger delay in μs | 100 |
| Trigger | Rising Edge |
| Exposure time in μs | 400 |

Table 10: Configurations of the Lightcrafter 4500 and the VisiLine VLG-02M

All patterns could be captured accurately. This demonstrates that the Lightcrafter 4500 is capable of synchronizing the used cameras.

The Lightcrafter 4500 module also has several configurable general-purpose input and output (GPIO) pins, which can be configured in the tab "Peripheral Control" of the GUI and used via the connector J6.

7.3 Luminous flux

The optical module of the Lightcrafter 4500 comes with three LEDs manufactured by OSRAM. According to the datasheets, the LEDs have the specifications which are summarized in Table 11:

| | Luminous flux in Lm | Forward current in A | Wavelength in nm |
|--------------------|---------------------|----------------------|------------------|
| LE A Q9WP (red) | 97 to 180 | 3.5 | 612...624 |
| LE CG Q9WP (green) | 315 to 500 | 5.0 | 500...600 |
| LE B Q9WP (blue) | 74 to 142 | 5.0 | 452...465 |

Table 11: Specifications of the LEDs of the Lightcrafter 4500 by OSRAM

The luminous flux is depending on the manufacturing tolerances of the LED and the current with which the LEDs are supplied. To measure the luminous flux of a light source, two methods are possible. Either using an Ulbricht sphere or a goniophotometer. How much of the emitted light of the LEDs can be used for the projection depends on the etendue of the optical system. The etendue G is a geometric function of the area A of the light source and the solid angle Ω into which the light propagates through a medium with the refractive index n and can be calculated as

$$G = n^2 \int_A \int_{\Omega} \cos(\theta) dA d\Omega \quad (7.1)$$

where θ is the angle between the normal of the area A and the direction of the light propagation. The etendue is a limiting factor and basically describes how much light the system can put through. A perfect loss-less optical system is required to obtain the same amount of light emitted by the light source at the

projection surface. Real optical systems always increase the etendue and thus reduce the light throughput. (Wendel, 2014)

To measure the luminous flux of a projector, the method according to the measurement standards for projectors IEC 61947-1:2002 and IEC 61947-2:2002 provided by the International Electrotechnical Commission (IEC) are used. The luminous flux in Lumen of the projector is derived from the standardized measurement of the illuminance in Lux. The measurement requires that

- The projector is calibrated with a test pattern as illustrated in Figure 96 (a), and set up so that the whole desired projection surface is illuminated. The projector needs to be calibrated so that neighbored rectangles are distinguishable. The width of every rectangle is 10 % of the height of the illuminated area. The height of the rectangles and the distance between the two patterns are 5 % of the height of the illuminated area.
- The measurement is taken in a dark room, where the projector is the only light source. Less than 1 % of the illumination must come from other sources.
- The measurement projection needs to be a 100 % white image.
- The photometer needs to be photopic and cosine-corrected and the calibration has to be based on a national norm.
- The illuminated area is divided into nine subareas and the measurements are taken at the respective centers as shown in Figure 96 (b). (IEC, 2002)

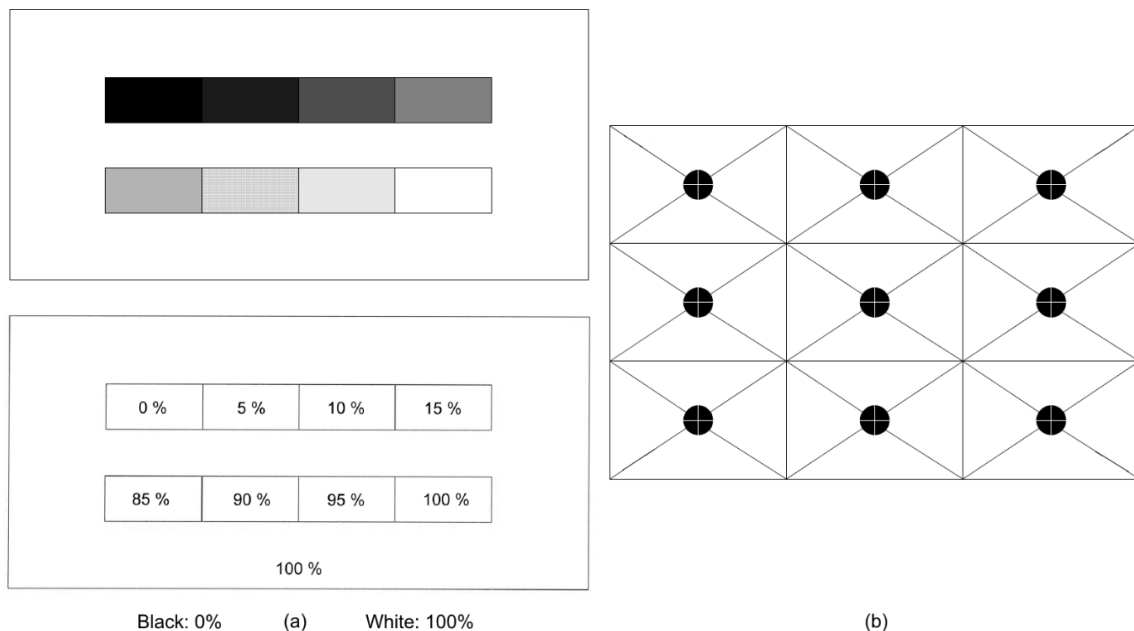


Figure 96: IEC test pattern for projector calibration (a) and measurement points for illuminance measurement (b) according to IEC 61947-1:2002 (IEC, 2002)

The Lumen (IEC) are obtained by calculating the average illuminance and multiplying it with the illuminated area. This standardized value enables the comparison of different projectors.

The light engine of the Lightcrafter 4500 is specified with a typical luminous flux of 150 Lm for white illumination. A measurement according to the IEC standard is conducted. The measurement setup has the parameters listed in Table 12:

| | | | |
|------------------------------------|----------------|-----|-----|
| Measurement distance in mm | 1550 | | |
| Image width in mm | 1107 | | |
| Image height in mm | 692 | | |
| Illuminated area in m ² | 0.766 | | |
| Measurement device | Roline RO-1332 | | |
| Measurement | M1 | M2 | M3 |
| Current of red LED (0...255) | 103 | 0 | 0 |
| Current of green LED (0...255) | 135 | 255 | 255 |
| Current of blue LED (0...255) | 130 | 0 | 0 |

Table 12: Parameters for luminous flux measurement

The room is fully darkened and the projector is calibrated according to the IEC standard. The illuminance is measured at the nine measurement points and the average illuminance and the luminous flux are calculated. The measurement of the Lightcrafter shows a luminous flux of 231 Lm (IEC) for white illumination with standard configurations. The individual measurement results are shown in Figure 97.

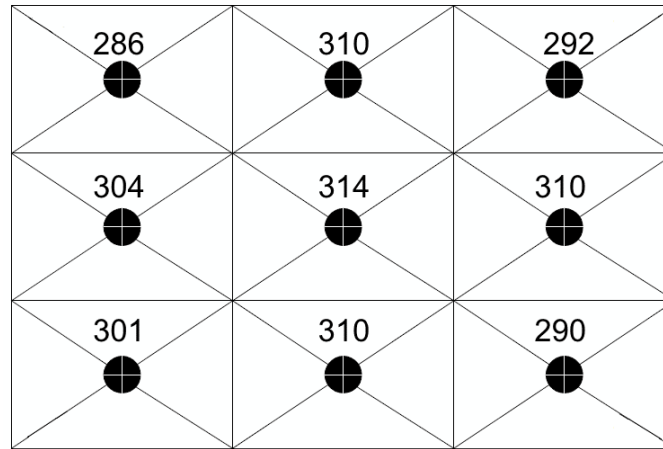


Figure 97: Measurement M1, white light from standard LEDs, standard configuration. Measured values are in Lux.

A second measurement is then conducted with the same parameters, but only with the green LED at the maximum current. The measurement shows a luminous flux of 176 Lm (IEC). Figure 98 shows the individual measurement results at the nine points.

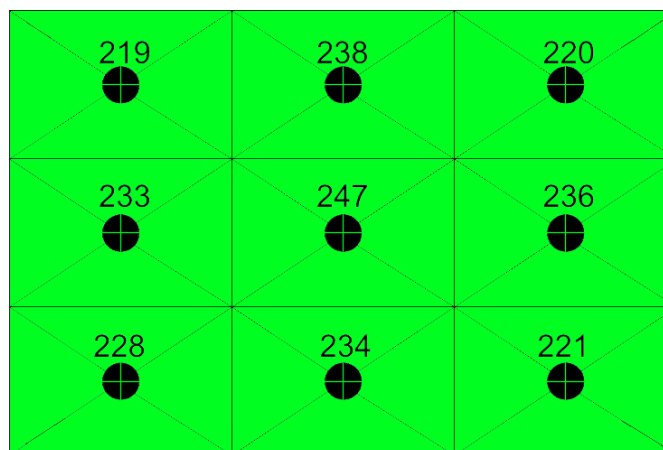


Figure 98: Measurement M2, green standard LED, maximum current. Measured values are in Lux.

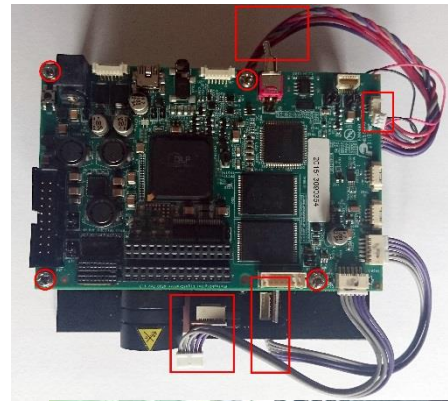
The required minimum luminous flux of 500 Lm (IEC) for white light illumination is an estimated value based on the experience of the 3D-measurement system provider. The currently used multimedia projector from CASIO (XJ-A146) is specified with 2500 Lm (ANSI), but since only the green light of the projector is used, the actual luminous flux for the green portion of the light is significantly lower.

Increasing the light output of the Lightcrafter 4500 is tested to see how easily the modification can be done. Figure 99 shows the required steps to disassemble the projector and gain access to the LEDs of the optical engine. The required tools are:

- Cross-tip screwdriver PH 000 and PH 1, which is also able to reach the screws of the heat sink. So, the diameter of the metal shaft should not be larger than 3 mm on a length of 40 mm measured from the tip of the screwdriver.
- Hot air gun to soften the thermal adhesive and the sealant of the LEDs.
- Scalpel or any other sharp and thin tool to remove the adhesive and the sealant.

1

- Disconnect power supply
- Disconnect cables of LEDs and fan
- Disconnect flex cable of DMD
- Loosen the four screws and remove circuit board



2

- Loosen the four screws of the heat sink
- Soften adhesive with hot air gun and carefully remove heat sink from fixture with a scalpel



3

- Loosen the six screws of the fixture
- Soften sealant with hot air gun and carefully remove LEDs from housing
- Soften adhesive with hot air gun and carefully remove LEDs from fixture



Figure 99: Disassembly process of the Lightcrafter 4500 to change the LEDs

The disassembly process is rather straight forward, however, removing the thermal adhesive and the sealant is rather difficult and time-consuming. A hot air gun is necessary to soften the thermal adhesive

to be able to carefully remove the L-shaped fixture from the heat sink with a thin scalpel. After removing the L-shaped fixture from the heat sink, the screws which connect it to the housing of the optical system can be removed. The LEDs are mounted onto an aluminum plate which is glued onto the L-shaped fixture and a sealant fills the gaps between the LEDs and the aluminum plate. Again the hot air gun is used to soften the sealant and the adhesive, which are then carefully removed with the scalpel. After this step is performed, the LEDs can be removed. The whole disassembly process takes roughly an hour, since cooling pauses are necessary to prevent the LEDs and the optical components from overheating. The force applied with the scalpel has to be very gentle, since the housing of the optical system is made out of plastic and may otherwise break. Once the LEDs are removed, a more powerful LED, such as the OSTAR Projection Power LE CG P1W from OSRAM, can be installed. The specifications of the LE CG P1W are presented in Table 13.

| | Luminous flux in Lm | Forward current in A | Wavelength in nm |
|-------------------|---------------------|----------------------|------------------|
| LE CG P1W (green) | 2800 to 4500 | 10.0 | 500...600 |

Table 13: Specifications of the LE CG P1W by OSRAM

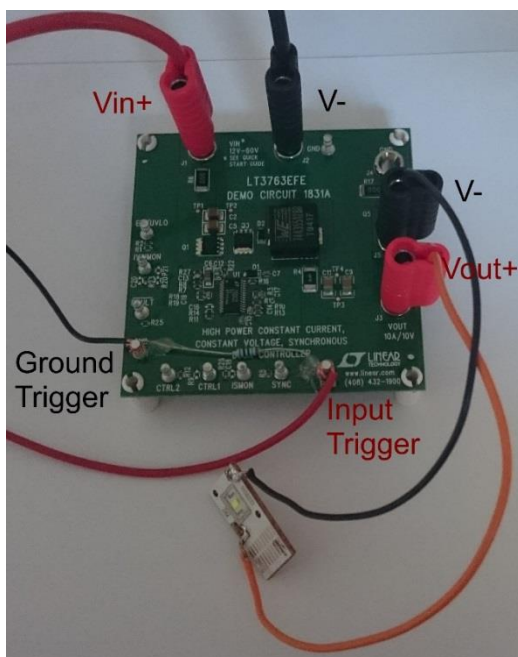


Figure 100: Wiring of LT3763 LED driver with LE CG P1W

As can be seen from Table 13 the new LED has a forward current of 10 A. Since the onboard LED driver of the Lightcrafter 4500 can only supply a maximum current of 4.3A, an external LED driver, such as the LED Driver Controller from LINEAR (LT3763), is necessary. This driver is a step-down converter, which converts the 24V input of the power supply into a 10 A / 10 V output to supply the LED. The driver can be controlled with Pulse Width Modulation (PWM) and is connected to the same output trigger of the Lightcrafter 4500 as the camera. This enables to synchronization of the LED with the pattern sequence. Figure 100 shows the LE CG P1W, which is connected to the LED driver controller.

As can be seen in Figure 100, the wires are soldered temporarily to the LED for testing. Normally, a connector would be soldered onto the copper plate of the LED, but because the copper plate is a very good heat conductor, only a connection at the corners was possible with the available soldering bolt.

Since the LT3763 board supplies the LED constantly with power and only turns it off if it receives a PWM signal, a 10 kΩ resistor is added between ground and input trigger to invert the operation mode. The LED is then precisely positioned in place of the standard green LED of the Lightcrafter and connected to the L-shaped fixture with thermal adhesive tape. The screws of the L-shaped fixture are then again inserted and thermal adhesive tape is applied between the fixture and the heat sink.

The synchronization of the LED with the pattern projection was successfully tested. A comparison measurement of the new LED showed a luminous flux of 282 Lm (IEC), which is an increase of roughly 60 %. The individual results of the third measurement are shown in Figure 101.



Figure 101: Measurement M3, green high-power LED. Measured values are in Lux.

7.4 Optics

The optical system of the Lightcrafter 4500 (IPD1231GP) is manufactured by IVIEW DISPLAYS. The specifications of the IPD1231GP summarized in Table 14:

| | |
|------------------------------|-------|
| Effective Focal length in mm | 14 |
| Offset in % | 100 |
| Throw ratio | 1.4:1 |
| Distortion in % | ≤ 1.0 |

Table 14: Specifications of the optics of the Lightcrafter 4500 (IVIEW DISPLAYS, 2014)

The structure of the optical system is shown in Figure 102.

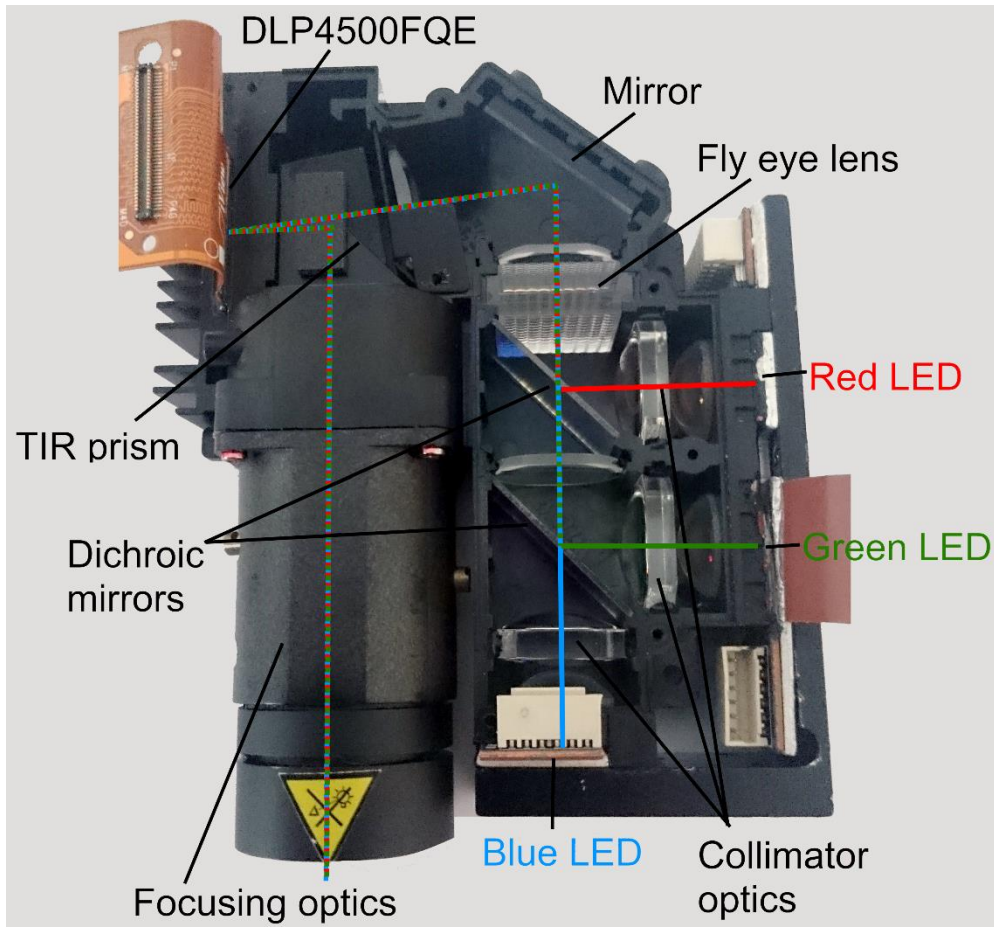


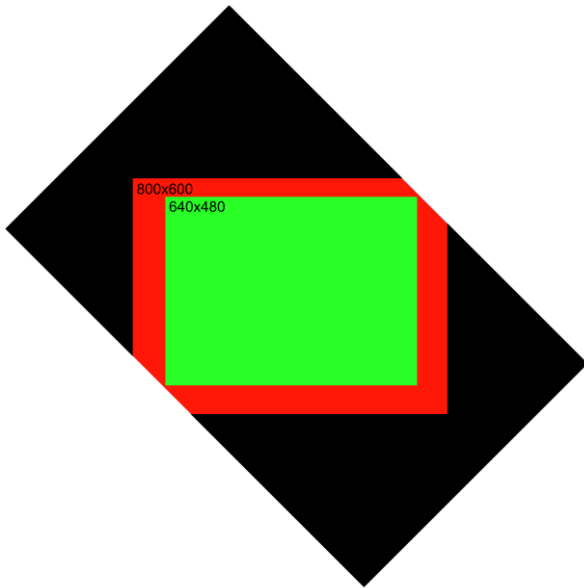
Figure 102: Optical system of the Lightcrafter 4500

After each LED a collimator is mounted to collect the light which is emitted by the LEDs and generate a narrow beam. The light of the blue LED passes two dichroic mirrors, which reflect the green and the red light respectively. The dichroic mirrors combine the three beams to one co-linear beam, which then passes through a fly eye and a condenser lens that make sure that the intensity of the light is uniform. The uniform co-linear beam of light then is reflected by a mirror, passes through a total internal reflection (TIR) prism and is incident on the DLP chip. Depending on the state of the micro-mirrors, the beam of light is either reflected into the TIR prism so that it is guided into the focusing optics of the Lightcrafter, or it stays inside the optical system of the Lightcrafter and is absorbed.

The standard focusing optics of the Lightcrafter 4500 are not suitable for the application of KNAPP because the throw ratio is too small. This results in a projection at the working distance which illuminates roughly four times the area which needs to be measured. Unfortunately, the standard focusing optics are already the ones with the highest throw ratio that IVIEW DISPLAYS offers. Moving the projector more closely to the measured objects is not an option, since the space is required by the robotic arm to maneuver and ensure that no collision occur.

As discussed in chapter 6, the necessary throw ratio for the application of KNAPP is 2.67:1. There are three options of how to reduce the size of the projected image, these are:

- Manipulate the source image.
- Substitute the optics of the Lightcrafter.
- Use an additional lens in front of the projector.



Manipulating the source image provides a couple of challenges. First off, due to the diamond alignment of the mirrors of the DMD, the CCD camera registers jagged vertical and horizontal lines as described in 5.2.8. To eliminate these jagged lines, the pattern needs to be drawn diagonally. Since the DMD offers a pixel accurate projection, a pattern can be generated so that the straight lines run diagonally across the DMD. To fit the pattern into the diagonal of the chip, a maximal resolution of 640 x 480 pixels is possible as displayed in Figure 103.

The reduced resolution, however, also reduces the accuracy of the 3D-measurement. Additionally, the projector has to be tilted by 45° to project the image onto the desired area. This is, however, the fastest and easiest way to reduce the size of the projection.

Figure 103: Shrinking the source image and projecting it diagonally

Substituting the optics of the Lightcrafter is another possibility. There are three general limitations for suitable optics:

- The optics have to be able to deal with the working distance of 1600 mm, which is roughly the image distance i shown in Figure 104.
- The optics have to be able to deal with the flange focal distance of 35 mm, which is the distance from the mounting flange of the optics to the DMD chip. This is roughly the object distance o as illustrated in Figure 104.
- The dimensions of the optics need to be compatible with the compact dimensions of the Lightcrafter, since there is very limited space at the mounting flange as shown in Figure 107.

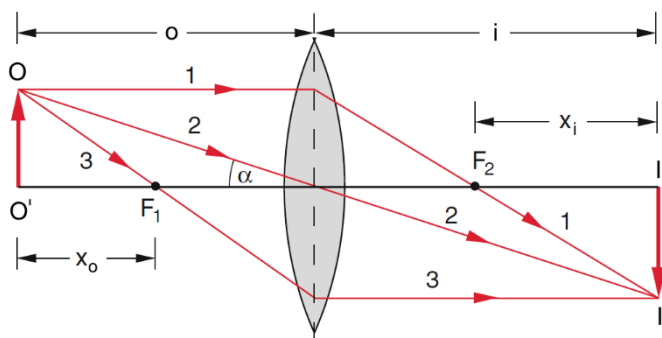


Figure 104: Construction of the image generated by a thin lens (Demtröder, 2006, p. 273)

From the lens equation for thin lenses

$$\frac{1}{f} = \frac{1}{i} + \frac{1}{o} \quad (7.2)$$

the necessary focal length can be calculated as

$$\frac{1}{f} = \frac{1}{35} + \frac{1}{1600} \quad (7.3)$$

$$f = 34.35 \text{ mm} \quad (7.4)$$

Since the image distance i is much bigger than the object distance o , the required focal length f is almost equal to the object distance.

This can be explained by inserting $o = f + x_o$ and $i = f + x_i$ in (7.2), whereby Newton's projection law is obtained as

$$x_o x_i = f^2. \quad (7.5)$$

The magnification M can be derived from Figure 104 using the intercept theorem

$$M = \frac{\overline{II'}}{oo'} = -\frac{i}{o} = \frac{f}{f-o}. \quad (7.6)$$

If $M < 0$, then the image has the opposite orientation as the object and for $M > 0$, the image has the same orientation as the object. From (7.6) it can be seen that $M < 0$ for $o > f$, which means that if the object distance o is bigger than the focal length f of the lens, the image is upside down. For $o = 2f$ follows that $M = -1$, which means that the image and the object have the same size. For $o = f$ follows that $M = \infty$, which means that the image size converges to infinity and $i = \infty$. (Demtröder, 2006, p. 273)

To test if the calculated focal length is sufficient, a basic objective is built and an achromatic lens (G322286000) from QIOPTIQ with a focal length of 35 mm is used. The objective is shown in Figure 105.

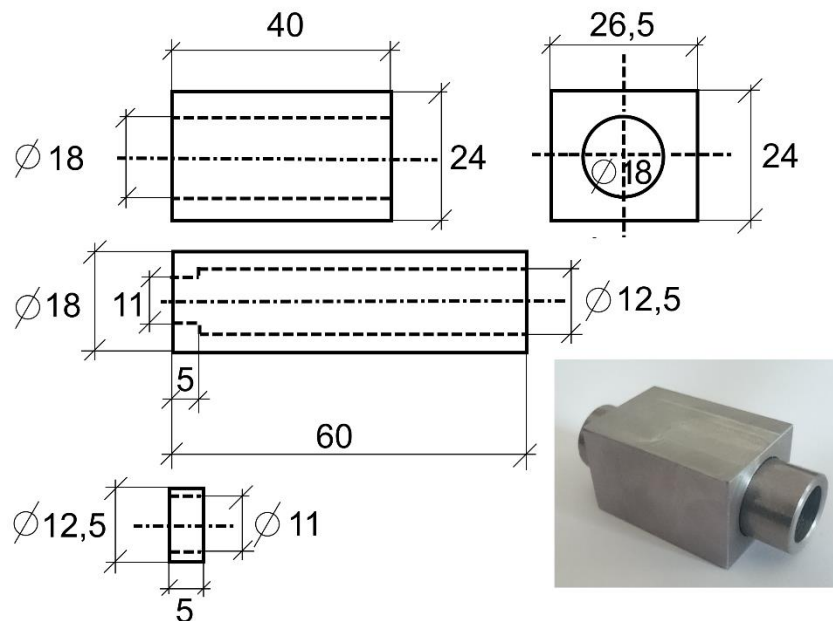


Figure 105: Self-made objective using an achromatic lens with a focal length of 35 mm from QIOPTIQ

The projected image has the correct size, which confirms the necessary focal length, however, significant distortions and aberrations are observed as displayed in Figure 106. This is due to the estimated dimensions of the optical system and the low precision of the self-made objective.



Figure 106: Projection with self-made objective and observed distortions

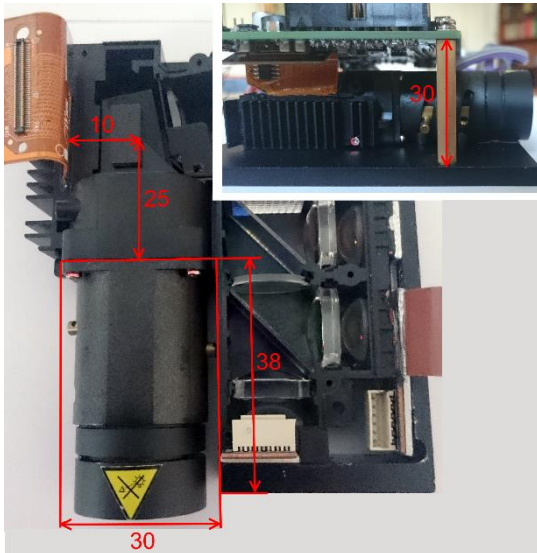


Figure 107: Available space to mount the optics

There are several optics available that have the necessary focal length and the required dimensions to be mounted onto the Lightcrafter, but they cannot cope with the relatively large flange focal distance of 35 mm. Optics with the standardized C-mount interface require a flange focal distance of precisely 17.52 mm to project a focused image. Because of the housing of the optical system of the Lightcrafter, it is not possible to move the mounting point closer to the DMD chip, which prevents the use of optics with the C-mount. Another standardized interface, which is commonly used, is the F-mount. The F-mount requires a flange focal distance of 46.50 mm and would consequently be able to deal with the specifications of the mounting point of the Lightcrafter. F-Mount optics are, however, designed for bigger sensors and are a lot bigger in size. The limitations due to the compact dimensions of the Lightcrafter, moves the closest mounting point for such optics to a distance of 73 mm as illustrated in Figure 107, which prevents the use of optics with the F-mount.

The only optics which are capable of dealing with a flange focal distance of 73 mm are optics of medium format cameras, such as PENTAX, PENTACON, ZEISS, BRONICA, MAMIYA and HASSELBLAD (Westin, 2012). These optics are, however, only available with focal lengths between 50 and 300 mm which generates an image which is too small at the working distance of 1600 mm. The only optics with a focal length near the required focal length are fisheye optics, which, however, cause significant distortions of the image. Furthermore, medium format cameras are not produced anymore and most of the optics available are second hand and as a result not an option for KNAPP.

Apart from using already existing optics, customized optics can be designed and adjusted to the specifications of the Lightcrafter. Several enquiries to lens manufacturing companies were unfortunately unsuccessful, which is mainly due to the costs for the development of customized optics and the price per unit, which would exceed the provided budget for the projection unit significantly. Therefore, designing custom optics is not an option for KNAPP.

Using an additional lens after the optics of the Lightcrafter is also a possibility to reduce the size of the projected image. For a lens system consisting of two lenses, the focal length of the system can be calculated as

$$\frac{1}{f} = \frac{1}{f_1} + \frac{1}{f_2} - \frac{D}{f_1 f_2} \quad (7.7)$$

If $D \ll f_1$ and $D \ll f_2$ is true, then the last term in (7.7) can be neglected, which means that the reciprocal focal lengths of two lenses, which are positioned closely to each other, add up. (Demtröder, 2006, p. 275)

There are lenses available which are specifically designed for such an application, such as the ScreenStar conversion lenses SST150 by NAVITAR. These lenses are, however, only manufactured upon request and are consequently rather expensive. Furthermore, an additional lens always increases the distortions of the image, which significantly influence the 3D-reconstruction. This is due to the relation shown in Figure 108.

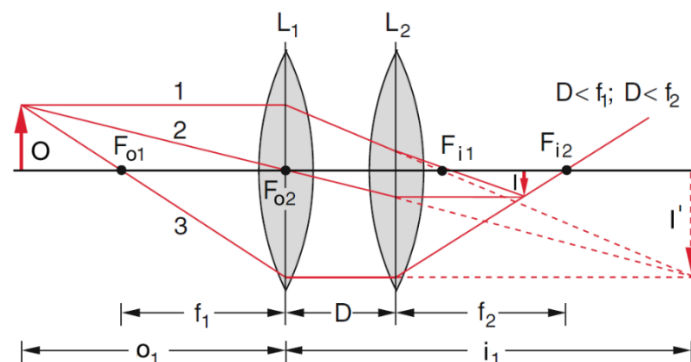


Figure 108: Construction of the image generated by two lenses which are close to each other: The additional lens L_2 reduces the size of the image I' to the size of image I and moves it closer towards the lens. (Demtröder, 2006, p. 276)

An additional lens L_2 reduces the size of the image I' to the size of image I . However, this does also inevitably move the image closer to the lens, which results in distortions of the image at the projection surface, if the projector is not moved closer to the surface. Figure 109 shows the test setup, the projection at a working distance of 1600 mm and the observed distortions.

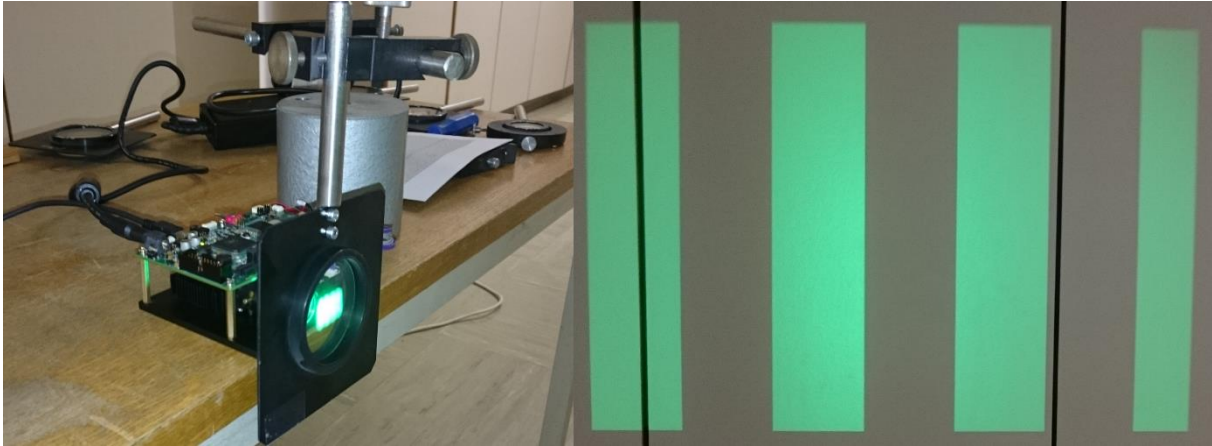


Figure 109: Test of converging lens in front of projector to reduce the size of the image

The Lightcrafter is positioned at a distance of 1600 mm from the projection surface and the focus is adjusted so that the image is focused. Then a converging lens is positioned 15 mm in front of the optics of the Lightcrafter and the focus is readjusted to generate a focused projection. This is, however, not possible without causing distortions to the image. Especially in the upper corners of the projection, distortions are noticeable and the image is not completely in focus anymore. The astigmatism correction of the optics of the Lightcrafter is suspended by the converging lens. A tradeoff between image quality and image distance / image size is observed. After consultation with the 3D-measurement provider, it was determined that these distortions are well outside the limits that the 3D-measurement system can handle. Hence, using an additional lens is not an option.

Summarizing, the only option to reduce the size of the projection to the specifications of KNAPP is by manipulating the source image. For the Lightcrafter 4500 this needs to be done by using a diagonal pattern with a reduced resolution of 640 x 480 pixels and tilt the projector by 45° to eliminate the jagged lines. The other options are either not feasible or exceed the budget provided by KNAPP.

7.5 Cooling

Since the green power LED is only activated for the duration of one projection cycle (~150 ms) and then deactivated until the next measurement is required (~3 s), no active cooling is necessary.

8 Summary and future work

8.1 Summary

In this thesis, an overview of the applications and the methods for 3D-measurement systems is provided. Since the application of KNAPP uses structured light projection to measure objects three-dimensionally, the focus is then on analyzing existing projection techniques which can be used for the necessary high-speed projection of a binary fringe pattern. The Lightcrafter 4500 is tested in regards to the programming of the pattern sequence, the triggering of cameras, the increasing of the light output and the adaption of the optics to the working distance and projection area of the application of KNAPP.

The Lightcrafter 4500 is a possible solution for the application of KNAPP, if the reduced resolution of the measurement is acceptable. The sequence programming and the configuration of the Lightcrafter 4500 is performed fast and easily. So is the triggering of cameras and other external components. The increase of the luminous flux of the Lightcrafter 4500 requires the disassembly of the optical system, which needs to be done carefully and is a rather time-consuming process. Damages to the optical system during the disassembly process cannot be ruled out. An additional component, the external LED driver, is necessary to supply the high-power LED with sufficient current. The synchronization of the external LED driver with the Lightcrafter 4500 is unproblematic. The adaption of the optics of the Lightcrafter 4500 is, however, the biggest challenge and a complex problem to solve. Neither designing customized optics nor using additional lenses lead to the desired result of an almost distortion-free projection of the correct size without exceeding the budget provided by KNAPP. The easiest solution is to manipulate the source image and change the orientation of the Lightcrafter 4500. This, however, leads to a reduced resolution of the projection and consequently to a reduced accuracy of the 3D-measurement. The same idea can also be applied when using another advanced light control module, such as the CEL5500 from DLI presented in chapter 6. Due to the orthogonal alignment of the micro-mirrors of the CEL5500 no tilting of the projector is necessary and the resolution only needs to be reduced to 800 x 600 pixels to gain the correct image size.

8.2 Lightcrafter 6500

As already mentioned in chapter 6, TI launched a new platform in the segment of advanced light control, the Lightcrafter 6500 shown in Figure 110 which contains the DLP6500 chipset and the DLPC900 controller. The DLP6500 has a native resolution of 1920 x 1080 pixels with an orthogonal micro-mirror alignment and the DLPC900 enables a frame rate of up to 9500 Hz of binary patterns stored in the flash memory of the Lightcrafter 6500. VIALUX adapted their optical module to the specifications of the new Lightcrafter 6500 and launched the STAR-065 in January 2015 shown in Figure 110. The STAR-065 module includes optics with a throw ratio of 2.1:1 and a green high-power LED with a luminous flux of 850 lm. The specifications of the Lightcrafter 6500 and the STAR-065 model are shown in Table 15 below:

| | |
|-----------------------------|-------------------------------------|
| | STAR-065 with DLP Lightcrafter 6500 |
| Manufacturer | VIALUX and Texas Instruments |
| DMD | DLP6500, 0.65" |
| Controller | DLPC900 |
| Resolution in pixel | 1920x1080 |
| DMD orientation | Orthogonal |
| Frame rate in Hertz | |
| 4. Binary from flash memory | 4. 9500 |
| 5. 8-bit from flash memory | 5. 250 |
| 6. Video from HDMI | 6. N/A |
| Illumination | Green LED |



Figure 110: Lightcrafter 6500 (top) (TI, 2014) and STAR-065 (bottom) (VIALUX,

| | |
|------------------------|---|
| Luminous flux in Lumen | 850 |
| Throw ratio | 2.1:1 |
| PC Interface | USB HDMI |
| Syncs/Triggers | 2x Input triggers 2x Output triggers |
| Dimensions in mm | 142x127x174 |
| Weight in kg | 2.1 |
| Price | 4250 € |

Table 15: Specifications of the Lightcrafter 6500 by VIALUX

Regarding the specifications of the application of KNAPP, it can be summarized that:

- The configuration of the Lightcrafter 6500 is similar to the configuration of the Lightcrafter 4500 and can therefore be adapted.
- The sequence programming is done in the same way as for the Lightcrafter 4500, only the design of the GUI is a little bit different. Apart from the design, the same features and functionalities are available for the Lightcrafter 6500.
- The Lightcrafter 6500 also has two input and output triggers which can be used to synchronize cameras with the projector.
- The luminous flux of the Lightcrafter 6500 is more than sufficient. If necessary, the use of a more powerful LED is possible, since the internal LED driver can supply up to 24 A.
- The optics of the Lightcrafter 6500 have a throw ratio of 2.1:1, which is still below the required throw ratio for the application of KNAPP. But due to the higher resolution of the DLP6500 and the orthogonal alignment of the micro-mirrors, the manipulation of the source image is very easy. The pattern sequence can be programmed so that instead of the full array of the DLP6500 only an area of 1280 x 1024 pixels is used for the projection. The image size is then roughly 600 mm wide, which is exactly the required width.
- The higher resolution of the projection also enables the use of cameras with a higher resolution, which increase the accuracy of the 3D-measurement.
- With a total price of 4250 € for both modules, this solution is also inside the budget provided by KNAPP.

8.3 3D-measurement system from ENSHAPE

During the research for this thesis, several suppliers of 3D-measurement systems were contacted. The startup company ENSHAPE founded by Marcus Große and Martin Schaffer, situated in Jena in Germany, showed particular interest in a cooperation with KNAPP.

Their measurement principle is based on projecting a statistical speckle pattern, generated by a laser light source, onto the object and shift the pattern in time. Two CCD cameras capture the scene and the correspondence between a pixel in camera 1 and camera 2 is found by comparing the intensity sequences. The pair of pixels with the highest correlation value is then said to be the corresponding pair. This probability encoding method delivers highly accurate measurement results in real time, which fulfills the requirements for the application of KNAPP. (Lutzke, Schaffer, Kühmstedt, Kowarschik, & Notni, 2013)

Figure 111 shows a container filled with products which typically need to be measured. Test measurements of this container were performed and segmentation algorithms were applied by ENSHAPE. The results of the 3D-measurement and the segmentation, shown at the bottom of Figure 111, are promising and further measurements are planned.



Figure 111: Test container for the measurement by ENSHAPE (top), 3D point cloud (bottom left) and segmentation (bottom right)

References

- AICON 3D SYSTEMS. (2014). *3D quality inspection of sheet metal hole patterns and trimmings*. Retrieved January 16, 2015, from http://www.aicon3d.com/fileadmin/user_upload/produkte/en/breuckmann_Scanner/01_PDF_IuT/Hole_patterns_trimmings_sheetmetal_Web.pdf
- AICON 3D SYSTEMS. (2014). *3D quality inspection of turbine blades*. Retrieved January 16, 2015, from http://www.aicon3d.com/fileadmin/user_upload/produkte/en/breuckmann_Scanner/01_PDF_IuT/Quality_inspection_turbine_blades_Web.pdf
- AICON 3D SYSTEMS. (2014). *The fast, high-precision approach to modern automotive design*. Retrieved December 23, 2014, from http://www.aicon3d.com/fileadmin/user_upload/produkte/en/breuckmann_Scanner/01_PDF_IuT/Modern_automotive_design_Web.pdf
- AICON 3D SYSTEMS. (2014). *Three-dimensional quality inspection of plastic parts*. Retrieved January 16, 2015, from http://www.aicon3d.com/fileadmin/user_upload/produkte/en/breuckmann_Scanner/01_PDF_IuT/Quality_inspection_plastic_parts_Web.pdf
- Aldiek, N., Naumann, H., Gottfried, S., & Löffler-Mang, M. (2014). *Handbuch Bauelemente Optik - Grundlagen, Werkstoffe, Geräte, Messtechnik. (7)*. Carl Hanser Verlag GmbH & Co. KG. Retrieved January 13, 2015, from <http://www.hanser-elibrary.com/isbn/9783446426252>
- Ali, N. (2005). *Reverse Engineering of Automotive Parts Applying Laser Scanning and Structured Light Techniques*. Retrieved April 17, 2015, from http://imaging.utk.edu/publications/papers/dissertation/Sherry_PILOT.pdf
- Bagci, E. (2009). Reverse engineering applications for recovery of broken or worn parts and re-manufacturing: Three case studies. *Advances in Engineering Software*(40), pp. 407-418. Retrieved February 16, 2014, from <http://www.sciencedirect.com/science/article/pii/S0965997808001312>
- Bednara, M., Höfler, H., Nowak, A., & Wölfelschneider, H. (2014). Lichtlaufzeitverfahren / Time-of-flight. *Leitfaden zur optischen 3D-Messtechnik*, 33-36. Fraunhofer Verlag.
- Berndt, D., & Christian, T. (2014). Stereobildverarbeitung / Triangulation. *Leitfaden zur optischen 3D-Messtechnik*(14), 14-19. Fraunhofer Verlag.
- Berndt, D., & Trostmann, E. (2014). In-Prozessprüfung von Montagebaugruppen. *Leitfaden zur optischen 3D-Messtechnik*, 67-69. Fraunhofer Verlag.
- Berndt, D., Boochs, F., & Kühmstedt, P. (2014). 3D-Messen großer Volumen bzw. großer Bauteile. *Leitfaden zur optischen 3D-Messtechnik*, 77-80. Fraunhofer Verlag.
- Bert, T. (2012). *Getting ready for high frame rates in Digital Cinema*. Retrieved February 26, 2015, from http://www.barco.com/projection_systems/downloads/WhitePaper_Getting_ready_for_high_frame_rates_in_digital_cinema.pdf
- Beyerer, J., León, F. P., & Frese, C. (2012). *Automatische Sichtprüfung: Grundlagen, Methoden und Praxis der Bildgewinnung und Bildauswertung*. Springer.
- Born, M., & Wolf, E. (1970). *Principles of Optics* (4. ed.). Pergamon Press. Retrieved March 25, 2015, from <https://archive.org/details/PrinciplesOfOptics>
- Bräuer-Burchardt, C., Möller, M., Munkelt, C., Heinze, M., Kühmstedt, P., & Gunther, N. (2012). Determining Exact Point Correspondences in 3D Measurement Systems Using Fringe Projection – Concepts, Algorithms and Accuracy Determination. In P. Z. Haq, *Applied Measurement Systems* (pp. 211-228). InTech. Retrieved February 8, 2015, from <http://www.intechopen.com/books/applied-measurement-systems/determining-exact-point-correspondences-in-3d-measurement-systems-using-fringe-projection-concepts-a>
- Breitbarth, A. (2012). *Praktische Anwendungen: Hochdynamische 3D-Verfahren*. Retrieved February 19, 2014, from http://www.researchgate.net/publication/236972216_Praktische_Anwendungen_Hochdynamische_3D-Verfahren
- Breitbarth, A. (2014). Muster- und Streifenprojektionsverfahren / Hochdynamische 3D-Verfahren. *Leitfaden zur optischen 3D-Messtechnik*, 14, 20-23. Fraunhofer Verlag.
- Breitbarth, A., Notni, G., Kühmstedt, P., Schreiber, P., & Sieler, M. (2012, April 19). *Patent No. DE102012206472A1*.

- Carl, D. (2014). Digitale Holographie. *Leitfaden zur optischen 3D-Messtechnik*, 14, 45-47. Fraunhofer Verlag.
- Chen, R. H. (2011). *Liquid Crystal Displays: Fundamental Physics and Technology* (1 ed.). John Wiley & Sons Inc.
- Chen, Y. (2014). Advanced liquid crystal materials for display and photonic applications. Retrieved February 21, 2015, from http://etd.fcla.edu/CF/CFE0005314/Dissertation_Esther_Chen_-_final.pdf
- Chinnock, C. (2013). Hybrid Projector Side by Side Demo Big Hit at Projection Summit. Retrieved February 26, 2015, from <http://www.display-central.com/wp-content/uploads/2013/06/sony-hybrid-architecture.png>
- Clive, T. (2013). Claude Monet and Ultraviolet Light. Did the Master Impressionist painter have UV supervision ? Retrieved February 21, 2015, from <http://www.skepticalartist.com/wp-content/uploads/2013/06/Visible-spectrum.jpg>
- de Felice, F., Petrillo, A., & Carlomusto, A. (2014). Shape Measurement Based on 3D Optical Scanner: Real Case Study in the Aeronautics Industry. *Applied Mechanics and Materials*(656), pp. 378-387.
- DELIGHT 2000. (2013). Выбор проектора. Как выбрать проектор правильно? Retrieved March 9, 2015, from <http://www.delight2000.com/images/content/biblioteka/3lcd.jpg>
- Demtröder, W. (2006). *Experimentalphysik 2 - Elektrizität und Optik* (6 ed.). Springer-Verlag.
- Dierking, I. (2014). Chiral Liquid Crystals: Structure, Phases, Effects. *Symmetry*, 6(2), pp. 444-472. Retrieved February 22, 2015, from <http://www.mdpi.com/2073-8994/6/2/444/htm>
- Effenberger, I. (2014). 3D-Objektlageerkennung auf Basis von Lichtschnittsensoren oder 3D-Smartkameras. *Leitfaden zur optischen 3D-Messtechnik*, 74-76. Fraunhofer Verlag.
- Eilam, E. (2005). *Reversing: Secrets of Reverse Engineering*. Wiley Publishing, Inc. Retrieved April 16, 2015, from http://www.foo.be/cours/dess-20122013/b/Eldad_Eilam-Reversing__Secrets_of_Reverse_Engineering-Wiley%282005%29.pdf
- Elze, T., & Tanner, T. G. (2012). *Temporal Properties of Liquid Crystal Displays: Implications for Vision Science Experiments*. Retrieved February 20, 2015, from <http://www.plosone.org/article/fetchObject.action?uri=info:doi/10.1371/journal.pone.0044048&representation=PDF>
- EPSON. (2014). Datasheet L3C07W-9x. Retrieved February 21, 2015, from <http://global.epson.com/products/https/products/pdf/c07w9.pdf>
- Frankowski, G., & Hainich, R. (2009). DLP-Based 3D Metrology by Structured light or Projected Fringe Technology for Life Sciences and Industrial Metrology. *SPIE MOEMS-MEMS: Micro-and Nanofabrication*. Retrieved March 24, 2014, from <http://proceedings.spiedigitallibrary.org/proceeding.aspx?articleid=809222>
- Fratz, M., Beckmann, T., & Carl, D. (2014). 3D-Objektvermessung mit digitaler Mehrwellenlängen-Holographie. *Leitfaden zur optischen 3D-Messtechnik*, 85-87. Fraunhofer Verlag.
- Freeman, M., Champion, M., & Madhavan, S. (2009). Scanned Laser Pico-Projectors: Seeing the Big Picture. *Optics & Photonics News*(May). Retrieved February 26, 2015, from http://www.microvision.com/wp-content/uploads/2014/07/OPN_Article.pdf
- Geng, J. (2011). Structured-light 3D surface imaging: a tutorial. *Advances in Optics and Photonics* 3, pp. 128-160. Retrieved January 13, 2015, from http://www.opticsinfobase.org/view_article.cfm?gotourl=http%3A%2F%2Fwww.opticsinfobase.org%2FDirectPDFAccess%2F2658A1FD-E5FE-CA70-08D4C8597DEB7672_211561%2Faop-3-2-128.pdf%3Fda%3D1%26id%3D211561%26seq%3D0%26mobile%3Dno&org=
- Gockel, T. (2006). Interaktive 3D-Modellerfassung mittels One-Shot-Musterprojektion und schneller Registrierung. Retrieved March 5, 2014, from www.ksp.kit.edu/download/1000004826
- Gorthi, S. S., & Rastogi, P. (2010). Fringe Projection Techniques: Whither we are? *Optics and Laser in Engineering* 48, pp. 133-144. Retrieved February 18, 2014, from <http://infoscience.epfl.ch/record/140745/files/OLEN.pdf>
- Gühning, J. (2002). 3D-Erfassung und Objektrekonstruktion mittels Streifenprojektion. Retrieved February 18, 2014, from <http://d-nb.info/980546680/34>
- Hebbeker, T. (2002). Elektromagnetische Welle. Retrieved February 10, 2015, from http://web.physik.rwth-aachen.de/~hebbeker/lectures/ph2_02/tipl293.gif
- Heist, S., Sieler, M., Breitbarth, A., Kühmstedt, P., & Notni, G. (2013). *Hochgeschwindigkeits-3D-Formvermessung mittels Array-Projektion*. Retrieved February 19, 2014, from http://www.dgao-proceedings.de/download/114/114_a18.pdf

- Heizmann, M., & Werling, S. (2014). Deflektometrie. *Leitfaden zur optischen 3D-Messtechnik*, 14, 28-32. Fraunhofer Verlag.
- Hill, C. (2014). Faseroptische interferometrische Rauheitsmesstechnik. *Leitfaden zur optischen 3D-Messtechnik*, 88-90. Fraunhofer Verlag.
- Hornbeck, L. J. (2002). Digital Light Processing and MEMS: Timely Convergence for a Bright Future. Retrieved February 25, 2015, from http://focus.ti.com/download/dlpdmd/115_Digital_Light_Processing_MEMS_Timely_Convergence.pdf
- IEC. (2002). Electronic projection - Measurement and documentation of key performance criteria - Part 1: Fixed resolution projectors. *IEC 61947-1:2002*. International Electrotechnical Commission (IEC). Retrieved January 21, 2015, from http://www.f07.fh-koeln.de/imperia/md/content/personen/blendl_christian/praktika/9474841.pdf
- IVIEW DISPLAYS. (2014). Product specifications projector engine IPD1231GP. Retrieved April 26, 2014, from http://www.iviewdisplays.com/en/products/products_details.php?pageNo=1&pid=43
- Jozsef, S., & Tibor, A. (2006). *State of the art in LCOS*. Retrieved February 23, 2015, from http://holovisionproject.holografika.eu/news_files/60_53.2_2%20State-of-the-art%20in%20LCOS_public
- JVC. (2007). Die Unterschiede zwischen dem DLA-HD1 und anderen Projektoren. Retrieved February 24, 2015, from http://jdl.jvc-europe.com/site/de/dla-hd1/img/pop4_pic1.jpg
- Kikuchi, H. (2010). Polymer-Stabilized Liquid Crystalline Blue Phases for Display. Retrieved February 17, 2015, from http://www.jst.go.jp/tt/EN/cips_details/pdf_2/1-3.pdf
- Koller, D., Walchshäusl, L., Eggers, G., Neudel, F., Kursawe, U., Kühmstedt, P., . . . Nouak, A. (2011). 3D capturing of Fingerprints - On the way to contactless certified sensor. *BIO/IG*, pp. 33-44. Retrieved February 8, 2015, from <http://cs.emis.de/LNI/Proceedings/Proceedings191/33.pdf>
- Kuhlmann, U., & Paul, E. (2002). Großes Kino - 11 Daten- und Videoprojektoren mit XGA-Auflösung. Retrieved February 25, 2015, from http://www.heise.de/altcms_bilder/124669/3_hires.jpg
- Lenz, M., & Rüther, M. (2009). Projector technologies. Retrieved February 23, 2015, from https://rvlab.icg.tugraz.at/project_page/project_microsense/images/lcos.png
- LIPA. (2015). *LIPA-Laser Illuminated Projector Association*. Retrieved February 27, 2015, from <http://lipainfo.org/laser-projection/laser-regulations/>
- Luhmann, T. (2014). Industriephotogrammetrie. *Leitfaden zur optischen 3D-Messtechnik*, 14, 9-13. Fraunhofer Verlag.
- Lutzke, P., Schaffer, M., Kühmstedt, P., Kowarschik, R., & Notni, G. (2013). Optical Measurement Systems for Industrial Inspection VIII. *Experimental comparison of phase-shifting fringe projection and statistical pattern projection and statistical pattern projection(8788)*. Society of Photo-Optical Instrumentation Engineers (SPIE). Retrieved February 25, 2014, from <http://proceedings.spiedigitallibrary.org/proceeding.aspx?articleid=1687422>
- Martin, R. R., & Várady, T. (1996). RECCAD, Deliverable Document 1 COPERNICUS project, N° 1068. Retrieved April 16, 2015, from <http://ralph.cs.cf.ac.uk/papers/Geometry/recrep.pdf>
- Maxwell, J. C. (1855). Experiments on colour. Retrieved February 24, 2015, from http://www.jimworthey.com/archive/Maxwell_1855_OCRtext.pdf
- Meizi, J. (2010). Fast-Response Liquid Crystal Displays. Retrieved February 20, 2015, from <http://etd.fcla.edu/CF/CFE0003435/Jiao-Meizi-201012-PhD.pdf>
- Mellish, B. (2006). Wire-grid polarizer. Retrieved March 3, 2015, from <http://upload.wikimedia.org/wikipedia/commons/thumb/9/94/Wire-grid-polarizer.svg/2000px-Wire-grid-polarizer.svg.png>
- MERCK. (2013). *A Deep Dive into Merck's LC & OLED Business*. Darmstadt. Retrieved February 20, 2015, from http://www.merck.de/company.merck.de/de/images/LCOLEDDay_Complete_final_tcm1613_110011.pdf?Version=
- MERCK. (2015). *Merck Performance Materials*. Retrieved March 5, 2015, from http://www.merck-performance-materials.com/corp.performance_materials/en/images/LC_Phases_EN_440x200_tcm2033_100325.jpg
- Morrison, G. (2013). Panasonic Low(ish)-Cost LED Projectors. Retrieved March 6, 2015, from http://cdn.soundandvision.com/images/styles/600_wide/public/pana_laser_led_hybrid.jpg
- Motamedi, E. M. (2004). *MOEMS: Micro-Opto-Electro-Mechanical Systems*. SPIE Press.

- Munday, R. (2006). Visual Perception 8. Retrieved February 8, 2015, from <http://visual-memory.co.uk/daniel/Modules/FM21820/images/projector.gif>
- Murat, H., Avci, A., Beernaert, R., Dhaenens, K., De Smet, H., Bogaert, L., . . . Meuret, Y. (2008). Two LCOS full color projector with efficient LED illumination engine. Retrieved February 17, 2015, from http://www.researchgate.net/profile/Youri_Meuret/publication/222565678_Two_LCOS_full_color_projector_with_efficient_LED_illumination_engine/links/0fcfd50dc03a979a41000000.pdf
- Navarro Fernández, S. (2012). One-shot pattern projection for dense and accurate 3D reconstruction in structured light. Retrieved February 19, 2014, from <http://dugi-doc.udg.edu/bitstream/handle/10256/7034/tsfn.pdf?sequence=1>
- Nordmann, A. (2007). Refraction on an aperture in the manner of Huygens. Retrieved March 26, 2015, from http://upload.wikimedia.org/wikipedia/commons/thumb/6/60/Refraction_on_an_aperture_-_Huygens-Fresnel_principle.svg/2000px-Refraction_on_an_aperture_-_Huygens-Fresnel_principle.svg.png
- Notni, G. (2014). Leitfaden zur optischen 3D-Messtechnik. *Überblick über optische 3D-Messverfahren(14)*. Fraunhofer Verlag.
- Notni, G., & Kühmstedt, P. (2013). New example for a high speed 3D-sensor - Vom stationären zum dynamischen Messen. Retrieved February 19, 2014, from http://spectronet.de/portals/visqua/story_docs/intern_spectronet/vortraege/130305_16_collab_vortraege/130305_03_kuehmstedt_fhg_iof.pdf
- Pagès, J., Salvi, J., García, R., & Matabosch, C. (2003). Robotics and Automation. *Overview of coded light projection techniques for automatic 3D profiling(1)*, 133-138. IEEE. Retrieved January 13, 2015, from <http://dugi-doc.udg.edu/bitstream/handle/10256/2278/60.pdf?sequence=1>
- Palme, C. (2015). *www.curtpalme.com Home theater*. Retrieved February 23, 2015, from <http://www.curtpalme.com/PJSpecs.shtml>
- Rao, L. (2012). Low Voltage Blue Phase Liquid Crystal Displays. Retrieved February 21, 2015, from http://etd.fcla.edu/CF/CFE0004625/Dissertation_LRAO_final.pdf
- Rao, L., Zhibing, G., Sebastian, G., Kuan-Ming, C., & Shin-Tson, W. (2010). Emerging Liquid Crystal Displays Based on the Kerr Effect. (L. Taylor & Francis Group, Ed.) *Molecular Crystals and Liquid Crystals*, pp. 30-42. Retrieved February 17, 2015, from <http://www.creol.ucf.edu/research/Publications/2222.pdf>
- Reichl, J. (2006). LCoS projektory. Retrieved February 24, 2015, from http://fyzika.jreichl.com/data/optika/33_opticke_pristroje_soubory/projektory/image032.jpg
- Riedel, J. (2014). Weißlichtinterferometrie. *Leitfaden zur optischen 3D-Messtechnik, 14*, 42-44. Fraunhofer Verlag.
- Sakurambo. (2007). Illustration of the CIE 1931 color space. Retrieved from <http://upload.wikimedia.org/wikipedia/commons/thumb/0/02/CIExy1931.svg/2000px-CIExy1931.svg.png>
- Salvi, J., Pagès, J., & Battle, J. (2004). Pattern codification strategies in structured light systems. Retrieved February 20, 2014, from <http://citeseerx.ist.psu.edu/viewdoc/download;jsessionid=4AC4B0F3B559E4B398A6DB060E9A449D?doi=10.1.1.9.5774&rep=rep1&type=pdf>
- Scharstein, D., & Szeliski, R. (2001). *A Taxonomy and Evaluation of Dense Two-Frame Stereo Correspondence Algorithms*. Microsoft Research. Retrieved April 9, 2015, from <http://131.107.65.14/pubs/69895/tr-2001-81.pdf>
- SCHOTT. (2014). *SCHOTT advanced optics*. Retrieved March 20, 2015, from http://www.us.schott.com/advanced_optics/english/download/schott-tie-29-refractive-index-and-dispersion-april-2014-us.pdf
- Schröder, G., & Treiber, H. (2007). *Technische Optik* (10 ed.). Vogel Buchverlag.
- Schwarte, R., Häusler, G., & Malz, R. (2000). Three-Dimensional Imaging Techniques. In B. Jähne, & H. Haußecker, *Computer Vision and Applications* (pp. 177-205). Academic Press.
- SITER. (2014). Working principle of UHP single lamp DLP seamless splicing screen . Retrieved February 24, 2015, from <http://www.siter999.com/Upload/Images/20140325/201403251931163900024.gif>
- STEENBECK. (2013). Steenbeck user manual 16mm 01-Series. Retrieved February 8, 2015, from http://www.steenbeck.com/manual/16mm_01_serie.pdf
- Takato, K., Hasegawa, M., Koden, M., Itoh, N., Hasegawa, R., & Sakamoto, M. (2005). *Alignment Technologies and Applications of Liquid Crystal Devices*. Tylor & Francis. Retrieved February

- 20, 2015, from <http://ir.nmu.org.ua/bitstream/handle/123456789/121995/b4382c73f8ffa3f3b18742ae72745e24.pdf?sequence=1&isAllowed=y>
- Taphanel, M. (2014). Chromatische konfokale Triangulation. *Leitfaden zur optischen 3D-Messtechnik*, 14, 39-41. Fraunhofer Verlag.
- TI. (2010). *DLP System Optics*. Retrieved February 24, 2015, from <http://www.ti.com/lit/an/dlpa022/dlpa022.pdf>
- TI. (2013). Datasheet DLP 0.45 WXGA DMD. Retrieved February 25, 2015, from <http://www.ti.com/lit/ds/symlink/dlp4500.pdf>
- TI. (2013). Datasheet DLP 0.55 XGA Series 450 DMD. Retrieved February 26, 2015, from <http://www.ti.com/lit/ds/symlink/dlp5500.pdf>
- TI. (2013). *DMD 101: Introduction to Digital Micromirror Device (DMD) Technology*. Retrieved February 24, 2015, from <http://www.ti.com/lit/an/dlpa008a/dlpa008a.pdf>
- TI. (2014). DLP LightCrafter 4500 Evaluation Module User's Guide. Retrieved March 26, 2014, from <http://www.ti.com/lit/ug/dlpu011d/dlpu011d.pdf>
- TI. (2014). DLP Lightcrafter 6500 and 9000 EVM User's Guide. Retrieved January 30, 2015, from <http://www.ti.com/lit/ug/dlpu028a/dlpu028a.pdf>
- TI. (2015). Getting Started with DLP Pico Technology. Retrieved February 23, 2015, from <http://www.ti.com/lit/wp/dlpa059/dlpa059.pdf>
- Trostmann, E., & Dunker, T. (2014). Lichtschnittverfahren. *Leitfaden zur optischen 3D-Messtechnik*, 14, 24-27. Fraunhofer Verlag.
- Tsolis, N. (2009). DMD chip - DLP. Retrieved February 24, 2015, from http://www.projectorjunkies.com/wp-content/uploads/2014/02/dlp_selection_of_colour_wheels.jpg
- VDC. (2015). *www.vdc.com VDC Display Systems*. Retrieved February 23, 2015, from <http://vdc.com/site/crt-projector-support/>
- VIALUX. (2015). Datasheet STAR-065 EVM Monochrome LED light engines. Retrieved January 30, 2015, from http://vialux.de/pdf/E_STAR_065_EVM.pdf
- Wandell, B. (2012). *Foundations of Vision*. Retrieved February 22, 2015, from <https://foundationsofvision.stanford.edu/appendix/>
- Weise, T., Leibe, B., & van Luc, G. (2007). Fast 3D Scanning with Automatic Motion Compensation. Retrieved March 17, 2014, from https://www.vision.ee.ethz.ch/publications/papers/proceedings/eth_biwi_00489.pdf
- Wendel, S. (2014). Spektrum der Lichttechnik. *Freiform-Optiken im Nahfeld von LEDs*, 7, 14. KIT Scientific Publishing. Retrieved April 24, 2015, from <http://d-nb.info/106301400X/34>
- Wernemünde, R. (2014). Dimensionelle Inline-Qualitätsprüfung. *Leitfaden zur optischen 3D-Messtechnik*, 63-66. Fraunhofer Verlag.
- Westin, S. (2012). Camera Mounts. Retrieved January 29, 2015, from <http://www.graphics.cornell.edu/~westin/misc/mounts-by-register.html>
- WINTeCH. (2015). DLP LightCrafter 4500. Retrieved February 2, 2015, from https://www.wintechdigital.com/image/cache/data/Procuts/LCR4500/LightCrafter4500_side-1051x710.jpg
- Wiora, G. (2001). Optische 3D-Messtechnik: Präzise Gestaltvermessung mit einem erweiterten Streifenprojektionsverfahren. Retrieved March 5, 2014, from http://archiv.ub.uni-heidelberg.de/volltextserver/1808/3/03_Diss_Wiora_Online_Version.pdf
- Wissmann, P. (2013). *Hand-Guided 3-D Scanning*. Retrieved February 7, 2015, from Universitätsbibliothek RWTH Aachen University: <http://darwin.bth.rwth-aachen.de/opus3/volltexte/2014/4842/pdf/4842.pdf>
- Wissmann, P., Forster, F., & Schmitt, R. (2011). Fast and low-cost structured light pattern sequence projection. *Optics Express*, pp. 24657-24671. Retrieved February 20, 2014, from http://www.opticsinfobase.org/view_article.cfm?gotourl=http%3A%2F%2Fwww.opticsinfobase.org%2FDirectPDFAccess%2F1CC28437-D5A4-A37D-56B664291A40AC45_224470%2Foe-19-24-24657.pdf%3Fda%3D1%26id%3D224470%26seq%3D0%26mobile%3Dno&org=
- Yan, J., & Wu, S.-T. (2011). Polymer-stabilized blue phase liquid crystals: a tutorial. *Optical Materials Express*(8). Retrieved February 17, 2015, from http://www.opticsinfobase.org/view_article.cfm?gotourl=http%3A%2F%2Fwww.opticsinfobase.org%2FDirectPDFAccess%2FF6DBD2BF-CE2B-9780-

- 77C80CCF964BD757_224213%2Fome-1-8-1527.pdf%3Fda%3D1%26id%3D224213%26seq%3D0%26mobile%3Dno&org=
- Yuan, C., Fenglin, P., & Wu, S.-T. (2013). Submillisecond-Response Vertical-Aligned Liquid Crystal for Color Sequential Projection Displays. *Journal of display technology*, 9(2). Retrieved February 5, 2015, from <http://lcd.creol.ucf.edu/Publications/2013/JDT%20Chen%20VA-LCOS.pdf>
- ZEISS. (2013). Optical Knowledge - Optical Parameters. Retrieved March 20, 2015, from http://www.zeiss.com/vision-care/en_de/eye-care-professionals/optical-knowledge/optical-basics/optics-the-eye/optical-parameters.html
- Zhang, S., van der Weide, D., & Oliver, J. (2010). Superfast phase-shifting method for 3-D shape measurement. Retrieved February 19, 2014, from http://lib.dr.iastate.edu/cgi/viewcontent.cgi?article=1045&context=me_pubs
- Zhang, Z., Zheng, Y., & Daping, C. (2014). Fundamentals of phase-only liquid crystal on silicon (LCOS) devices. *Light: Science & Applications*. Retrieved February 20, 2015, from <http://www.nature.com/lisa/journal/v3/n10/pdf/lisa201494a.pdf>
- Zhou, M. (2011). A New Approach of Composite Surface Reconstruction Based on Reverse Engineering. *Procedia Engineering*, pp. 594-599. Retrieved February 8, 2015, from http://ac.els-cdn.com/S1877705811053951/1-s2.0-S1877705811053951-main.pdf?_tid=f8c793a0-af93-11e4-8f90-00000aacb361&acdnat=1423401259_7edf944fba6628ee1fe56ff4fdd09140